Kinetics and Mechanism of Deoxygenation Reactions over Proton-Form and Molybdenum-Modified Zeolite Catalysts

A DISSERTATION
SUBMITTED TO THE FACULTY OF THE
UNIVERSITY OF MINNESOTA
BY

Jeremy William Bedard

IN PARTIAL FULFILLMENT OF THE
REQUIREMENTS FOR THE DEGREE OF
DOCTOR OF PHILOSOPHY

Advisors: Aditya Bhan and Lanny Schmidt

July 2014

ACKNOWLEDGMENTS

The past five years has definitely been an unpredictable experience. There have been frustrating and joyous occasions, yet they all have directed me on the path to where I am now. I know I would not be where I am today without the numerous friends and colleagues that have helped me along the way. I would like to take this opportunity to thank all of you, with a few specifics below.

I must start with my advisers, Professors Aditya Bhan and Lanny Schmidt, because without them, I would not be writing this. Professor Bhan has been a constant source of passion, motivation, and ambition. His rigorous methods of conducting research and communicating scientific results has molded me into not only a more effective investigator, but also a more critical and creative thinker that I can extend to all areas of life. I am truly grateful for the opportunity to explore and learn with these two people.

I have great appreciation for my group members, who have mentored me along the way. Dr. Hsu Chiang was the first the show me the ropes in lab, and eased my transition into kinetic studies. Dr. Ian Hill provided someone to talk to regarding technical as well as personal subjects. Some days you don't want to talk about science, and Ian was always willing. Dr. Reetam Chakrabarti always had a practical and simplistic approach to research. Someday I will introduce myself and my work as "Me, Bedard. Biomass, Gasoline, F-150." Dr. Samuel Blass started the same year as me, yet somehow finagled his way out early. Sam was always eager to discuss my latest results, be it graduate school related or not. His constant reminders that "you cannot do this in industry" were greatly revered. As were his cookies, that he tried, in vain, to hide in his desk. Current and past lab mates include Elizabeth Mallon, Samia Ilias, Mark Mazar, Do-Young Hong, Srinivas Rangaragan, Dongxia Liu, Michael Skinner, Christine Colby, Jake Kruger, Hui Sun, Alex Marvin, Nils Persson, Dario Prieto Centurion, Wen-Sheng Lee, Joseph DeWilde, Cha-Jung Chen, Minje Kang, Rachit Khare, Mark Sullivan, Udit Gupta, Linh Bui, Andrew Hwang, and Anurag Kumar. Thank you all for guidance and support.

I must acknowledge my friends outside of the department for making graduate life a bit more balanced. I could not ask for better roommates than Brian Woods and Drew Thompson. Thank you for making 3120 unforgettable. A

giant thanks goes to some of my closest friends including Nick Kirby, Tony Campos, Ange Colvin, Spencer Broughten, Erik Knoll, Jake Holsten, Maura Coonan, Joel Rindelaub, and most recently and importantly, Brittany Bleess. Friends like you guys make it all worthwhile.

Lastly, I must thank those that have been there since the very beginning: my family. The unending encouragement and admiration is irreplaceable. Thank you Mom for always pushing me to the highest level. Thank you Dad for your support in my endeavors. Thank you Jason for being a great brother.

ABSTRACT

The depletion of fossil fuel resources and the environmental consequences of their use have dictated the development of new sources of energy that are both sustainable and economical. Biomass has emerged as a renewable carbon feedstock that can be used to produce chemicals and fuels traditionally obtained from petroleum. The oxygen content of biomass prohibits its use without modification because oxygenated hydrocarbons are non-volatile and have lower energy content. Chemical processes that eliminate oxygen and keep the carbon backbone intact are required for the development of biomass as a viable chemical feedstock. This dissertation reports on the kinetic and mechanistic studies conducted on high and low temperature catalytic processes for deoxygenation of biomass precursors to produce high-value chemicals and fuels.

Low temperature, steady state reaction studies of acetic acid and ethanol were used to identify co-adsorbed acetic acid/ethanol dimers as surface intermediates within specific elementary steps involved in the esterification of acetic acid with ethanol on zeolites. A reaction mechanism involving two dominating surface species, an inactive ethanol dimeric species adsorbed on Brønsted sites inhibiting ester formation and a co-adsorbed complex of acetic acid and ethanol on the active site reacting to produce ethyl acetate, is shown to describe the reaction rate as a function of temperature (323 – 383 K), acetic acid (0.5 – 6.0 kPa), and ethanol (5.0 – 13.0 kPa) partial pressure on proton-form BEA, FER, MFI, and MOR zeolites. Measured differences in rates as a function of zeolite structure and the rigorous interpretation of these differences in terms of esterification rate and equilibrium constants is presented to show that the intrinsic rate constant for the activation of the co-adsorbed complex increases in the order FER < MOR < MFI < BEA.

High temperature co-processing of acetic acid, formic acid, or carbon dioxide with methane (CH_3COOH/CH_4 = 0.04-0.10, $HCOOH/CH_4$ = 0.01-0.03, CO_2/CH_4 = 0.01-0.03) on Mo/H-ZSM-5 formulations at 950 K and atmospheric pressure in an effort to couple deoxygenation and dehydrogenation reaction sequences results instead in a two-zone, stratified bed reactor configuration consisting of upstream oxygenate/CH_4 reforming and downstream CH_4 dehydroaromatization. X-ray absorption spectroscopy and chemical transient

experiments show that molybdenum carbide is formed inside zeolite micropores during CH_4 reactions. The addition of an oxygenate co-feed causes oxidation of the active molybdenum carbide catalyst while producing CO and H_2 until completely converted. Forward rates of C_6H_6 synthesis are unperturbed by the introduction of an oxygenate co-feed after rigorously accounting for the thermodynamic reversibility caused by the H_2 produced in oxygenate reforming reactions and the fraction of the active catalyst deemed unavailable for CH_4 dehydroaromatization. All effects of co-processing $C_{1\text{-}2}$ oxygenates and molecular H_2 with CH_4 can be interpreted in terms of an approach to equilibrium.

Co-processing H_2O, CO_2, or light ($C_{1\text{-}2}$, $C/H_{eff} < 0.25$) oxygenates with CH_4 at 950 K over Mo/H-ZSM-5 catalysts results in complete fragmentation of the oxygenate and CO as the sole oxygen-containing product. The C/H_{eff} accounts for removal of O as CO and describes the net C_6H_6 and total hydrocarbon synthesis rates at varying (0.0-0.10) $C_{1\text{-}2}$ oxygenate and H_2 to CH_4 co-feed ratios. Co-processing larger ($C_{3\text{-}5}$, $C/H_{eff} \geq 0.25$) oxygenates with CH_4 results in incomplete fragmentation of the co-fed oxygenate and preferential pathways of C_6H_6 synthesis that exclude CH_4 incorporation. This results in greater net C_6H_6 synthesis rates than would be predicted from observations made when co-processing $C_{1\text{-}2}$ oxygenates.

Catalytic technologies have served a crucial role in processing petroleum feedstocks and are faced with new challenges as the feedstock shifts to chemically diverse but renewable biomass sources. This research addresses these challenges at fundamental and applied levels as it offers the potential to convert readily available biomass to commodity chemicals and fuels while simultaneously examining the elementary concepts of deoxygenation reactions on catalytic surfaces.

TABLE OF CONTENTS

LIST OF TABLES

LIST OF FIGURES

CHAPTER

ONE

INTRODUCTION

1.1 Motivation

New sources of energy are needed as the world's population grows, energy consumption escalates, and fossil fuel supplies diminish.[1,2] Renewable resources such as biomass, solar, and wind energy have the potential to reduce the world's dependence on fossil fuels for its energy demands.[3–5] Of these, biomass is the only renewable carbon feedstock available for the production of chemicals and fuels currently obtained from crude oil.[6–9] The oxygen content of biomass (~50% by weight) creates a processing challenge when compared with traditional carbon sources because oxygenated hydrocarbons are non-volatile and possess a lower heating value than hydrocarbons without oxygen.[7,10] Chemical processes that eliminate oxygen while maintaining or even increasing the carbon chain length are required for the development of biomass as a viable chemical feedstock. This dissertation reports on the investigation into the kinetic and mechanistic chemistry that is involved in oxygen removal from model biomass molecules to produce fuels and commodity chemicals.

The conversion of biomass to hydrocarbons is limited by oxygen removal. Strategies for removing oxygen from biomass monomers include dehydration and decarboxylation reactions. Figure 1.1 shows the species derived from a C_5 carbohydrate through these oxygen removal techniques in the absence of hydrogen or methane. While elimination of H_2O is easier than CO_2 in carbohydrates, extensive dehydration leads to stable cyclic species which hinder additional oxygen removal.[11] Dehydration of biomass also leads to unsaturated compounds and ultimately aromatic species which are unsuitable for use as fuels

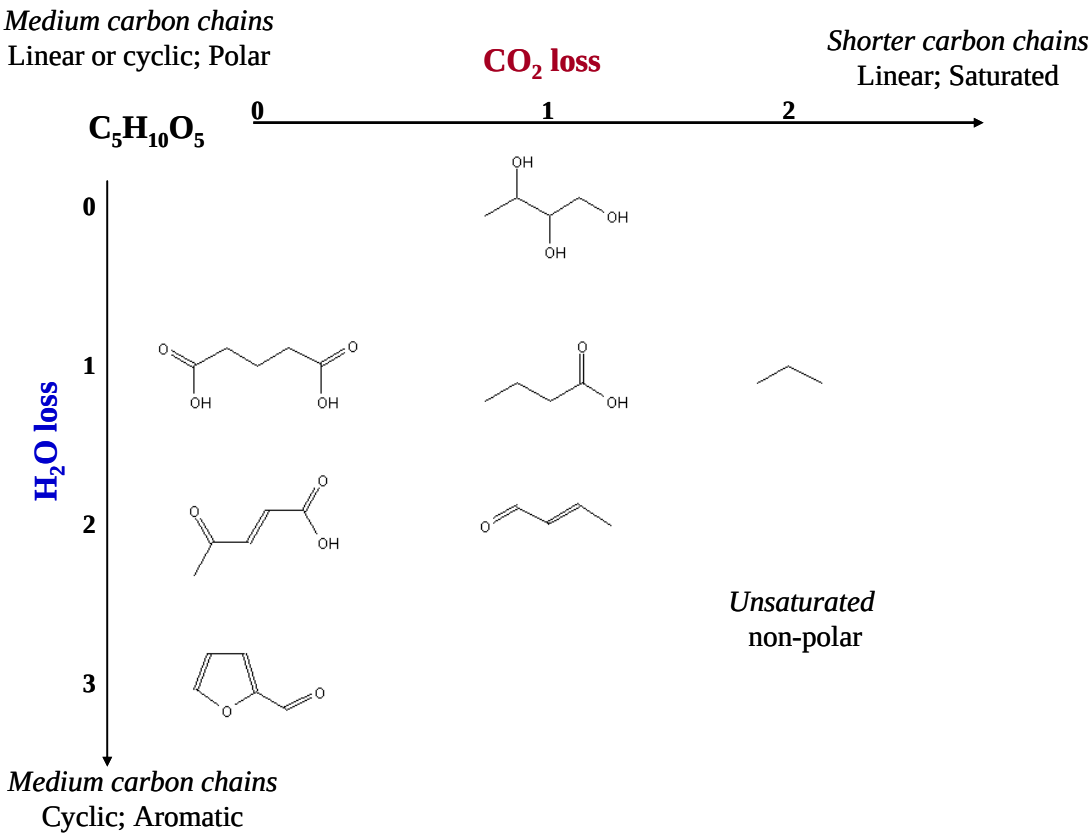

Figure 1.1 Species derived from dehydration and decarboxylation of C_5-carbohydrates.

alone due to their toxicity. Decarboxylation leaves behind hydrogen which enables the production of saturated compounds, but this process also reduces the carbon chain length which results in small hydrocarbons that are too volatile for use as liquid fuels. Ultimately, neither of these strategies is sufficient to synthesize the non-polar and saturated hydrocarbons that are compatible with the existing transportation infrastructure.

A more efficient method of removing oxygen from biomass is reduction with hydrogen to maintain the carbon chain length while keeping the molecule saturated. Hydrogenation with molecular H_2 is not a viable means of deoxygenation as H_2 is not found naturally on earth so mass production must occur by way of hydrocarbon reforming which is energy intensive. Processing conditions for hydrogenation are also difficult to optimize as H_2 is a gas, the oxygenate is a liquid, and the catalyst is a solid.

Methane, the main constituent of natural gas, is also an abundant source of carbon being investigated as a raw material for the synthesis of energy carriers and chemicals currently obtained from petroleum.[12–14] Methane activation

involves dehydrogenation to grow carbon chains; this process is energy intensive because of the high dissociation energy (104 kcal mol^{-1}) and low polarity (χ_C = 2.5; χ_H = 2.2) of the C-H bond.[12] Coupling deoxygenation of biomass with dehydrogenation of methane would serve to activate both carbon feedstocks to produce higher value products closer in stoichiometry to those derived from fossil fuels. Figure 1.2 depicts hydrogen transfer across zeolite derived catalysts with methane acting as a surrogate for molecular hydrogen to facilitate deoxygenation of biomass. Zeolites are used industrially in petroleum refineries because they enable hydrogen transfer; the only difference here is oxygenates as one of the feedstocks.[15]

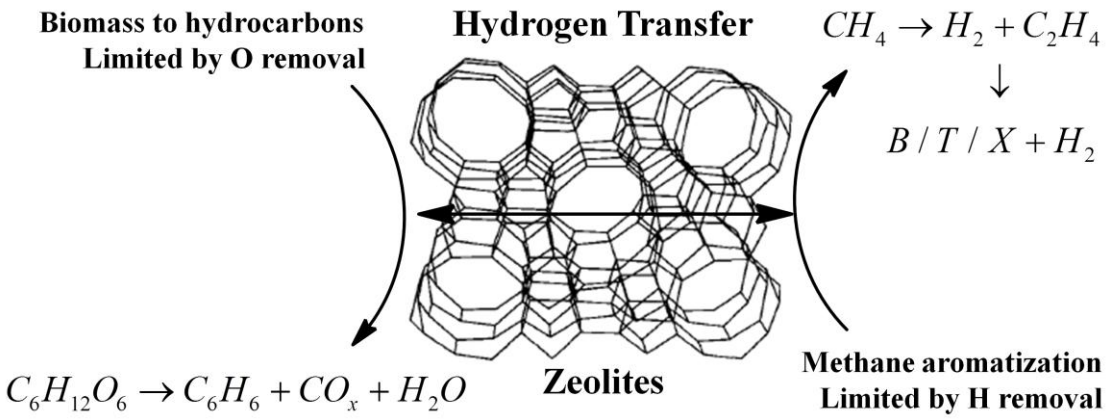

Figure 1.2 Hydrogen transfer from hydrogen rich alkanes to hydrogen deficient oxygenates.

1.2 Background

1.2.1 Zeolites as solid Brønsted acid catalysts

Zeolites are crystalline microporous aluminosilicates that are commonly used as catalysts in the petroleum industry.[15] The zeolite framework consists of SiO_2 tetrahedra with some degree of Al substitution. Replacing a Si^{4+} atom with a trivalent Al^{3+} cation creates a negative charge on a framework oxygen directly bonded to the Al. This negative charge must be balanced by a cation, commonly Na^+, NH_4^+, or H^+. The hydroxyl group that results when the counter-ion is a proton generates the Brønsted acidity observed in zeolites.[16] Figure 1.3 shows how the Brønsted acid site is depicted for reaction schemes.

Zeolites are categorized by their crystalline framework and as of 2013, there are 201 known zeolite structures with each type distinguished by a 3-capital

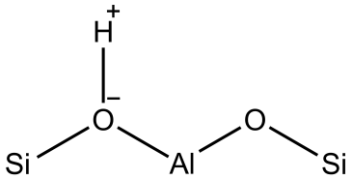

Figure 1.3 Brønsted acid site in zeolites.

letter code usually derived from the name of the type of material.[17,18] Each zeolite is distinctive because of its channel system and pore size. The pore size is denoted by the number of tetrahedral (T) atoms in a membered ring (MR). For example, MFI has 10 Si or Al in its largest channel and therefore it is designated as having 10-MR channels. Table 1.1 summarizes structural features of the zeolites used in this investigation as deoxygenation catalysts. Some zeolites are referred to by different names to distinguish the zeolite in its proton form, e.g. H-ZSM5 for proton-form MFI and Hβ for proton-form BEA.

Table 1.1 Properties of zeolites

Sample	**BEA**	**FER**	**MFI**	**MOR**
Structure	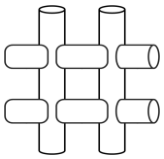	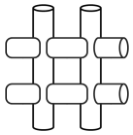	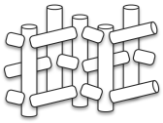	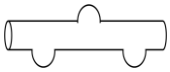
Framework Density (T/1000 Å^3)*	15.3	17.6	18.4	17.0
Channel System*	3-D	2-D	3-D	1-D
Largest Channel Sizes (Å)*	12-MR 6.6 x 6.7 12-MR 5.6 x 5.6	10-MR 4.2 x 5.4 8-MR 3.5 x 4.8	10-MR 5.1 x 5.5 10-MR 5.3 x 5.6	12-MR 6.5 x 7.0 8-MR 2.6 x 5.7
Si:Al**	12.5	10	11.5	10
Surface Area (m^2g^{-1})**	680	100	425	500

*[19] **[20]

1.2.2 Deoxygenation reactions of biomass model compounds

Chen et al. have defined an effective hydrogen index (EHI, Equation 1.1) which characterizes heteroatom-containing hydrocarbons by their hydrogen deficiency.[21] For comparison, a C_6 sugar ($C_6H_{12}O_6$) has an EHI of 0 whereas

ethanol and a C_8-alkane have an EHI of 2 and 2.25, respectively. Currently studied deoxygenation strategies include rapidly heating (> 700 Ks^{-1}) solid biomass samples together with H-ZSM-5.[22,23] This process avoids thermal decomposition prior to deoxygenation reactions which include decarbonylation, decarboxylation, dehydration, and aromatization. Partially deoxygenated compounds are produced, but much of the carbon ends up as hydrogen-deficient coke species or is lost as CO and CO_2 (~50% carbon yield).[22] This fast pyrolysis technique converts biomass to usable liquids but does not address the inherent need to add hydrogen to remove oxygen as water and avoid the loss of carbon as CO_2 or CO. The strategies investigated here to combat this shortcoming are (1) to partially deoxygenate model compounds coupled with chain growth and (2) to use CH_4 as a potential hydrogen transfer reagent.

$$EHI = \frac{H - 2O - 3N - 2S}{C} \tag{1.1}$$

1.3 Mechanistic studies of deoxygenation via esterification

Esterification is a nucleophilic acyl substitution reaction with the carbonyl group of the carboxylic acid acting as the electrophile and an alcohol as the nucleophile. This reaction was first presented by Emil Fischer and is well-described for the homogenous aqueous reaction.[24,25] Industrially, esterification is conducted using mineral acids such as H_2SO_4 and HCl as the catalyst to produce esters that are used as solvents or chemicals for packaging, pharmaceutical, perfume, and flavoring industries.[26,27] Industrial homogenous catalysis with mineral acids is plagued by reactor corrosion, poor catalyst recovery, and difficult product separation such that a move to solid acids is desired.[28]

Gas-phase esterification reactions have been studied on a variety of solid acids including silica supported sulfonic acids,[29–34] metal oxides,[31,35,36] heteropolyacids,[37,38] ion-exchange resins,[31,35] and zeolites.[35,39–42] Some of these studies aim to improve on batch reactor conversions with pervaporation to remove water,[39,43] while other studies compare conversion and selectivity among different solid acids.[31,35] Acetic acid is the most common carboxylic acid studied while the alcohol is usually methanol or ethanol. Studies comparing alcohols show higher alcohol conversion for shorter, straight-chain species versus

longer and branched reactants.[42,44] The mechanism of esterification on heterogeneous catalysts is debated in the literature as some studies suggest Langmuir-Hinshelwood (LH) kinetics, [34,45,46] while others propose Eley-Rideal (ER) kinetics.[29,32,36,42,44,47,48] The LH model is used to describe a mechanism in which two adsorbed species react together, and is therefore referred to as a dual-site mechanism whereas the ER model describes a mechanism in which a gaseous species reacts with an adsorbed species, and is therefore referred to as a single-site mechanism.[49]

This ambiguity in the reaction mechanism has been considered and the research conducted as part of this dissertation has provided a reaction mechanism that is consistent over many zeolites. This was accomplished by deriving rate expressions that are consistent with steady-state kinetic experiments across a range of temperatures (323-383 K), reactant partial pressures (0.5-13.0 kPa), and zeolite topologies (BEA, FER, MFI, and MOR). The rate expressions were further supported through isotopic experiments to confirm a rate determining step by exploiting the kinetic isotope effect. The rate expression was tested over many zeolites to elucidate the effect of zeolite topology on the rate and mechanism of esterification reactions. A structure-function correlation was derived to show how shape selectivity can be used to predict products of deoxygenation reactions over various zeolites.

1.4 Kinetic studies of methane and light oxygenate co-processing over Mo/H-ZSM-5

Mo/H-ZSM5 catalysts have been studied for their production of aromatics and hydrogen from CH_4 in a process termed methane dehydroaromatization (DHA).[50–52] Formation of aromatics from CH_4 is thermodynamically unfavorable at temperatures less than 773 K in the absence of oxygen, but DHA selectively converts methane directly to hydrogen and benzene in a non-oxidative process at these high temperatures.

This chemistry requires encapsulation of the metal clusters inside the zeolite because CH_4 is only activated on metals.[53,54] Encapsulation requires vapor phase synthesis such that volatile Mo species can exchange with protons at aluminum sites and a well-dispersed Mo/ZSM-5 material is obtained.[55] Molybdenum oxide complexes are often used as the Mo precursor such that Mo oxide, in the structure of $Mo_2O_5^{2+}$ dimers, form on the active site. The transformation is shown in Figure 1.4. The extent of dimer formation

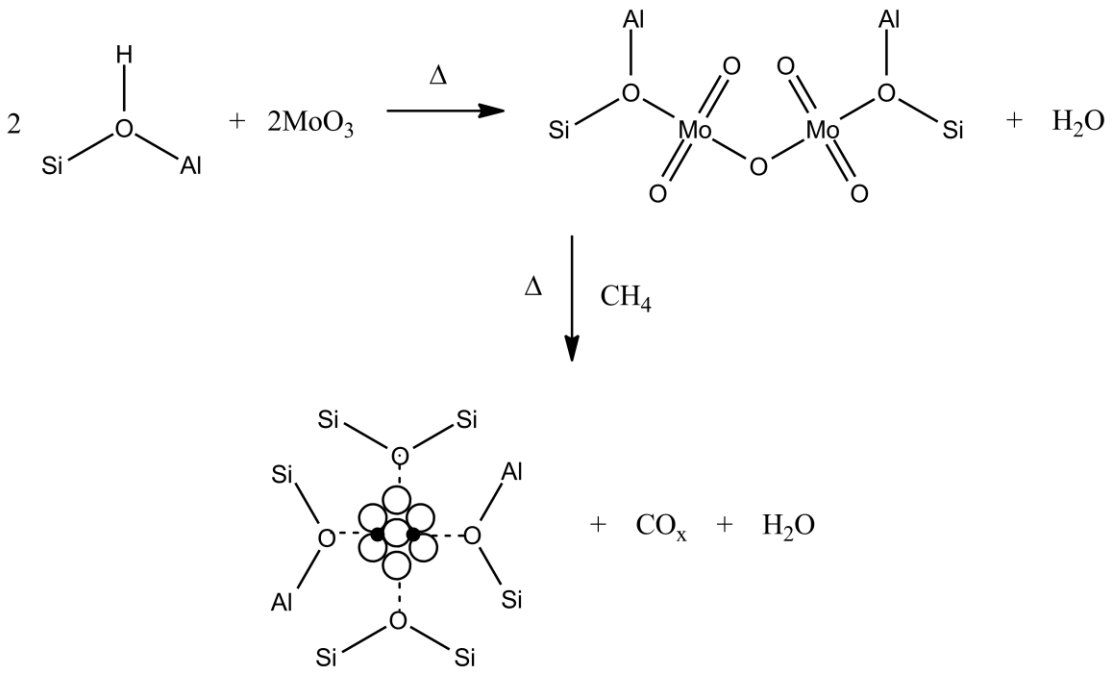

Figure 1.4 Exchange of H^+ with $Mo_2O_5^{2+}$ dimers on ZSM-5 followed by reduction to MoC_x clusters with CH_4.

including its dispersion can be determined through titration of the remaining hydroxyl groups with D_2 as well as using infrared spectroscopy.[53,56]

Once methane is introduced to the catalyst at temperatures ~973 K, the $Mo_2O_5^{2+}$ dimers are reduced to Mo carbide clusters, MoC_x, as shown in Scheme 1.1.[57,58] Production of MoC_x can be inferred by the removal of oxygen in the form of CO, CO_2, and H_2O as well as evidenced by changes in the X-ray absorption spectrum. The catalyst activates C-H bonds of methane that produce activated carbon species on the cluster surface.[59] These carbon species can then dimerize to produce ethylene.[52–54,57] Ethylene desorbs from the metal-carbide cluster and is oligomerized over Brønsted acid sites to produce benzene and other aromatics.[54] Deactivation is observed when the C^* deposited on the surface of the catalyst by methane activation is not removed effectively by H^* intermediates, which can result in coke formation.[51,53,54] Co-processing small quantities of oxidants such as CO_2 has been shown to effectively remove these carbon deposits, enabling the catalyst to continue CH_4 activation.[59,60]

We have built on the methane DHA process by co-feeding oxygenate compounds such as acetic acid, ethanol, and acetone to not only scavenge the

activated carbon species that cause coking, but also serve as model biomass compounds that are deoxygenated. Co-processing of various C_{1-2} oxygenates with CH_4 (O^*/CH_4 = 0.0-0.10) on Mo/H-ZSM-5 catalysts at 950 K in an effort to couple deoxygenation and dehydrogenation reactions results instead in a two-zone, stratified reactor bed consisting of upstream reforming of the oxygenate followed by downstream CH_4 dehydroaromatization. The addition of these oxygenates causes MoC_s oxidation while producing H_2 and CO as the sole oxygen-containing product. Forward rates were found to be unperturbed by the introduction of H_2, CO_2, HCOOH, or CH_3COOH after rigorously accounting for the fraction of active catalyst oxidized and the thermodynamic reversibility caused by H_2 produced in reforming reactions. All effects of co-processing C_{1-2} oxygenates with CH_4 can be interpreted in terms of an approach to equilibrium. Co-processing of these oxygenates possessing acid, hydroxyl, and carbonyl functionalities as well as H_2O and CO_2 results in complete fragmentation of the oxygenate as evidenced by steady-state kinetic studies of isotopically labeled reactants. The C to H effective ratio (Equation 1.2) was devised to characterize these co-feeds and serves as a single value descriptor for predicting the C_6H_6 as well as the total hydrocarbon net synthesis rate.

$$C/H_{eff} = \frac{C-O}{H} \tag{1.2}$$

CHAPTER

TWO

KINETICS AND MECHANISM OF ACETIC ACID ESTERIFICATION WITH ETHANOL ON ZEOLITES*

2.1 Introduction

Esterification reactions are used to produce fine chemicals and represent a method to concurrently extend the carbon chain length and to accomplish deoxygenation of oxygen-containing compounds that can be derived from biorenewable resources [26]. Several routes of producing esters synthetically have been briefly examined by Yadav and Mehta [38]. Industrially, ester production is most commonly catalyzed by homogenous mineral acids such as H_2SO_4 and HCl [27]. Ongoing efforts involve the use of solid acids as the esterification catalyst that allows for better reactant-product separation, catalyst recovery, and the ability to conduct reactions in continuous, fixed bed reactors [28,61].

Gas-phase esterification reactions have been studied on a variety of solid acids, including silica-supported sulfonic acids [29–33], ion-exchange resins [31,35], metal oxides [31,35,36], heteropolyacids [13], and zeolites [34,35,39–42]. A variety of mono-alkanols, including methanol [29–33,36], ethanol [30,32,37,39,40,62,63], iso-propanol [42,63], butanol [30,35,37,42,64], and benzyl alcohol [41] have been used as the esterifying agent and acetic acid [29–33,35–37,39–42], lactic acid [62], acrylic acid [64], phenylacetic and benzoic acid [63] have been used as the acylating agent. As briefly discussed in the following sections, an outstanding mechanistic question in esterification reactions catalyzed by solid acids is the involvement of one or two surface-bound species.

*Reported from Bedard, J. W.; Chiang, H.; Bhan, A., *Journal of Catalysis*, **290**, 210-219, (2012)

Teo and Saha determined that two surface adsorbates were involved in the rate-determining step of liquid-phase esterification of acetic acid with isoamyl alcohol using cation-exchange resin Purolite CT-175 at temperatures 333–358 K based on their assessment of minimizing the sum of residual squares between experimental and calculated reaction rates [45]. Miao and Shanks also propose a mechanism with a kinetically relevant step involving reaction of two surface adsorbates for liquid-phase esterification of acetic acid with methanol using propylsulfonic acid-functionalized SBA-15 at near ambient temperatures (303–333 K) based on the initial reaction rate being second order in the concentration of acid sites [65].

In contrast, Altiokka and Citak proposed that esterification reactions of acetic acid and isobutanol catalyzed by cation-exchange resin Amberlite IR-120 at temperatures 318–348 K occur via a single-site Eley-Rideal (ER) pathway in which an adsorbed alcohol molecule reacts with an acid molecule from the bulk phase [48]. Goodwin and co-workers determined through pyridine poisoning experiments that both gas-phase (363–413 K) and liquid-phase (333 K) esterification of acetic acid by ethanol and methanol using silica supported Nafion (SAC-13) proceeded through the single site ER pathway [29,32]. Chu and co-workers investigated vapor-phase esterification of acetic acid by ethanol and 1-butanol using heteropolyacid SiW_{12} catalysts at temperatures of 358–433 K and concluded that ethanol followed a two-site mechanism. while butanol followed the Eley-Rideal mechanism [37].

Specifically on zeolites, both Eley-Rideal and two-site mechanisms have been postulated for esterification. Kirumakki and co-workers studied esterification of acetic acid with C_3 and C_4 alcohols using proton-form BEA, FAU, and MFI zeolites at temperatures 383–403 K [42]. They observed a decrease in initial rate with an increase of alcohol concentration suggesting that the alcohol blocks adsorption of acetic acid and thus acid adsorption was necessary for esterification. From these observations, they concluded that ester formation occurs via an ER pathway by which an activated acetic acid molecule reacts with the alcohol from the bulk phase. Koster and co-workers investigated the gas-phase esterification of acetic acid and ethanol using MCM-41 at temperatures 398–473 K [34]. They pre-adsorbed one reactant, ethanol or acetic acid, then introduced the other reactant and observed through transient mass spectrometric analysis that ethyl acetate only formed after the pre-adsorbed reactant desorbed allowing the second reactant to adsorb. From these observations, they concluded that both reactants must be adsorbed on the surface and that the reaction

proceeded through the two-site pathway. They also reacted O^{18}-labeled acetic acid with O^{16}-ethanol and observed only $O^{16}O^{18}$-ethyl acetate and H_2O^{18} and no $O^{18}O^{18}$-ester, which lead them to conclude that the reaction progressed through a protonated acid surface species followed by nucleophilic attack by an alcohol molecule. Therefore, an outstanding mechanistic question on esterification catalyzed by acidic heterogeneous catalysts is whether the reaction proceeds via a dual-site pathway or a single-site ER pathway.

In this work, the mechanism of acetic acid and ethanol esterification over zeolites was examined using kinetic measurements. Four zeolite framework materials (H-BEA, H-FER, H-MFI, and H-MOR) were chosen to study the effects of zeolite pore size and connectivity on the kinetics and mechanism of esterification. Measured kinetic effects of acetic acid and ethanol pressure on ethyl acetate formation over these four zeolites are consistent with a mechanism that involves the formation of a co-adsorbed complex of acetic acid and ethanol and reaction of this co-adsorbed complex to produce ethyl acetate. The marked effects of zeolite structure on measured rates of esterification can be rigorously interpreted in terms of a kinetic parameter for esterification and a ratio of equilibrium constants that reflects the propensity to form an acetic acid/ethanol complex versus that to form ethanol dimers.

2.2 Materials and methods

2.2.1 Catalyst preparation

BEA (Si/Al = 12.0, CP 814E), FER (Si/Al = 11.5, CP 914C), MFI (Si/Al = 13.2, CBV 2314), and MOR (Si/Al = 11.1, CBV 21A) zeolite samples were obtained from Zeolyst International in their ammonium form. The silicon to aluminum ratio was determined by elemental analysis (Galbraith Laboratories). The zeolites were sieved to attain particle sizes between 180 and 425 μm (40-80 mesh) and subsequently treated in dry air (1.67 cm^3 s^{-1} at NTP conditions, ultrapure, Minneapolis Oxygen) to thermally decompose NH_4^+ to H^+ and $NH_{3(g)}$ by increasing the temperature from ambient to 773 K at 0.0167 K s^{-1} and holding at 773 K for 4 h. The protonated BEA, FER, MFI, and MOR zeolites are abbreviated as H-BEA, H-FER, H-MFI, and H-MOR, respectively. The structural and chemical characterization of these materials was accomplished by scanning and transmission electron microscopy, X-ray diffraction, N_2 physisorption, and titration by dimethyl ether. These data have been reported in section 2.5 and shown in Table 2.1.

Table 2.1 Physical properties for catalyst samples used in this study. (a) ICP-OES elemental analysis as performed by Galbraith Laboratories. (b) Adsorbed DME per Al atom on zeolites at 438 K. (c) BET parameters fit to nitrogen adsorption data.

Zeolite sample (Si/Al)	Largest channel sizes (Å)	Si/Al (ICP-OES)[a]	DME/Al[b]	BET Surface Area (m^2g^{-1})[c]	BET micropore Volume (cc/g)[c]
H-FER (10)	10-MR 4.2 x 5.4 8-MR 3.5 x 4.8	11.5	0.45	317	0.16
H-MFI (11.5)	10-MR 5.1 x 5.5 10-MR 5.3 x 5.6	13.2	0.49	286	0.12
H-MOR (10.5)	12-MR 6.5 x 7.0 8-MR 2.6 x 5.7	11.1	0.48	424	0.21
H-BEA (12)	12-MR 6.6 x 6.7 12-MR 5.6 x 5.6	12.0	0.42	579	0.19

[a] ICP-OES elemental analysis as performed by Galbraith Laboratories.

[b] Adsorbed DME per Al atoms on zeolites at 438 K.

[c] PET parameters fit to nitrogen adsorption data.

2.2.2 Steady-state catalytic reaction of acetic acid/ethanol mixtures

Steady-state esterification reactions of acetic acid (AcOH) and ethanol (EtOH) were conducted in a fixed bed, tubular stainless steel reactor (8 mm inner diameter) at atmospheric pressure and differential conditions (<10% conversion). Zeolite samples were diluted with acid-washed quartz sand (40-100 mesh, Acros) to maintain a catalyst bed volume of 1 cm^3. The catalyst bed was made stationary within the tubular reactor by sandwiching it between quartz wool (Perkin Elmer). Isothermal reaction temperature was set by a three-zone split tube furnace (Series 3210, Applied Test System) controlled by three Watlow temperature controllers (96 series) with K-type thermocouple feedback (Omega Engineering). A thermowell was installed in the reactor such that a thermocouple could be placed in thermal contact with the catalyst bed to record the reaction temperature. Prior to conducting esterification reactions, catalyst samples were pretreated in He (0.67 $cm^3\ s^{-1}$, ultrapure, Minneapolis Oxygen) by increasing the temperature from ambient to 773 K at 1.5 K s^{-1} and holding at 773 K for 3 h prior to cooling the catalyst bed in He flow to the desired reaction temperature. Ethanol (Pharmco-Aaper, 99.98%) and acetic acid (Fluka, >99.8%) were introduced to flowing gas streams using separate liquid infusion pumps (Model

100, KD Scientific). Liquid EtOH (6.67–13.3 x 10^{-3} cm^3 s^{-1}) and liquid AcOH (3.33–5.56 x 10^{-3} cm^3 s^{-1}) were vaporized at 423 K in heated transfer lines containing gas flows of He (0.38–0.44 cm^3 s^{-1} at NTP conditions) and a mixture of Ar/CH_4 (0.33 cm^3 s^{-1} at NTP conditions, 10% CH_4 and 90% Ar, Airgas) as internal standards. Transfer lines were kept at temperatures greater than 393 K by resistive heating to ensure that no condensation of liquid reactants occurred. Partial pressures of EtOH and AcOH were changed by adjusting the liquid flow rate on the syringe pump while also adjusting the He flow rate to keep the total gaseous flow rate constant at 0.83 cm^3 s^{-1}. The reactor effluent was sent via heated transfer lines to a gas chromatograph (Agilent 6890N GC) equipped with a bonded polystyrene-divinylbenzene capillary column (HP-PLOT/Q, 30.0 m x 0.530 mm x 40.0 μm, Agilent) connected to a flame ionization detector. Reaction rates were measured as a function of temperature (323–393 K) and reactant pressure (P_{AcOH} = 0.5–6.0 kPa, P_{EtOH} = 5.0–13.0 kPa).

2.3 Results and discussion

Ethyl acetate (EA), the esterification product of acetic acid and ethanol reactions, was observed on H-BEA (Si/Al = 12.0, T = 323–353 K, P_{EtOH} = 5–11 kPa, P_{AcOH} = 0.5–4 kPa), H-FER (Si/Al = 11.5, T = 343–383 K, P_{EtOH} = 5–11 kPa, P_{AcOH} = 1–6 kPa), H-MFI (Si/Al = 13.2, T = 343–383 K, P_{EtOH} = 5–11 kPa, P_{AcOH} = 1–5 kPa), and H-MOR (Si/Al = 11.1, T = 323–353 K, P_{EtOH} = 7–13 kPa, P_{AcOH} = 0.5–4 kPa) with greater than 90% selectivity. Small amounts of ethylene and diethyl ether (<10% selectivity) were produced but did not affect the determination of mechanistic pathways. In the following sections, we present a discussion of the mechanistic cycle for acetic acid/ethanol esterification reactions over different zeolite materials and interpret the marked effects of zeolite structure in terms of experimentally obtained kinetic and thermodynamic parameters.

2.3.1 Kinetics and mechanism of acetic acid esterification by ethanol

The measured rates of EA synthesis over H-BEA, H-FER, H-MFI, and H-MOR as a function of AcOH and EtOH pressure are shown in Figures 2.1-2.4. The reaction rate increases with increasing AcOH pressure, suggesting that AcOH is involved in the rate-determining step; the rate decreases with increasing EtOH pressure, suggesting EtOH inhibits the reaction through prevalence of EtOH-derived species on the catalyst surface, over all four zeolites. Three mechanisms would account for these observed pressure dependencies. The first

involves EtOH adsorption on a Brønsted acid site followed by activation and reaction with AcOH and is referred to as the ethoxide mechanism (Figure 2.5). The second mechanism involves AcOH adsorption on a Brønsted acid site followed by activation and reaction with EtOH and is referred to as the acetyl mechanism (Figure 2.6). The third mechanism involves co-adsorption of AcOH and EtOH which react to form EA and is referred to as the co-adsorption mediated mechanism (Figure 2.7). All three mechanisms would result in EA synthesis rates being enhanced by increasing AcOH pressure and inhibited by EtOH dimer formation on the active sites, which accounts for the negative EtOH pressure dependence observed in reaction studies. In infrared spectroscopic experiments, Zecchina and co-workers observed that when the ratio of adducts to zeolitic hydroxyl groups was greater than 1:1, (i) the intensity of the background (3500–1300 cm^{-1}) and the Evans window increased, (ii) a strong adsorption band centered at 1650–1600 cm^{-1} formed and broadened below 1300 cm^{-1}, and (iii) the intensity of the A component band (~2980 cm^{-1}) decreased while the B component band (~2450 cm^{-1}) broadened [66]. Based on these observations, the authors concluded that methanol and ethanol dimer species are formed upon adsorption in H-MFI and H-MOR zeolites. The invariance in the differential heat of adsorption of ethanol (~130 kJ mol^{-1}) at ethanol per aluminum coverages greater than 1 on H-MFI led Lee and co-workers to conclude that ethanol dimers are adsorbed on Brønsted acid sites in H-MFI, facilitated by the ability of ethanol to act as both a hydrogen-bond acceptor and donor [67]. Kinetic and isotopic experiments for ethanol dehydration over H-FER, H-MFI, and H-MOR by Chiang and co-workers showed that the observed pressure dependence and secondary kinetic isotope effects for diethyl ether formation could be rigorously described by a mechanistic cycle which involves the formation of ethanol dimers on the surface and a kinetically relevant step that involves activation of the dimer to form diethyl ether [68]. Based on these observations for dimer formation in reactions of alkanols on zeolites at similar temperature and pressure conditions as used in our work, we anticipate the formation of dimers and have proposed reaction pathways to reflect this. In the following section, we discuss the mechanistic evidence in support of the three proposed reaction cycles depicted in Figures 2.5-2.7 and on the basis of experimental observations and analysis of corresponding rate expressions, distinguish and contrast the three proposed mechanisms.

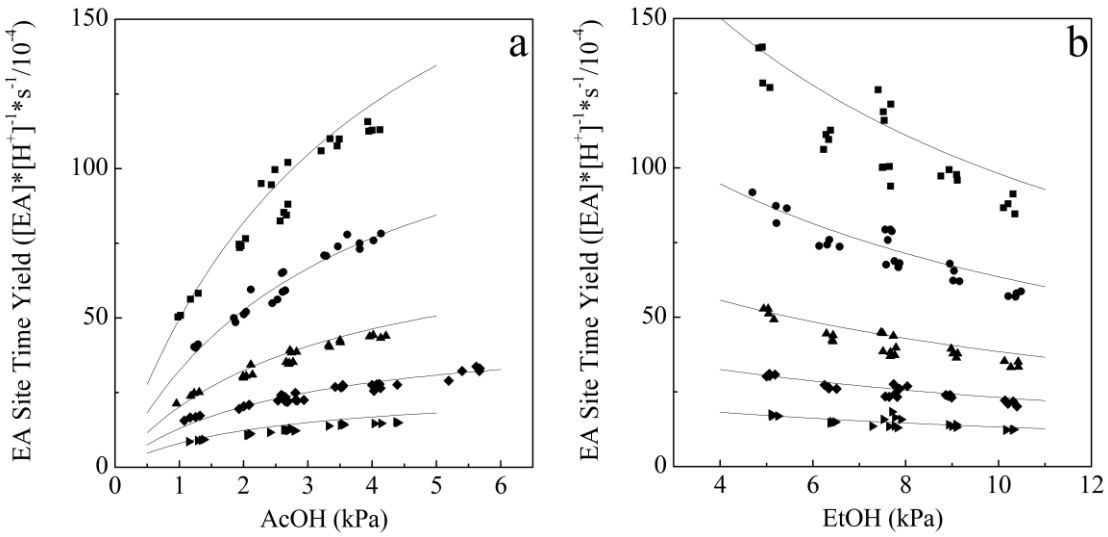

Figure 2.1 Measured ethyl acetate (EA) synthesis rate as a function of acetic acid (a, P_{EtOH} = 10.5 kPa) and ethanol (b, P_{AcOH} = 2.6 kPa) pressure over H-MFI (Si/Al = 13.2) at 343 K (►), 353 K (♦), 363 K (▲), 373 K (●), and 383 K (■). The solid lines represent predictions from Equation 2.4.

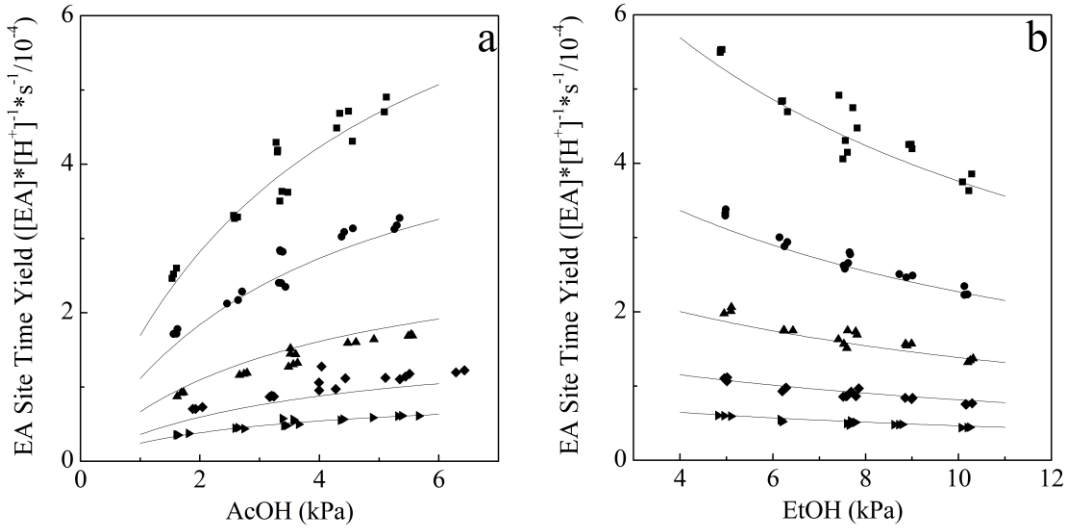

Figure 2.2 Measured ethyl acetate (EA) synthesis rate as a function of acetic acid (a, P_{EtOH} = 12.4 kPa) and ethanol (b, P_{AcOH} = 2.5 kPa) pressure over H-FER (Si/Al = 11.5) at 343 K (►), 353 K (♦), 363 K (▲), 373 K (●), and 383 K (■). The solid lines represent predictions from Equation 2.4.

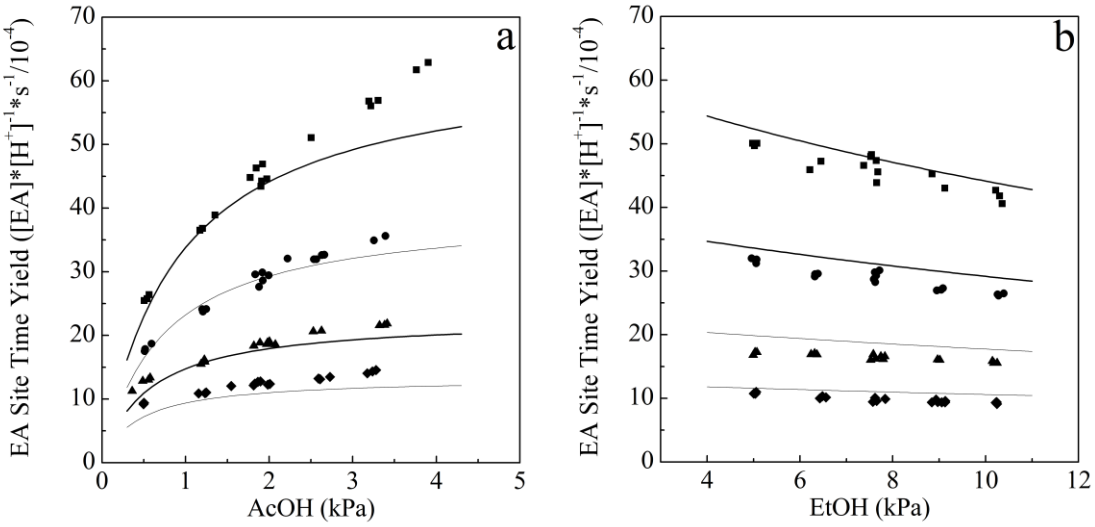

Figure 2.3 Measured ethyl acetate (EA) synthesis rate as a function of acetic acid (a, P_{EtOH} =10.3 kPa) and ethanol (b, P_{AcOH} =1.9 kPa) pressure over H-BEA (Si/Al = 12.0) at 323 K (♦), 333 K (▲), 343 K (●), and 353 K (■). The solid lines represent predictions from Equation 2.4.

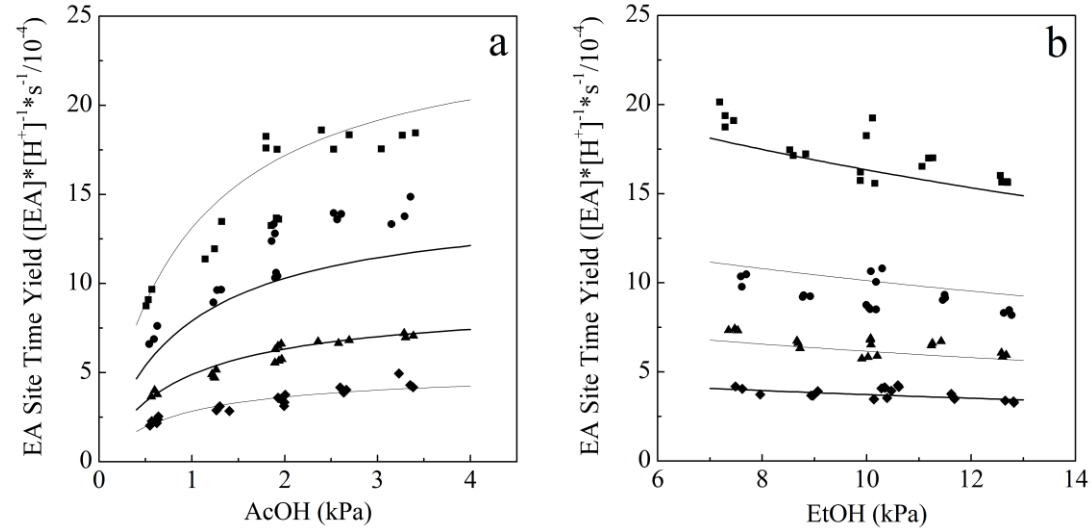

Figure 2.4 Measured ethyl acetate (EA) synthesis rate as a function of acetic acid (a, P_{EtOH} = 10.1 kPa) and ethanol (b, P_{AcOH} = 1.9 kPa) pressure over H-MOR (Si/Al = 11.1) at 323 K (♦), 333 K (▲), 343 K (●), and 353 K (■). The solid lines represent predictions from Equation 2.4.

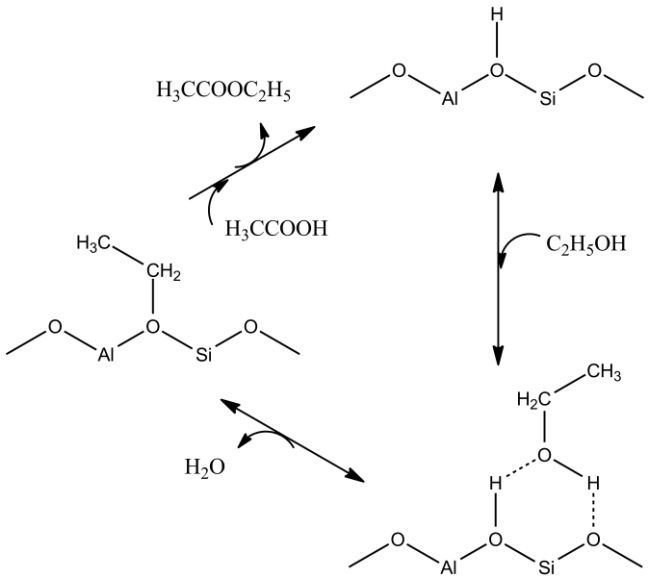

Figure 2.5 Proposed elementary steps for EA formation via EtOH activation to form a surface alkoxide and subsequent reaction with AcOH. This mechanism is referred to as the ethoxide mechanism.

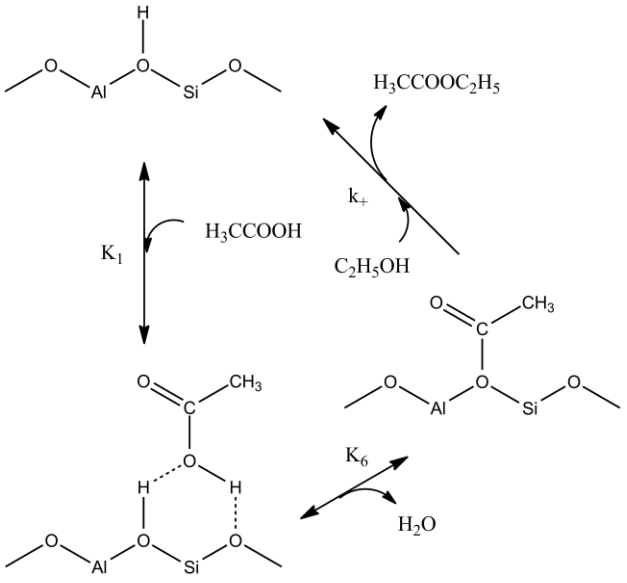

Figure 2.6 Proposed elementary steps for EA formation via AcOH activation to form a surface acetyl and subsequent reaction with EtOH. This mechanism is referred to as the acetyl mechanism.

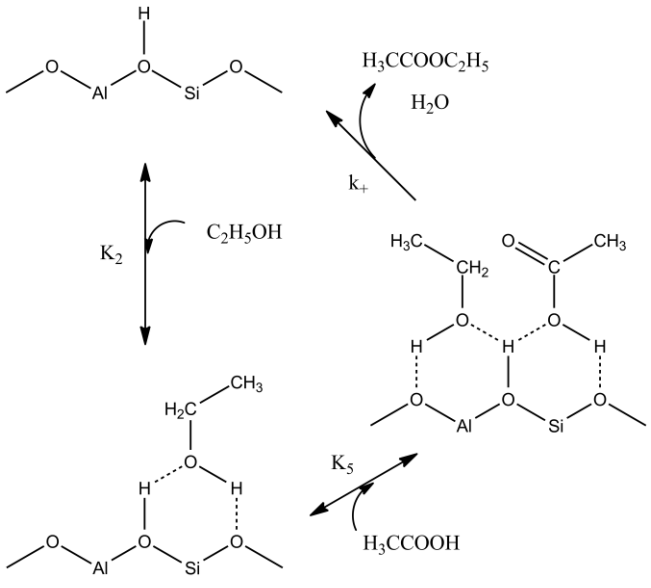

Figure 2.7 Proposed elementary steps for EA formation via reaction of co-adsorbed AcOH/EtOH complex on the surface. This mechanism is referred to as the co-adsorption mediated mechanism.

Besides forming dimers, ethanol can also decompose to water and a surface-bound ethoxide species on Brønsted acid sites in zeolites (Figure 2.5). ^{13}C cross-polarization/magic-angle spinning NMR experiments by Wang and co-workers showed the appearance of a new species at 72.6 ppm upon heating a H-Y zeolite sample pre-dosed with ethanol to 453 K while removing water and physisorbed ethanol with N_2 flow [69]. The authors assigned this observed chemical shift to a surface-bound ethoxide species, $SiO(CH_2CH_3)Al$, formed upon dehydration of ethanol. Ethylene, upon adsorption on Brønsted acid sites of proton-form zeolites, also forms ethoxide species with sp^3 hybridization of the C bonded to the zeolite surface O and significant covalent bond character as shown for H-Y by Namuangruk and co-workers using a 84T cluster modeled by the ONIOM3 (MP2/6-311++G(d,p):HF/6-31G(d):UFF) method [70]. Ethylene adsorbs weakly (-8.7 kcal/mol) on the hydroxyl group of the zeolite via π-interactions and protonation of ethylene leads to the formation of the surface-bound ethoxide species. If EA forms by the ethoxide mechanism involving the formation of a surface ethoxide by dehydration of ethanol (Figure 2.5), it should also form when ethylene is used as a co-reactant with acetic acid. No EA formation was observed when introducing 1.3 kPa of AcOH and up to 23 kPa of C_2H_4 using 3.0 mg of H-BEA at 353 K, hence we conclude that under our

reaction conditions, EA is not formed via the ethoxide mechanism depicted in Figure 2.5. Koster and co-workers co-reacted $H_3CCO^{18}O^{18}H$ and C_2H_5OH over MCM-41 at 448 K and observed H_2O^{18} and $H_3CCO^{18}OC_2H_5$ production but no $H_3CCO^{18}O^{18}C_2H_5$ was formed [34]. If EA was formed through the ethoxide mechanism, it would be doubly ^{18}O labeled so the authors concluded that esterification proceeds through a protonated AcOH molecule rather than EtOH adsorption on MCM-41 catalysts. Based on these reports and our data with ethylene co-feed, the ethoxide mechanism can be ruled out so the acetyl and co-adsorbed complex mediated pathways (Figures 2.6 and 2.7) were further investigated by deriving mechanistic rate equations for EA production.

Two elementary steps in the acetyl mechanism that involve AcOH could be the potential rate-determining step (RDS) for this mechanism: AcOH activation and product formation. Rate expressions were derived using elementary steps and assuming all steps involving the formation of intermediates are quasi-equilibrated. Equations 2.1 and 2.2 are the rate equations for the acetyl mechanism (Figure 2.6) with product formation and AcOH activation being the RDS, respectively. The intrinsic rate constant and equilibrium constants are designated as k_+ and K_i, respectively, while the concentration of free acid sites, AcOH, and EtOH are labeled as $[H_0]$, $[AcOH]$, and $[EtOH]$ respectively. These derivations are reported in section 2.5. The expressions have been simplified by neglecting the rate dependence on EA concentration because low concentrations of EA result (<0.1 kPa) under differential conversion (<10%) conditions.

$$\frac{r}{[H_0]} = \frac{\dfrac{k_+ K_1 K_6 [AcOH][EtOH]}{[H_2O]}}{1 + \dfrac{K_1 K_6 [AcOH]}{[H_2O]} + K_1[AcOH] + K_2[EtOH] + K_2 K_3 [EtOH]^2 + K_2 K_5 [AcOH][EtOH]} \quad (2.1)$$

$$\frac{r}{[H_0]} = \frac{k_+ K_1 [AcOH]}{1 + K_1[AcOH] + K_2[EtOH] + K_2 K_3 [EtOH]^2 + K_2 K_5 [AcOH][EtOH]} \quad (2.2)$$

Inspection of Equation 2.1 shows that water should inhibit the rate of EA synthesis; however, our experimental data suggest otherwise. Experiments were conducted with increasing catalyst mass to effectively increase the conversion which resulted in an increased concentration of EA and H_2O in the effluent, while keeping all other parameters constant (P_{EtOH} = 10.5 kPa, P_{AcOH} = 2.6 kPa and T = 353 K). EA pressure was used to infer the H_2O pressure based on the 1:1

Table 2.2 Effect of increased EA pressure on the rate of EA formation at 353 K on H-BEA.

Catalyst mass (mg)	EA Pressure (kPa)	EA TOF ($/10^{-4}$ mol EA (mol H^+)$^{-1}$ s^{-1})
6.1	0.11	63
9.5	0.16	62
12.4	0.22	62

stoichiometry of EA/H_2O in the selective AcOH esterification by EtOH. Increased EA pressure, and therefore increased H_2O pressure, had no effect on measured EA synthesis rates as shown in Table 2.2.

An independent set of experiments was conducted in which H_2O was co-fed with EtOH and AcOH to probe the effects of directly introducing water on EA formation rates under experimental conditions. Water was co-fed at partial pressures similar to those produced at reaction conditions with no H_2O co-feed (P_{H2O} = 0.04 kPa). No significant change (<10%) in EA synthesis rate was observed upon addition of H_2O on all four zeolites, as shown in Table 2.3. The data for these water co-feed experiments at varying AcOH pressure have been reported in section 2.5 (Figure 2.18). Ison and Gorte reported that in co-adsorption experiments of water and methanol on H-ZSM-5, methanol could rapidly displace adsorbed water while water could not displace adsorbed methanol [71]. Considering our experimental results at low conversion and therefore, low partial pressure of water, as well as the adsorption study by Ison et al., water does not have a significant effect on the synthesis of EA at these reaction conditions. Equation 2.1 is inconsistent with the observed effect of H_2O pressure on measured reaction rates, therefore, product formation in the acetyl mechanism was disregarded as a potential kinetically relevant step for the formation of EA.

Equation 2.2 and AcOH activation cannot be ruled out by this logic as it has no dependence on H_2O pressure. The terms in the denominator correspond to the fraction of surface sites occupied by empty sites, AcOH monomers $K_1[AcOH]$, EtOH monomers $K_2[EtOH]$, EtOH dimers $K_2K_3[EtOH]^2$, or co-adsorbed AcOH/EtOH complexes $K_2K_5[AcOH][EtOH]$. Any of these species can dominate the surface; rate expressions corresponding to one or two dominating species were derived for all cases and are shown in section 2.5.

Table 2.3 Effect of water co-feed on the rate of EA formation at P_{EtOH} = 10.2, P_{AcOH} = 3.0, and T = 363 K.

Catalyst	EA TOF, P_{H2O} = 0.0 kPa ($/10^{-4}$ mol EA (mol H^+)$^{-1}$ s^{-1})	EA TOF, P_{H2O} = 0.04 kPa ($/10^{-4}$ mol EA (mol H^+)$^{-1}$ s^{-1})
H-BEA	64	68
H-FER	1.4	1.4
H-MFI	37	34
H-MOR	23	23

Experimental observations described earlier report a negative dependence in EA synthesis rates on EtOH pressure ranging from -0.5 to -0.3 order and a positive dependence on AcOH pressure ranging from 0.3 to 0.5 order. The range of reaction orders is dependent on prevalent process conditions, including reactant pressure, temperature, and the specific zeolite. Both orders are fractional meaning that EtOH and AcOH terms must be present in the numerator as well as the denominator. An inspection of the rate expressions derived from Equation 2.2 offers no rate equation that is consistent with the experimental data. Therefore, the RDS for esterification cannot be AcOH activation and the acetyl mechanism can be disregarded.

The rate equation for the co-adsorbed complex mediated mechanism (Figure 2.7) with product formation as the RDS is given in Equation 2.3 (see section 2.5 for derivation). This mechanism considers elementary steps of AcOH and EtOH physisorption to form the co-adsorbed AcOH/EtOH complex that subsequently reacts to produce EA and H_2O in the RDS. The quasi-equilibrium assumption is applied to each adsorption step in the mechanism. Substitution affords Equation 2.3 which represents the rate per

$$\frac{r}{[H_0]} = \frac{k_+ K_2 K_5 [AcOH][EtOH]}{1 + K_2[EtOH] + K_1[AcOH] + K_2 K_3 [EtOH]^2 + K_2 K_5 [AcOH][EtOH]} \tag{2.3}$$

active site for the co-adsorbed complex mediated mechanism in terms of vapor-phase reactant concentrations. An analysis of this rate expression corresponding to the predominant prevalence of different surface species is also shown in section 2.5. Two expressions, shown as Equations 2.4 and 2.5, give AcOH and EtOH terms in the numerator and denominator, which would give rise to fractional orders as seen in experimental data. Equation 2.4

$$r = \frac{k_+ K_2 K_5 [AcOH]}{K_2 K_3 [EtOH] + K_2 K_5 [AcOH]} \tag{2.4}$$

$$r = \frac{k_+ K_2 K_5 [AcOH][EtOH]}{K_1 [AcOH] + K_2 K_3 [EtOH]^2} \tag{2.5}$$

corresponds to ethanol dimers, K_2K_3 term, and the co-adsorbed AcOH/EtOH complex, K_2K_5 term, predominantly occupying the active sites under reaction conditions, while Equation 2.5 corresponds to ethanol dimers, K_2K_3 term, and AcOH monomers, K_1 term, as the dominating surface species. Equations 2.4 and 2.5 can be written in a linear form, Equations 2.6 and 2.7 respectively, which can

$$\frac{1}{r} = \frac{K_3 [EtOH]}{k_+ K_5 [AcOH]} + \frac{1}{k_+} \tag{2.6}$$

$$\frac{1}{r} = \frac{K_3 [EtOH]}{k_+ K_5 [AcOH]} + \frac{K_1}{k_+ K_2 K_5 [EtOH]} \tag{2.7}$$

then be plotted to determine their ability to describe the kinetic effects of AcOH and EtOH pressure on EA formation. Both reciprocal rate expressions give an inverse dependence of rate on AcOH pressure and the slopeof a linear trendline of 1/r versus $1/[AcOH]$ for either expression is directly proportional to the EtOH pressure. There is an effect of EtOH pressure on the Y-intercept of these linear fits as Equation 2.6 has no dependence, while the Y-intercept of Equation 2.7 is inversely proportional to the EtOH pressure. An independent set of experiments was conducted at varying AcOH pressure, constant temperature, and constant EtOH pressure to determine the effect of EtOH pressure on the Y-intercept of the linear fit predicted from Equations 2.6 and 2.7. Table 2.4 shows the value of the y-intercept of a linear trendline fit to reciprocal rate data (1/r) as a function of $1/[AcOH]$ at constant EtOH pressure. The Y-intercept value is invariant with EtOH pressure, which is consistent with Equation 2.6. This analysis supports Equation 2.4 that corresponds to the co-adsorbed complex dominating on the surface rather than AcOH monomers as being consistent with our experimental data recorded at varying EtOH and AcOH pressures and varying temperatures on H-BEA, H-FER, H-MFI, and H-MOR.

Although experimental reports that specifically probe the stability and existence of monomeric and dimeric intermediates in esterification reactions under conditions relevant for catalysis are elusive, computational chemistry methods have been employed to determine the relative stability of monomeric

Table 2.4 Y-intercept values from the linear trendline of a 1/r vs. 1/[AcOH] plot at different constant [EtOH] with P_{AcOH} = 1.0 – 5.0 and T = 353 K.

EtOH Pressure (kPa)	Y-intercept (/10^2 (mol H^+) s (mol EA)$^{-1}$)
7.8	7.2
9.0	8.1
10.4	7.9
11.7	8.1

and dimeric complexes in reactions of alkanols and olefins on zeolites. Density functional theory (DFT) calculations by Blaszkowski and van Santen on a 3T cluster have shown that adsorption of a methanol dimer (-130 kJ mol^{-1}) is stronger than the adsorption of a methanol monomer (-75 kJ mol^{-1}) [72]. A similar study by Svelle and co-workers using a hybrid MP2:DFT method with an H-ZSM-5 unit cell has shown that the co-adsorption of methanol and ethene (-37 kJ mol^{-1}) is stronger than the adsorption of ethene alone (-24 to -31 kJ mol^{-1}) [73]. These computational results along with the infrared spectroscopic [66], calorimetric [67], and kinetic [68] experimental observations on the formation of EtOH dimers discussed previously suggest that the co-adsorption of dimers is more stable than adsorption of monomers, and this argument can be used to support the notion that AcOH/EtOH complexes will be more prevalent on the surface as compared to AcOH monomers such that Equation 2.4 would better describe the observed kinetics than Equation 2.5.

Equation 2.6, the linearized form of Equation 2.4, predicts that the reciprocal rate should both be a function of EtOH pressure and inverse AcOH pressure. Figures 2.8-2.11 show these plots for H-MFI, H-FER, H-BEA, H-MOR zeolites studied here at multiple temperatures. Consistent with this prediction, it is observed that the reciprocal rate is linear with [EtOH] or 1/[AcOH] whether the EtOH or AcOH pressure is varied at constant pressure of the other co-reactant. From the linear regression of these data, the intrinsic rate constant, k_+, as well as a quotient of equilibrium constants, K_5/K_3 which reflects the tendency of forming the AcOH/EtOH co-adsorbed complex over EtOH dimers, can be obtained. The values of k_+ and K_5/K_3 can be plotted as a function of inverse temperature (Figure 2.12) to obtain thermodynamic values that can be used to calculate k_+ and K_5/K_3 at a given temperature. These values can then be used in Equation 2.4 to predict the EA synthesis rate as a function of AcOH and EtOH concentration. Essentially invariant kinetic parameters, k_+ and K_5/K_3, are obtained from data where AcOH or EtOH pressure was varied in independent

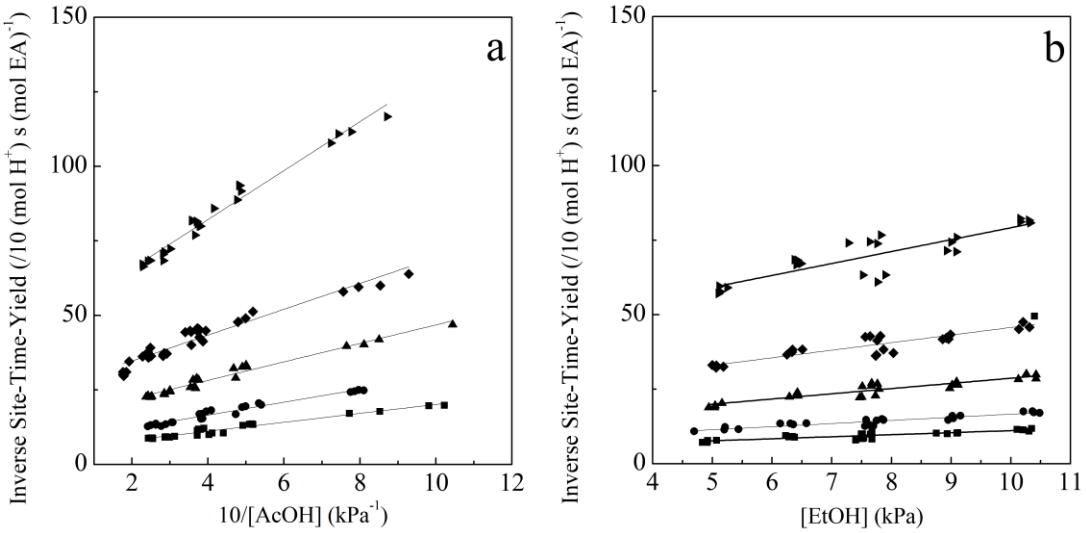

Figure 2.8 Inverse rate of ethyl acetate (EA) synthesis as a function of inverse acetic acid (a, P_{EtOH} = 10.5 kPa) and ethanol (b, P_{AcOH} = 2.6 kPa) pressure over H-MFI (Si/Al = 13.2) at 343 K (▶), 353 K (♦), 363 K (▲), 373 K (●), and 383 K (■). The solid lines are calculated linear regressions.

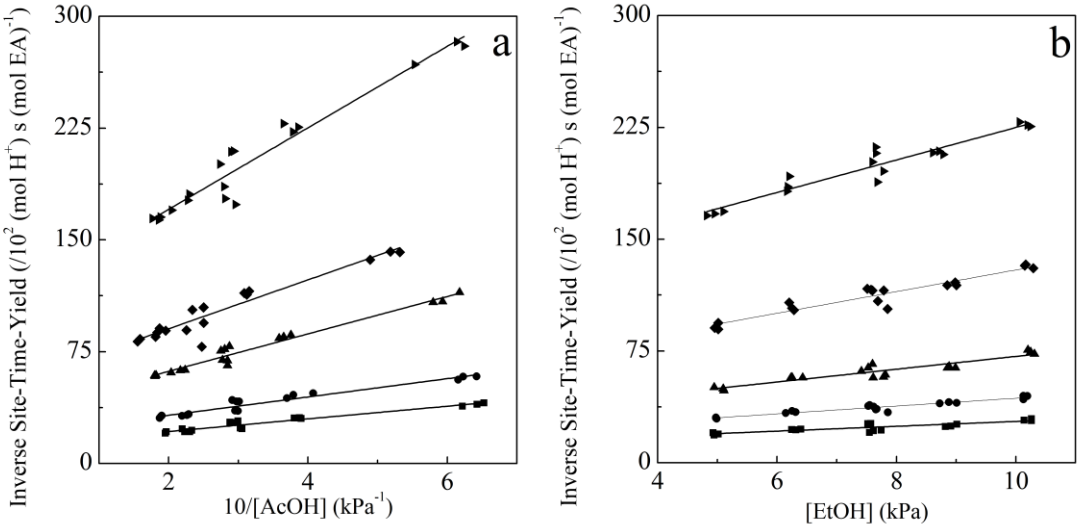

Figure 2.9 Inverse rate of ethyl acetate (EA) synthesis as a function of inverse acetic acid (a, P_{EtOH} = 12.4 kPa) and ethanol (b, P_{AcOH} = 2.5 kPa) pressure over H-FER (Si/Al = 11.5) at 343 K (▶), 353 K (♦), 363 K (▲), 373 K (●), and 383 K (■). The solid lines are calculated linear regressions.

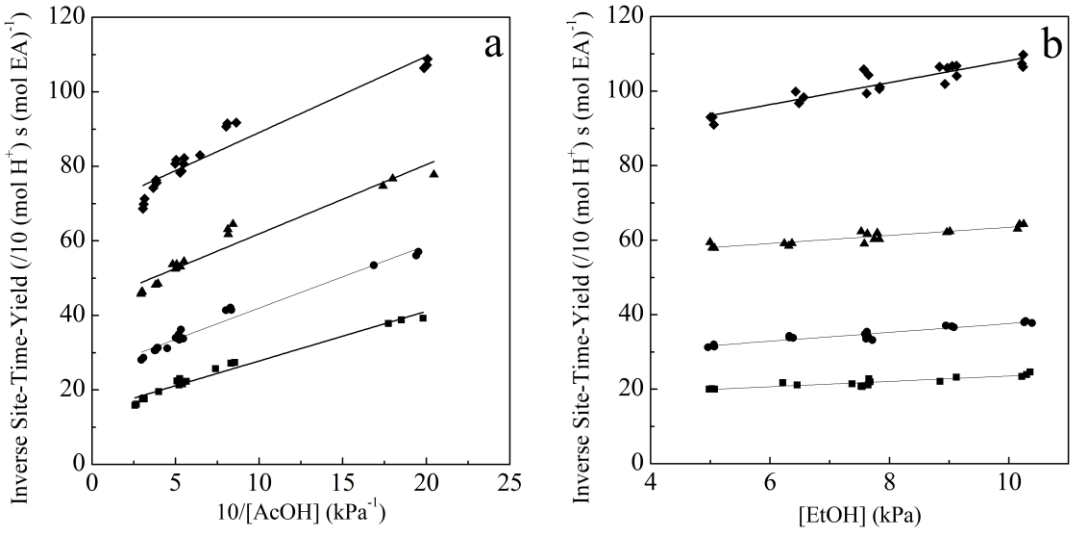

Figure 2.10 Inverse rate of ethyl acetate (EA) synthesis as a function of inverse acetic acid (a, P_{EtOH} = 10.3 kPa) and ethanol (b, P_{AcOH} = 1.9 kPa) pressure over H-BEA (Si/Al = 12.0) at 323 K (♦), 333 K (▲), 343 K (●), and 353 K (■). The solid lines are calculated linear regressions.

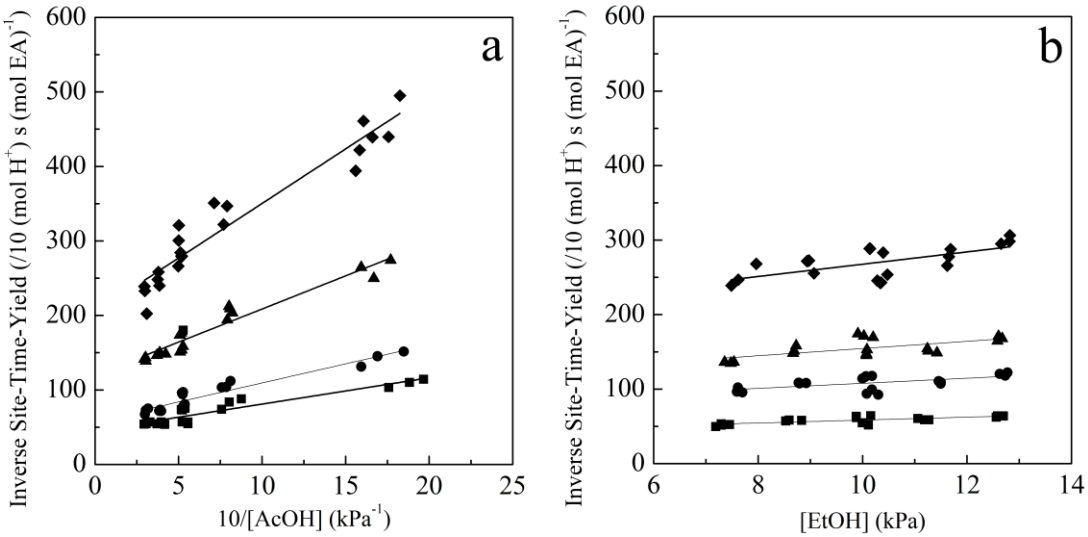

Figure 2.11 Inverse rate of ethyl acetate (EA) synthesis as a function of inverse acetic acid (a, P_{EtOH} = 10.1 kPa) and ethanol (b, P_{AcOH} = 1.9 kPa) pressure over H-MOR (Si/Al = 11.1) at 323 K (♦), 333 K (▲), 343 K (●), and 353 K (■). The solid lines are calculated linear regressions.

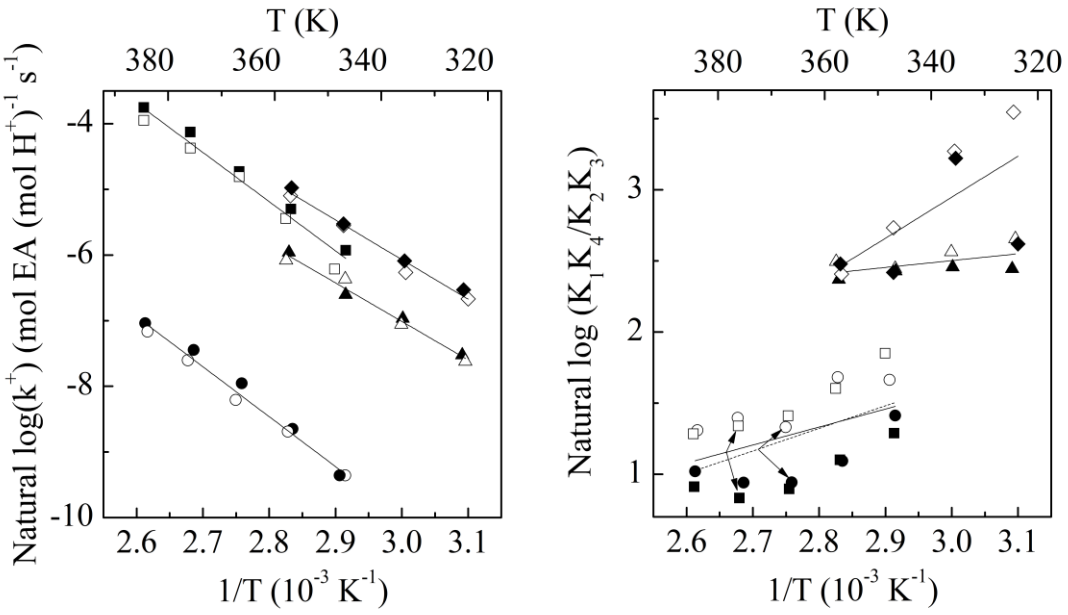

Figure 2.12 Natural log of measured intrinsic rate constant, k_+, and product of equilibrium constants, K_5/K_3, over H-BEA (♦,◊), H-FER (●,○), H-MFI (■,□), and H-MOR (▲,Δ). Closed symbols represent data obtained while varying acetic acid pressure; open symbols represent data obtained while varying ethanol pressure. The solid lines are calculated linear regressions.

experimental studies further corroborating our mechanistic inference regarding the involvement and kinetic relevance of AcOH/EtOH dimers (Figure 2.12). Thermodynamic parameters were calculated by using all our data, obtained in independent experiments varying AcOH and EtOH, for each zeolite studied.

Equation 2.4 rigorously and accurately predicts reaction rate as a function of AcOH and EtOH pressures at multiple temperatures for all zeolites used in this study (solid lines in Figures 2.1-2.4). The full mechanistic pathway that is consistent with Equation 2.4 is shown in Figure 2.13. Gas-phase EtOH can adsorb on a Brønsted acid site (K_2) followed by AcOH adsorption (K_5) to form the AcOH/EtOH co-adsorbed complex. The co-adsorbed complex can also form through adsorption of an AcOH molecule first (K_1) followed by subsequent adsorption of an EtOH molecule (K_4). Reaction of the co-adsorbed complex to form EA and H_2O is the RDS (k_+). EtOH dimers are formed by adsorbing two molecules of EtOH (K_3) on the same active site; subsequent dehydration of this ethanol dimer produces diethyl ether.

The mechanistic pathway shown in Figure 2.13 is consistent over all zeolites, therefore, kinetic rate parameters can be directly compared as a function of zeolite structure. Table 2.5 shows the rate and equilibrium parameters determined for the mechanism depicted in Figure 2.13 for each zeolite. Experimental uncertainties were calculated by propagating errors obtained from the slope and Y-intercept of reciprocal plots (Figures 2.8-2.11) with use of the LINEST function in Microsoft Excel. As explained by Calverley, transforming data such that a linear fit can be obtained may result in inaccurate parameter estimates due to loss of the inherent error structure in the original data[74]. Two secondary parameter estimation techniques (i) a weighted least squares method reported by Harris [75] and (ii) Athena Visual Studio (v14.2, W.E. Stewart and M. Caracotsios) were used for non-linear parameter estimation using raw temperature, pressure, and rate data to overcome the limitation of using linear reciprocal plots. These secondary analysis techniques are thoroughly explained in section 2.5. As shown in Table 2.5, all estimated parameters are consistent over the three methods used with small relative errors.

The intrinsic rate constant for activation of the co-adsorbed AcOH/EtOH complex (k_+) increases in the order FER < MOR < MFI < BEA while the ratio of equilibrium constants (K_5/K_3) increases in the order FER ≈ MFI < MOR ≈ BEA. The effects of zeolite structure on the esterification of AcOH by benzyl alcohol and propanol was studied by Kirumakki and co-workers and they report a similar trend where the rate constant for esterification over BEA was greater than MFI in both reaction systems [41,42]. The smaller ratio of equilibrium constants for MFI and FER compared with BEA and MOR (5 versus 11) suggests that the tendency to form the co-adsorbed complex over EtOH dimers is greater on larger pore zeolites (12-membered ring) than on smaller pore zeolites (10-membered ring). The equilibrium constants of forming AcOH/EtOH and EtOH/EtOH dimers cannot be determined separately in this system. Chiang and co-workers reported that equilibrium constants for EtOH dimers on proton-form FER, MFI, and MOR, at similar reaction conditions as reported here, increase with zeolite pore size [68]. This report by Chiang and co-workers for ethanol conversion and our data for ethanol esterification reactions are consistent and suggest that dimeric intermediates are consistentlyprevalent at low temperature conditions in zeolites and are in general more stable in larger pore materials.

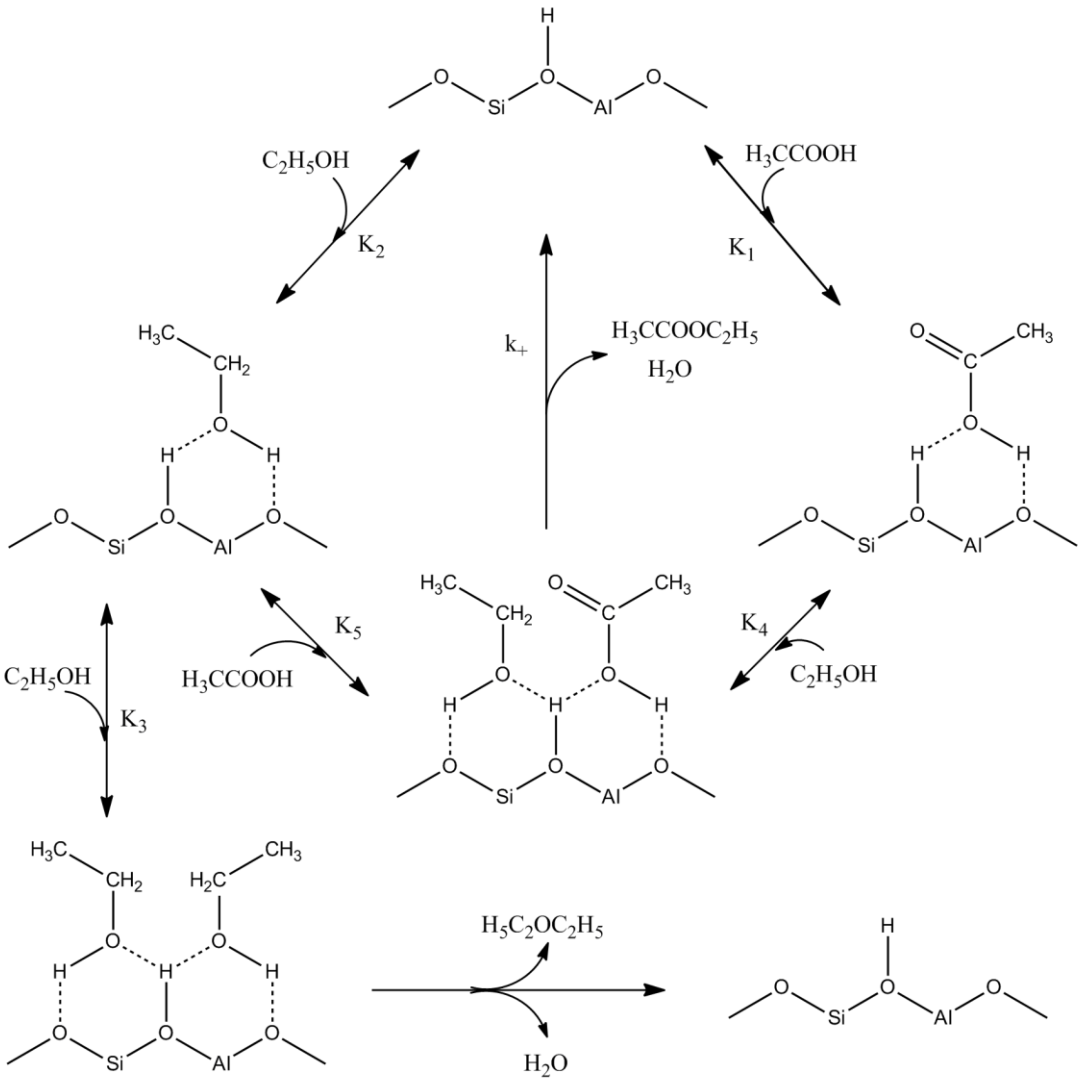

Figure 2.13 Reaction pathway for the production of ethyl acetate from acetic acid and ethanol over proton-form zeolite.

Table 2.5 Rate constants ($\ln[k_+]$), ratio of equilibrium constants ($\ln[K_5/K_3]$), and activation energies (E_{act}) for EA synthesis at 353 K, P_{AcOH} = 1.0 – 6.0 kPa, and P_{EtOH} = 4.0 – 13.0 kPa over the four types of zeolite (Si:Al) framework materials.

BEA (12.0)	$\ln(k_+)$ (mol EA (mol H^+)$^{-1}$ s^{-1})	±	$\ln(K_5/K_3)$	±	E_{act} (kJ/mol)	±
Experimental	-5.03	0.03	2.44	0.11	50.2	2.6
Non-Linear Fit	-4.99	0.09	2.31	0.19	50.1	6.7
Athena V. S.	-5.03	0.06	2.40	0.19	54.1	4.0
MFI (13.2)						
Experimental	-5.38	0.05	1.35	0.15	62.3	4.0
Non-Linear Fit	-5.43	0.10	1.44	0.22	67.0	8.7
Athena V. S.	-5.62	0.10	1.88	0.26	68.2	4.5
MOR (11.1)						
Experimental	-6.02	0.06	2.43	0.18	48.8	2.6
Non-Linear Fit	-6.06	0.15	2.51	0.95	49.8	5.2
Athena V. S.	-6.00	0.09	2.30	0.26	46.3	9.2
FER (11.5)						
Experimental	-8.67	0.05	1.39	0.09	63.3	2.9
Non-Linear Fit	-8.66	0.06	1.37	0.13	63.7	3.6
Athena V. S.	-8.79	0.16	1.62	0.38	68.1	7.2

Our studies in this report show that esterification rates of AcOH by EtOH can be described by a mechanism that proceeds through a surface AcOH/EtOH co-adsorbed complex and that the ethyl acetate synthesis rate is inhibited by surface EtOH dimers on proton-form BEA, FER, MFI, and MOR zeolites. This study resolves the outstanding mechanistic question pertaining to the involvement of one or two surface sites in bimolecular esterification reactions over proton-form zeolites. Our ability to discriminate the effects of zeolite structure on the kinetics of acid catalyzed reactions occurring in their constrained environments depends critically on dissecting chemical reactions into their

elementary steps and concurrently describing the concomitant effects of spatial constraints on the stability of adsorbed intermediates.

2.4 Conclusions

Steady-state catalytic reactions of acetic acid with ethanol over H-BEA, H-FER, H-MFI, and H-MOR at 323–383 K showed that esterification reactions to produce ethyl acetate occur with greater than 90% selectivity on all four zeolites. EA synthesis rates increase with AcOH pressure and decrease with increasing EtOH pressure over all four zeolites, suggesting that both AcOH and EtOH are involved in the rate-determining step. Measured pressure and temperature dependence of reaction rates on all four zeolites can be accurately and rigorously described by a reaction pathway that is consistent with the formation of an energetically favorable AcOH/EtOH complex adsorbed on the zeolite active site. Competitive adsorption of EtOH dimers in this mechanism inhibits the production of the ester product. Kinetic and thermodynamic parameters regressed from this mechanism show that the intrinsic rate constant for activation of the co-adsorbed complex increases in the order FER < MOR < MFI < BEA.

2.5 Supplemental information

2.5.1 Chemical titration by dimethyl ether over zeolites

Chemical titration using dimethyl ether (DME) over H-BEA, H-FER, H-MFI, and H-MOR materials was performed in a tubular packed-bed quartz reactor (10 mm inner diameter) under atmospheric pressure. A mixture of DME/Ar/He (0.17 cm^3 s^{-1}; 24.9% DME, 25.1% Ar and 50% He; Praxair) was introduced by He (0.67 cm^3 s^{-1}, ultrapure, Minneapolis oxygen) during each pulse with 90s intervals. Physisorbed DME and water formed were subsequently removed by He (1.67 cm^3 s^{-1}) for 1.5 to 2.5 hours.

The DME uptake ratio per Al site on the four zeolites is tabulated in Table 2.1. Cheung et al. showed that each Brønsted acid site can adsorb 0.5 DME molecules because DME reacts with surface hydroxyl groups to form persistent methyl groups [76]. From the data in Table 2.1, we infer that the concentration of Brønsted acid sites in the four zeolites used in this study is nearly identical to that inferred from the framework Aluminum content in these materials. The DME titration data reported herein for BEA, FER, MFI, and MOR zeolites has been reproduced from previous work by Chiang et al. [68,77].

2.5.2 Thiele modulus calculation for kinetic versus diffusion control

A Thiele modulus of 0.003 was calculated for the system studied (esterification on H-MFI, first-order k = 0.004 s^{-1}) for 1 micron spherical crystals assuming an effective diffusivity of $4.06*10^{-10}$ m^2 s^{-1} to approximate ethanol diffusion through a zeolite micropore [78]. This confirms that the esterification reactions studied were indeed kinetically limited despite the conservative estimates used.

2.5.3 Structural characterization of zeolite materials

2.5.3.1 Nitrogen adsorption experiments

Nitrogen adsorption/desorption measurements were carried out at 77 K on an Autosorb-1 analyzer (Quantachrome Instruments). Prior to the measurement, samples were evacuated overnight at 573 K and 1 mm Hg. The specific surface area and the pore size distribution were calculated using the Brunauer–Emmett–Teller (BET) and BJH method, respectively. Conventional t-plot methods were used as an extra means for extracting micropore volume and external surface area from the nitrogen adsorption data over t ranges from 3 to 5 Å. The BET equation was used to calculate the BET specific surface area from the adsorption data obtained at P/P_0 between 0.1 and 0.3. Derived values from Liu et al. for BEA, FER, MFI, and MOR zeolites are reproduced in Table 2.1 [79].

2.5.3.2 X-ray diffraction patterns

Powder X-ray diffraction (XRD) patterns were collected on a Bruker AXS D5005 diffractometer using Cu- Kα radiation. Data were collected with a step size of 0.04° and a step time of 3 s. These experiments confirm the crystallinity and identity of the catalyst samples employed.

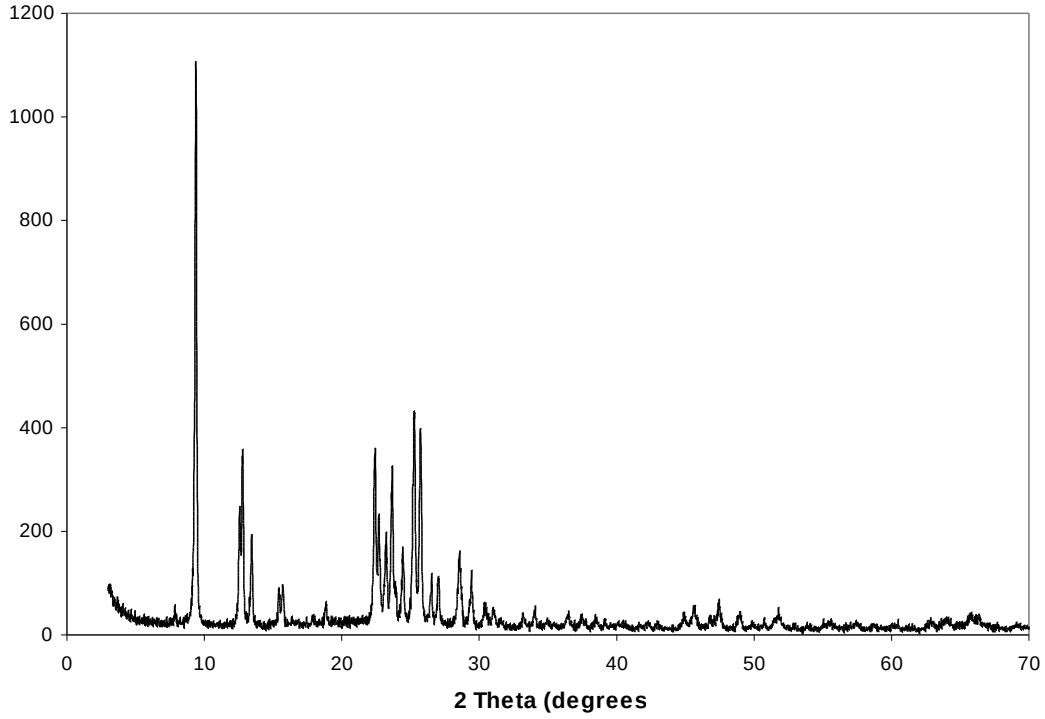

Figure 2.14 XRD pattern for H-FER (Si/Al=11.5).

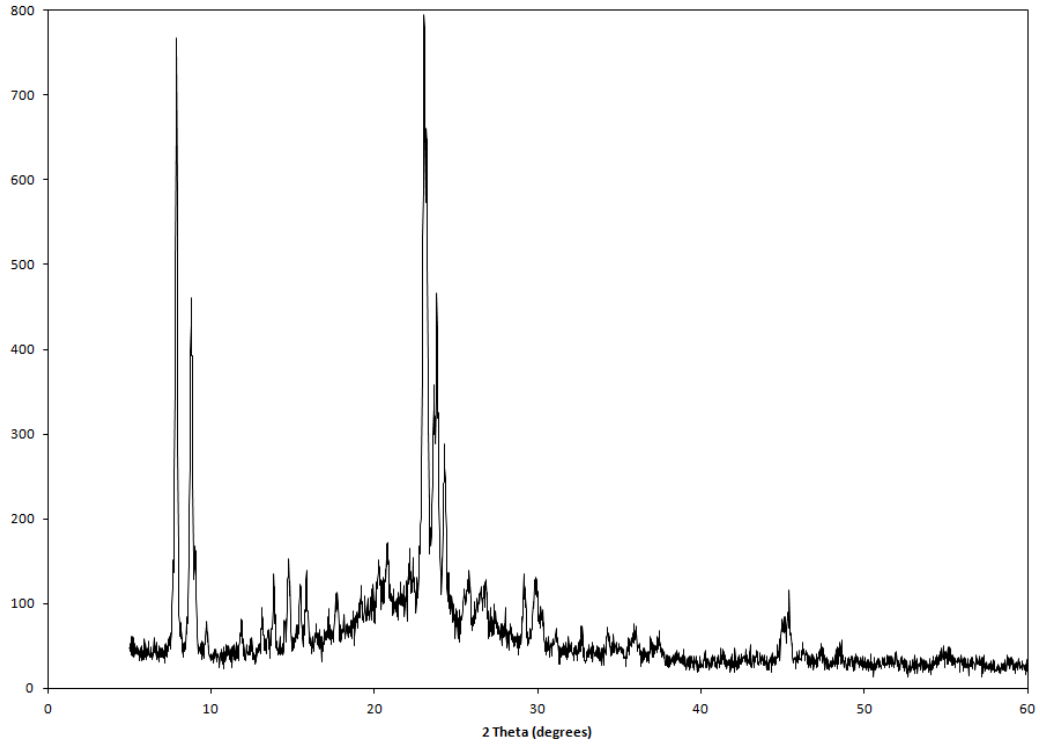

Figure 2.15 XRD pattern for H-MFI (Si/Al=13.2).

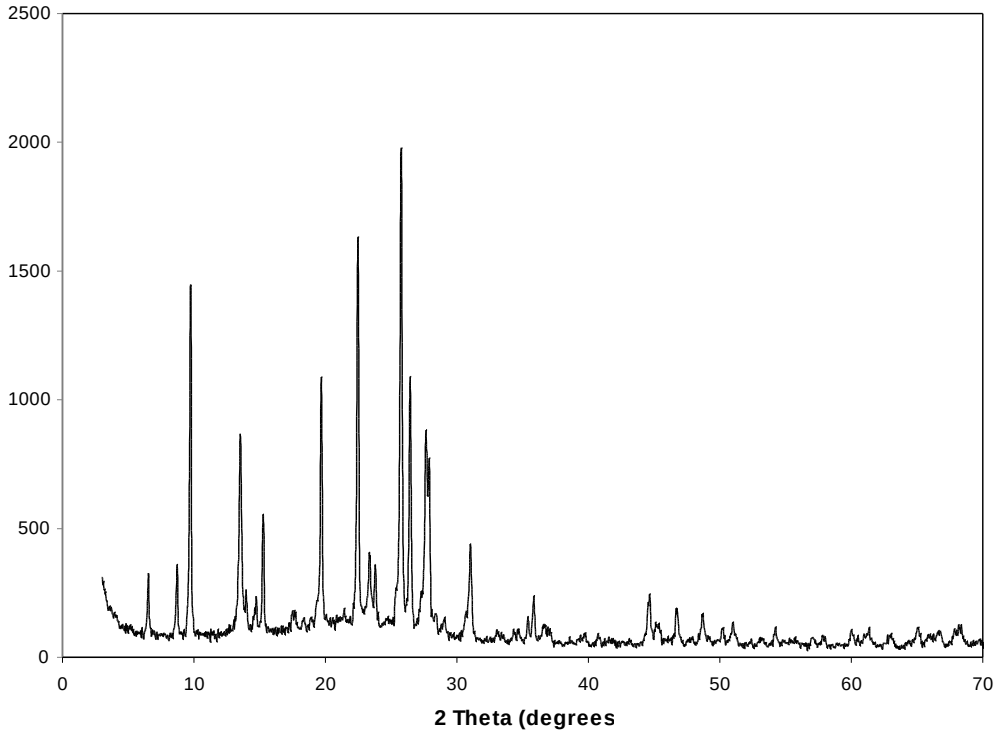

Figure 2.16 XRD pattern for H-MOR (Si/Al=11.1).

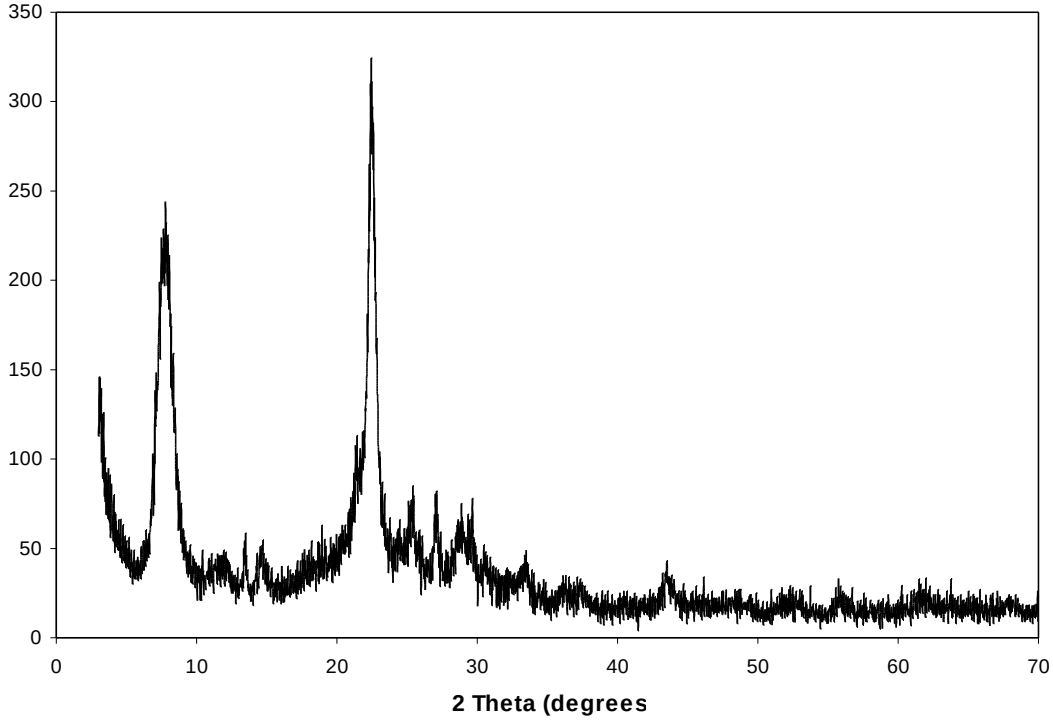

Figure 2.17 XRD pattern for H-BEA (Si/Al=12.0).

2.5.4 Derivation of rate expressions

2.5.4.1 EA synthesis via the acetyl mechanism (Figure 2.6) and product formation as the rate-determining step

AcOH and EtOH can reversibly adsorb on the zeolite acid site as AcOH and EtOH monomers or EtOH and AcOH/EtOH dimers. These adsorption steps are expressed as equations 2.8 – 2.12. Forward rate constants are expressed as k_i, reverse rate constants are expressed as k_{-i}, and Brønsted acid site are expressed as H^+.

$$AcOH + H^+ \underset{k_{-1}}{\overset{k_1}{\rightleftharpoons}} AcOH \cdot H^+ \tag{2.8}$$

$$EtOH + H^+ \underset{k_{-2}}{\overset{k_2}{\rightleftharpoons}} EtOH \cdot H^+ \tag{2.9}$$

$$EtOH + EtOH \cdot H^+ \underset{k_{-3}}{\overset{k_3}{\rightleftharpoons}} (EtOH)_2 \cdot H^+ \tag{2.10}$$

$$EtOH + AcOH \cdot H^+ \underset{k_{-4}}{\overset{k_4}{\rightleftharpoons}} AcOH / EtOH \cdot H^+ \tag{2.11}$$

$$AcOH + EtOH \cdot H^+ \underset{k_{-5}}{\overset{k_5}{\rightleftharpoons}} AcOH / EtOH \cdot H^+ \tag{2.12}$$

Formation of an acetyl through activation of an adsorbed AcOH molecule is expressed in equation 2.13 where CH_3CO^+ represents the adsorbed acetyl and H_2O represents the released water molecule.

$$AcOH \cdot H^+ \underset{k_{-6}}{\overset{k_6}{\rightleftharpoons}} CH_3CO^+ + H_2O \tag{2.13}$$

The adsorbed acetyl can react with an ethanol molecule, with forward and reverse rate constants k_+ and k_- respectively, from the bulk in the rate-determining step expressed in equation 2.14 where $EA{\cdot}H^+$ represents an absorbed ethyl acetate molecule.

$$CH_3CO^+ + EtOH \underset{k_-}{\overset{k_+}{\rightleftharpoons}} EA \cdot H^+ \tag{2.14}$$

The adsorbed EA molecule can desorb as expressed in equation 2.15.

$$EA \cdot H^+ \underset{k_{-7}}{\overset{k_7}{\rightleftharpoons}} EA + H^+ \tag{2.15}$$

The reaction rate can be expressed as equation 2.16 where $[CH_3CO^+]$ is the number of acetyls on the surface and $[EA{\cdot}H^+]$ is the number of ethyl acetate molecules on the surface.

$$r = k_{+}[CH_3CO^{+}][EtOH] - k_{-}[EA \cdot H^{+}] \tag{2.16}$$

The balance of surface species on the zeolite can be expressed as equation 2.17 where $[H_0]$ is the number of initially accessible Brønsted acid sites, $[H^+]$ is the number of accessible Brønsted acid sites, and $[AcOH \cdot H^+]$, $[EtOH \cdot H^+]$, $[(EtOH)_2 \cdot H^+]$, and $[AcOH/EtOH \cdot H^+]$ reperesent the number of acetic acid monomers, ethanol monomers, ethanol dimers, and acetic acid/ethanol dimers absorbed on the zeolite surface, respectively.

$$[H_0] = [H^+] + [CH_3CO^+] + [EtOH \cdot H^+] + [AcOH \cdot H^+] + [(EtOH)_2 \cdot H^+] + [AcOH / EtOH \cdot H^+] + [EA \cdot H^+] \tag{2.17}$$

The quasi-equilibrium assumption is applied for steps 1-7 involving AcOH monomer, EtOH monomer, EtOH dimer, AcOH/EtOH co-adsorbed dimer, acetyl, and EA monomer formation with equilibrium constants K_1, K_2, K_3, K_4, K_5, K_6, and K_7 respectively. Therefore, the number of AcOH and EtOH monomers, EtOH and AcOH/EtOH dimers, acetyls, and EA monomers can be expressed in terms of gas phase acetic acid, ethanol, ethyl acetate, and water concentrations as shown in equations2.18 –2.23 where $[AcOH]$ represents acetic acid, $[EtOH]$ represents ethanol, $[EA]$ represents ethyl acetate, and $[H_2O]$ represents water pressure in the gas phase.

$$[AcOH \cdot H^+] = K_1[AcOH][H^+] \tag{2.18}$$

$$[EtOH \cdot H^+] = K_2[EtOH][H^+] \tag{2.19}$$

$$[(EtOH)_2 \cdot H^+] = K_3[EtOH \cdot H^+][EtOH] = K_2K_3[EtOH]^2[H^+] \tag{2.20}$$

$$[AcOH / EtOH \cdot H^+] = K_4[AcOH \cdot H^+][EtOH] = K_5[EtOH \cdot H^+][AcOH] = K_1K_4[AcOH][EtOH][H^+] = K_2K_5[AcOH][EtOH][H^+] \tag{2.21}$$

$$[CH_3CO^+] = \frac{K_6[AcOH \cdot H^+]}{[H_2O]} = \frac{K_1K_6[AcOH][H^+]}{[H_2O]} \tag{2.22}$$

$$[EA \cdot H^+] = \frac{[EA][H^+]}{K_7} \tag{2.23}$$

Substituting equations 2.18-2.23 into equation 2.17, we can represent each surface species as a product of equilibrium constants and gas phase concentration, as expressed in equation 2.24.

$$[H_0]=[H^+]+\frac{K_1K_6[AcOH][H^+]}{[H_2O]}+K_2[EtOH][H^+]+K_2K_3[EtOH]^2[H^+]+ K_1[AcOH][H^+]+K_2K_5[AcOH][EtOH][H^+]+\frac{[EA][H^+]}{K_7} \quad (2.24)$$

Rearranging equation2.24, we can express the number of accessible Brønsted acid sites, *[H⁺]*, as a function of the initially accessible Brønsted acid sites, *[H₀]*, and gas phase concentrations, as expressed in equation2.25.

$$[H^+]=\frac{[H_0]}{1+\frac{K_1K_6[AcOH]}{[H_2O]}+K_2[EtOH]+K_2K_3[EtOH]^2+K_1[AcOH]+K_2K_5[AcOH][EtOH]+\frac{[EA]}{K_7}} \quad (2.25)$$

Substituting equations 2.22 and 2.23 into equation 2.16, we can represent the rate as a function of accessible Brønsted acid sites and gas phase concentrations, expressed in equation 2.26.

$$r=\frac{k_+K_1K_6[AcOH][EtOH][H^+]}{[H_2O]}-k_-\frac{[EA][H^+]}{K_7} \quad (2.26)$$

Substituting equation 2.25 into 2.26 and rearranging, we can represent the rate per initially accessible Brønsted acid sites as a function of gas phase concentrations of all reactants and products, expressed in equation 2.27.

$$\frac{r}{[H_0]}=\frac{\frac{k_+K_1K_6[AcOH][EtOH]}{[H_2O]}-k_-\frac{[EA]}{K_7}}{1+\frac{K_1K_6[AcOH]}{[H_2O]}+K_2[EtOH]+K_2K_3[EtOH]^2+K_1[AcOH]+K_2K_5[AcOH][EtOH]+\frac{[EA]}{K_7}} \quad (2.27)$$

Neglecting the effect of EA pressure, as discussed in Section 3.1 of the manuscript, leads to equation 2.28 which represents the rate per active site for EA synthesis via the acetyl mechanism with product formation as the rate-determining step.

$$\frac{r}{[H_0]}=\frac{\frac{k_+K_1K_6[AcOH][EtOH]}{[H_2O]}}{1+\frac{K_1K_6[AcOH]}{[H_2O]}+K_2[EtOH]+K_2K_3[EtOH]^2+K_1[AcOH]+K_2K_5[AcOH][EtOH]} \quad (2.28)$$

2.5.4.2 EA synthesis via the acetyl mechanism (Figure 2.6) and AcOH activation as the rate-determining step

Derivation of this rate equation will use the same equations in S.3.1 but now the rate of reaction is dependent of the activation of AcOH on the zeolite surface, as expressed in equation 2.29.

$$AcOH \cdot H^+ \underset{k_-}{\overset{k_+}{\rightleftharpoons}} CH_3CO^+ + H_2O \tag{2.29}$$

The rate of EA synthesis can then be express as equation 2.30.

$$r = k_+[AcOH \cdot H^+] - k_-[CH_3CO^+][H_2O] \tag{2.30}$$

Assuming EA formation to be quasi-equilibrated, equation 2.14, and substituting in equation 2.23, we can represent the number of acetyls on the surface as a function of gas phase concentrations of reactants and products and of the number of accessible Brønsted acid sites, as expressed in equation 2.31.

$$[CH_3CO^+] = \frac{[EA \cdot H^+]}{K_6[EtOH]} = \frac{[EA][H^+]}{K_6K_7[EtOH]} \tag{2.31}$$

Substituting equations 2.18 and 2.31 into equation 2.29, we can represent the rate as a function of accessible Brønsted acid sites and gas phase concentrations, expressed in equation 2.32.

$$r = k_+K_1[AcOH][H^+] - \frac{k_-[EA][H_2O][H^+]}{K_6K_7[EtOH]} \tag{2.32}$$

The number of initially accessible Brønsted acid sites, $[H_0]$, can be represented as before but now including equation 2.31, as expressed in equation 2.33.

$$\begin{aligned}[H_0] = [H^+] + \frac{[EA][H^+]}{K_6K_7[EtOH]} + K_2[EtOH][H^+] + K_1[AcOH][H^+] + \\ K_2K_3[EtOH]^2[H^+] + K_2K_5[AcOH][EtOH][H^+] + \frac{[EA][H^+]}{K_7}\end{aligned} \tag{2.33}$$

Rearranging equation 2.33, we can express the number of accessible Brønsted acid sites, *[H⁺]*, as a function of the initially accessible Brønsted acid sites, *[H₀]*, and gas phase concentrations, as expressed in equation 2.34.

$$[H^+] = \frac{[H_0]}{1 + \frac{[EA]}{K_6 K_7 [EtOH]} + K_2[EtOH] + K_1[AcOH] + K_2 K_3 [EtOH]^2 + K_2 K_5 [AcOH][EtOH] + \frac{[EA]}{K_7}} \quad (2.34)$$

Substituting equation 2.34 into 2.32 and rearranging, we can represent the rate per initially accessible Brønsted acid sites as a function of gas phase concentrations of all reactants and products, expressed in equation 2.35.

$$\frac{r}{[H_0]} = \frac{k_+ K_1 [AcOH] - \frac{k_- [EA][H_2O]}{K_6 K_7 [EtOH]}}{1 + \frac{[EA]}{K_6 K_7 [EtOH]} + K_2[EtOH] + K_1[AcOH] + K_2 K_3 [EtOH]^2 + K_2 K_5 [AcOH][EtOH] + \frac{[EA]}{K_7}} \quad (2.35)$$

Neglecting the effect of EA pressure leads to equation 2.36 which represents the rate per active site for EA synthesis via the acetyl mechanism with AcOH activation as the rate-determining step.

$$\frac{r}{[H_0]} = \frac{k_+ K_1 [AcOH]}{1 + \frac{[EA]}{K_6 K_7 [EtOH]} + K_2[EtOH] + K_1[AcOH] + K_2 K_3 [EtOH]^2 + K_1 K_4 [AcOH][EtOH]} \quad (2.36)$$

Rate expressions corresponding to different species dominating on the surface, were derived from equation 2.36 by setting the contributions from all other species to zero, as expressed in equations 2.37 – 2.48. The symbol $\Theta_{species}$ is used to represent the dominating surface species designated.

$$\Theta_{empty} : r = k_+ K_1 [AcOH] \quad (2.37)$$

$$\Theta_{acetyls} : r = \frac{k_+ K_1 K_6 K_7 [EtOH][AcOH]}{[EA]} \quad (2.38)$$

$$\Theta_{EtOH} : r = \frac{k_+ K_1 [AcOH]}{K_2 [EtOH]} \quad (2.39)$$

$$\Theta_{EtOH\,\mathrm{dimers}} : r = \frac{k_+ K_1 [AcOH]}{K_2 K_3 [EtOH]^2} \quad (2.40)$$

$$\Theta_{AcOH} : r = k_+ \tag{2.41}$$

$$\Theta_{AcOH/EtOH} : r = \frac{k_+}{K_4[EtOH]} \tag{2.42}$$

$$\Theta_{EtOH} + \Theta_{EtOH\,dimers} : r = \frac{k_+ K_1[AcOH]}{K_2[EtOH](1+K_3[EtOH])} \tag{2.43}$$

$$\Theta_{EtOH} + \Theta_{AcOH/EtOH} : r = \frac{k_+ K_1[AcOH]}{(K_2 + K_1 K_4[AcOH])[EtOH]} \tag{2.44}$$

$$\Theta_{AcOH} + \Theta_{AcOH/EtOH} : r = \frac{k_+}{1+K_4[EtOH]} \tag{2.45}$$

$$\Theta_{EtOH} + \Theta_{AcOH} : r = \frac{k_+ K_1[AcOH]}{K_2[EtOH]+K_1[AcOH]} \tag{2.46}$$

$$\Theta_{EtOH\,dimers} + \Theta_{AcOH/EtOH} : r = \frac{k_+ K_1[AcOH]}{(K_2K_3[EtOH]+K_1K_4[AcOH])[EtOH]} \tag{2.47}$$

$$\Theta_{EtOH\,dimers} + \Theta_{AcOH} : r = \frac{k_+ K_1[AcOH]}{K_1[AcOH]+K_2K_3[EtOH]^2} \tag{2.48}$$

2.5.4.3 EA synthesis via the co-adsorption mediated mechanism (Figure 2.7) and product formation as the rate-determining step

Derivation of this rate equation will use the same equations in S.3.1 but now the rate of reaction is dependent of the activation of the AcOH/EtOH co-adsorbed complex on the zeolite surface, as expressed in equation 2.49.

$$AcOH/EtOH \cdot H^+ \underset{k_-}{\overset{k_+}{\rightleftharpoons}} H^+ + EA + H_2O \tag{2.49}$$

The rate of EA synthesis can then be express as equation 2.50.

$$r = k_+[AcOH/EtOH \cdot H^+] \tag{2.50}$$

Substituting equation 2.21 into 2.50, we can represent the rate as a function of accessible Brønsted acid sites and gas phase concentrations, expressed in equation 2.51.

$$r = k_+ K_1 K_4[AcOH][EtOH][H^+] = k_+ K_2 K_5[AcOH][EtOH][H^+] \tag{2.51}$$

The number of initially accessible Brønsted acid sites, *[H₀]*, can be represented as a function of the number of accessible Brønsted acid sites, *[H⁺]* and gas phase concentrations, expressed in equation 2.52.

$$[H_0] = [H^+] + K_2[EtOH][H^+] + K_1[AcOH][H^+] + K_2K_3[EtOH]^2[H^+] + K_2K_5[AcOH][EtOH][H^+] \quad (2.52)$$

Rearranging equation 2.52, we can express the number of accessible Brønsted acid sites, *[H⁺]*, as a function of the initially accessible Brønsted acid sites, *[H₀]*, and gas phase concentrations, as expressed in equation 2.53.

$$[H^+] = \frac{[H_0]}{1 + K_2[EtOH] + K_1[AcOH] + K_2K_3[EtOH]^2 + K_2K_5[AcOH][EtOH]} \quad (2.53)$$

Substituting equation 2.53 into 2.51 and rearranging, we can represent the rate per initially accessible Brønsted acid sites as a function of gas phase concentrations of all reactants and products, expressed in equation 2.54.

$$\frac{r}{[H_0]} = \frac{k_+K_2K_5[AcOH][EtOH]}{1 + K_2[EtOH] + K_1[AcOH] + K_2K_3[EtOH]^2 + K_2K_5[AcOH][EtOH]} \quad (2.54)$$

Rate expressions corresponding to different species dominating on the surface, were derived from equation 2.54 by setting the contributions from all other species to zero, as expressed in equations 2.55 – 2.65. The symbol $\Theta_{species}$ is used to represent the dominating surface species designated.

$$\Theta_{empty} : r = k_+K_2K_5[AcOH][EtOH] \quad (2.55)$$

$$\Theta_{EtOH} : r = k_+K_5[AcOH] \quad (2.56)$$

$$\Theta_{EtOH\,dimers} : r = \frac{k_+K_5[AcOH]}{K_3[EtOH]} \quad (2.57)$$

$$\Theta_{AcOH} : r = \frac{k_+K_2K_5[EtOH]}{K_1} \quad (2.58)$$

$$\Theta_{AcOH/EtOH} : r = k_+ \quad (2.59)$$

$$\Theta_{EtOH} + \Theta_{EtOH\,dimers} : r = \frac{k_+K_4[AcOH]}{(1 + K_3[EtOH])} \quad (2.60)$$

$$\Theta_{EtOH} + \Theta_{AcOH/EtOH} : r = \frac{k_+K_5[AcOH]}{1 + K_5[AcOH]} \quad (2.61)$$

$$\Theta_{AcOH} + \Theta_{AcOH/EtOH} : r = \frac{k_+ K_2 K_5 [EtOH]}{K_1 + K_2 K_5 [EtOH]} \tag{2.62}$$

$$\Theta_{EtOH} + \Theta_{AcOH} : r = \frac{k_+ K_2 K_5 [AcOH][EtOH]}{K_2 [EtOH] + K_1 [AcOH]} \tag{2.63}$$

$$\Theta_{EtOH\,dimers} + \Theta_{AcOH/EtOH} : r = \frac{k_+ K_5 [AcOH]}{K_3 [EtOH] + K_5 [AcOH]} \tag{2.64}$$

$$\Theta_{EtOH\,dimers} + \Theta_{AcOH} : r = \frac{k_+ K_2 K_5 [AcOH][EtOH]}{K_1 [AcOH] + K_2 K_3 [EtOH]^2} \tag{2.65}$$

Equations 2.64 and 2.65 are rearranged to represent the reciprocal rate as a function of gas phase AcOH and EtOH concentration, as expressed in equations 2.66 and 2.67 respectively.

$$\frac{1}{r} = \frac{K_3 [EtOH]}{k_+ K_5 [AcOH]} + \frac{1}{k_+} \tag{2.66}$$

$$\frac{1}{r} = \frac{K_3 [EtOH]}{k_+ K_5 [AcOH]} + \frac{K_1}{k_+ K_2 K_5 [EtOH]} \tag{2.67}$$

2.5.5 Effect of water co-feed on the rate of EA formation

Esterification reactions were conducted with and without H_2O co-feed (0.04 kPa) over H-BEA, H-FER, H-MFI, and H-MOR at P_{EtOH} = 10.2, P_{AcOH} = 1.0-5.0, and T = 363 K. The ethyl acetate synthesis rate as a function of AcOH pressure is shown in Figure 2.18.

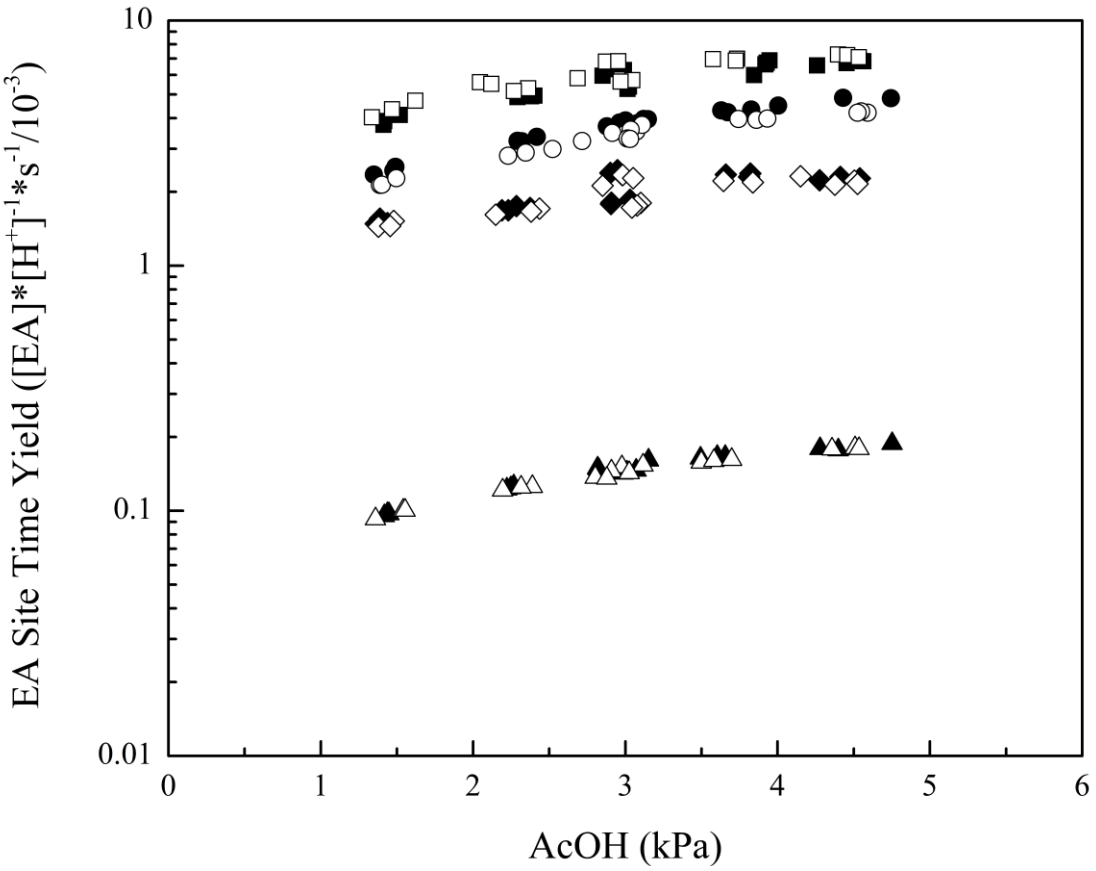

Figure 2.18 Measured ethyl acetate (EA) synthesis rate as a function of acetic acid (P_{EtOH} =10.2 kPa, T = 363 K) over H-BEA (2.7 mg, Si/Al = 12.0, ■), H-FER (100 mg, Si/Al = 11.5, ▲) H-MFI (3 mg, Si/Al = 13.2, ●), and H-MOR (9 mg, Si/Al = 11.1, ♦). Closed symbols represent data with no H_2O co-feed and open symbols represent data with P_{H2O} = 0.04 kPa.

2.5.6 Parameter estimation using non-linear techniques

2.5.6.1 Parameter estimation using a weighted least squares technique

Kinetic parameters (k_+ and K_5/K_3) and their uncertainties were estimated using a non-linear least squares technique described by Harris [75]. EtOH and AcOH pressure along with observed rates were placed in separate columns in Microsoft Excel. A calculated rate was determined using Equation 2.68. Squared relative residuals (SRR) were calculated with Equation 2.69. The sum of the SRR was then calculated. This sum was then minimized by changing k_+ and K_5/K_3 using the Solver function. Uncertainties in k_+ and K_5/K_3 were determined using the

$$r = \frac{k_+ \frac{K_5}{K_3}[AcOH]}{[EtOH] + \frac{K_5}{K_3}[AcOH]} \tag{2.68}$$

$$SRR = \frac{(r - r_{calc})^2}{r^2} \tag{2.69}$$

"jackknife" procedure as explained next. SRR of data points at similar reactant partial pressures, usually triplicate GC injections, were deleted and the sum of residuals was minimized. The resultant values of k_+ and K_5/K_3 were copied and pasted into separate columns and the previously deleted SRR were recalculated. This process was then repeated with all of the SRR of similar reactant pressure data points. Standard deviations (σ) of the resultant k_+ and K_5/K_3 were calculated and the standard error was determined with Equation 2.70 where n is the number of data points. These standard errors are the estimates of uncertainty in the least squares determined k_+

$$\text{Standard error} = \sigma * \frac{n-1}{\sqrt{n}} \tag{2.70}$$

and K_5/K_3. This procedure was then completed for each zeolite, temperature, and reactant pressure varying experiment. Least squares determined k_+ and K_5/K_3 were compiled with their specific uncertainties for each temperature and zeolite. The natural log of kinetic parameters (k_+ and K_5/K_3) and their propagated uncertainties at T = 353 K are presented in Table 2.5 of the main article.

Activation energies, E_{act}, and their uncertainties for reactions over each zeolite were estimated using a similar non-linear least squares technique. k_+, as calculated from reciprocal plots (Figures 2.8-2.11), were placed in columns in Microsoft Excel with their respective errors (δ_i) obtained with use of the LINEST function and Equation 2.71 where b is the y-intercept of the regressed linear fit. For example, by looking at Equation 2.6 of the main article, we find that b is equal to $1/k_+$. Natural logs of k_+ were calculated and their respective errors propagated. Weight

$$\delta_{k_+} = \frac{\delta_b}{b^2} \tag{2.71}$$

factors were determined for all data using Equation 2.72. Calculated $ln(k_+)$ were determined with Equation 2.73 and squared relative residuals (SRR) using Equation 2.74 with T the temperature, R the gas constant, and A_{k+} the pre-exponential constant. The sum of the SRR was then calculated. This sum was minimized by changing E_{act}/R and $ln(A_{k+})$ using the Solver function.

$$w_i = \frac{1}{\delta_i^2} \tag{2.72}$$

$$\ln(k_+)_{calc} = \frac{-E_{act}}{R} \cdot \frac{1}{T} + \ln(A_{k_+}) \tag{2.73}$$

$$SRR = \frac{(\ln(k_+) - \ln(k_+)_{calc})^2}{\ln(k_+)^2} \tag{2.74}$$

Uncertainties in $ln(k_+)$ were determined using the "jackknife" procedure as explained next. SRR of data points at similar reactant temperature, one each for AcOH and EtOH pressure varying experiments, were deleted and the sum of residuals was minimized. The resultant values of E_{act}/R and $ln(A_{k+})$ were copied and pasted into separate columns and the previously deleted SRR were recalculated. This process was then repeated with all of the SRR of similar reactant temperature data points. Standard deviations (σ) of the resultant E_{act}/R and $ln(A_{k+})$ were calculated and the standard error was determined with Equation 2.70. These standard errors are the estimates of uncertainty in the least squares determined E_{act}/R and $ln(A_{k+})$. This procedure was then completed for each zeolite and temperature. The activation energies and their uncertainties for each zeolite are presented in Table 2.5 of the main article.

2.5.6.2 Parameter estimation using a pure algebraic equation

Activation energies and kinetic parameters (k_+ and K_5/K_3), along with their uncertainties, were determined with use of Athena Visual Studio (v14.2, W. E. Stewart and M. Caracotsios). The software uses a Bayesian estimation technique to optimize kinetic parameters and activation energies using a model, Equation 4 of the main article, which includes experimental EtOH and AcOH pressure as well as temperature and observed rate. E_{act}, k_+, and K_5/K_3, were optimized for each zeolite using all of their respective experimental data points (Figures 2.1-2.4 of the main article). Uncertainties were given as 95% marginal highest probability density (HPD) intervals. Activation energies and kinetic parameters along with their uncertainties are presented in Table 2.5 of the main article.

CHAPTER

THREE

CH_4 DEHYDROAROMATIZATION ON Mo/H-ZSM-5: EFFECTS OF CO-PROCESSING H_2 AND CH_3COOH*

3.1 Introduction

Natural gas has been purported to be a feedstock for the production of commodity chemicals and fuels currently produced from crude oil [80,81]. Methane, the primary component of natural gas, is chemically inert and its conversion to higher hydrocarbons involves the creation of C-C bonds and H_2 elimination [80,81]. A representative pathway for the non-oxidative conversion of methane is dehydroaromatization (DHA) via high temperature pyrolysis over catalytic surfaces.

Wang et al. originally reported that H-ZSM-5 modified by aqueous molybdenum oxide leads to near-equilibrium concentrations of aromatics and ethylene during non-oxidative CH_4 reactions at 973 K [50]. Further investigations of CH_4 DHA reactions on Mo encapsulated ZSM-5 catalysts at temperatures ~950 K have reported 8-10% CH_4 conversion with greater than 70% selectivity to benzene and stable catalytic performance at extended reactions times (16 hours) [51,54,82–89]. Substitution of high-valent metal-oxo species from aqueous solutions into cation exchange sites is limited due to the large size and multiple charge of solvated polyanion clusters, which impair diffusion within zeolite channels at pH levels required for stable aluminosilicate frameworks [55,90,91]. Borry et al. developed a vapor phase exchange process that can be used to

*Reported from Bedard, J. W., Hong, D.-Y., and Bhan, A., *Journal of Catalysis*, **306**, 58-67, (2013) with permission from Elsevier Inc. © 2013

support Mo oxides (MoO_x) in zeolites to combat this issue [88]. Kim et al reported a 1:1 Mo/Al stoichiometry corresponding to ion-exchange with Brønsted acid sites using vapor phase exchange [87]. Hexa-valent Mo forms dimeric $(Mo_2O_5)^+$ species upon vapor phase ion-exchange with two neighboring Al centers as evidenced by the incomplete exchange of Mo on all Al sites and the presence of residual protons as well as characteristic Raman and X-ray absorptions in these samples [87,88,92]. Upon exposure to CH_4 at 973 K, an induction period is observed in which MoO_x is carburized to form carbidic Mo (MoC_x) with oxygen removed as CO, CO_2, and H_2O as reported by Iglesia et al. and Bao et al. [58,87,93]. Ding et al. reported that $Mo_2O_5^+$ dimers reduce during carburization to form small (0.6-1 nm) MoC_x clusters, similar to the channel diameter within ZSM-5 (0.55 x 0.57 nm), with a fraction of the acidic OH groups, initially exchanged with MoO_x dimers, being regenerated [57]. These small MoC_x clusters contain ~10 Mo atoms and are shown to be stable and to resist sintering or migration to external surfaces during high temperature (~950 K) CH_4 reactions for several hours [57]. The presence and catalytic involvement in the activation of C-H bonds of these MoC_x clusters has been evidenced by X-ray absorption, X-ray photoelectron, infrared, and NMR spectroscopic investigations [57,94–96].

Mo-ZSM-5 catalysts have been shown to deactivate during non-oxidative CH_4 DHA reactions due to deposition of carbonaceous species [84,97]. Ichikawa et al. reported that a co-feed of CO_2 with CH_4 led to improved stability of the Mo-ZSM-5 catalysts at extended times on stream and postulated that this enhanced stability was due to CO_2 reacting with deactivating carbon species by the reverse Boudouard reaction [98,99]. Liu et al. studied the effects of co-feeding CO_2, CO, and H_2 with CH_4 and reported a drastic cessation of catalytic activity at higher CO_2 pressures ($CO_2/CH_4 > 0.075$) due to oxidation of the active MoC_x species [60]. CO co-feed (CH_4/CO ratio) had no effect on the rate and selectivity of CH_4 DHA reactions. Liu concluded that the presence CO was not responsible for the decrease in reaction rates during CO_2 co-feeding experiments. H_2 co-feed (CH_4/H_2 ratio) led to decreased hydrocarbon formation rates attributed to the reversibility of CH_4 pyrolysis reactions [60].

Methane DHA to benzene at 950 K is equilibrium limited to ~10% conversion with MoC_x clusters activating C-H bonds to remove H-atoms as H_2 and acid sites providing centers for carbon chain growth. Yu et al. postulated that hydrogen removal is the limiting factor in light alkane dehydrogenation reactions on proton and metal modified ZSM-5 formulations [100] and that this H-desorption bottleneck results in a very high chemical potential of hydrogen on

the surface of the catalyst. Iglesia and co-workers have exploited this phenomenon by using propane as the hydrogen source in hydrodesulfurization reactions over Zn-ZSM-5 catalysts [101–104].

Here, we seek to extend this concept of heteroatom removal reactions by using methane in deoxygenation reactions of low molecular weight oxygenates using MoC_x/ZSM-5 formulations. Co-processing CH_4 with acetic acid using Mo/H-ZSM-5 catalysts results in a stratified reactor bed with a fraction of the bed upstream being oxidized by acetic acid to form CO/H_2 mixtures in reforming reactions of CH_4 and the remaining fraction downstream accomplishing CH_4 DHA reactions in presence of the H_2 and CO produced upstream. Forward rates for CH_4 DHA are invariant with respect to catalyst loading and H_2 pressure in presence of hydrogen and acetic acid co-feeds. This research highlights a critical limitation in attempting to couple deoxygenation and dehydrogenation chemistries on Mo/ZSM-5 formulations by co-processing oxygenates and CH_4 – the preferential selectivity to remove oxygen as CO instead of as H_2O.

3.2 Materials and methods

3.2.1 Catalyst preparation

A ZSM-5 (Si/Al = 11.7, CBV 2314) zeolite sample was obtained from Zeolyst International in its ammonium form. The silicon to aluminum ratio was determined by elemental analysis (Analytical Geochemistry Lab, University of Minnesota). NH_4-ZSM-5 was converted to H-ZSM-5 by treating in dry air (0.67 $cm^3\ s^{-1}$ at NTP conditions, UHP, Minneapolis Oxygen) to thermally decompose NH_4^+ to H^+ and $NH_{3(g)}$ by increasing the temperature from ambient to 773 K at 0.0167 K s^{-1} and holding at 773 K for 10 hours. H-ZSM-5 and MoO_3 powders (Sigma-Aldrich, 99.9%) were ground together in an agate mortar and pestle for 0.5 hours to form intimate mixtures containing a Mo to Al_f ratio of 0.25. The mixture was heated from ambient to 623 K at 0.0167 K s^{-1} and soaked at this temperature for 16 hours in dry air (0.67 $cm^3\ s^{-1}$) to remove water and to disperse MoO_3 on the zeolite's external surface [88,92]. Subsequently, the mixture was heated to 973 K at 0.167 K s^{-1} and soaked at this temperature for 10 hours to facilitate molybdenum oxide migration into the zeolite pores [92]. After treatment, the molybdenum to aluminum ratio was determined by elemental analysis (Analytical Geochemistry Lab, University of Minnesota). The catalysts were pressed to form pellets which were then crushed and sieved to attain

particle sizes between 180 and 425 μm (40-80 mesh) for subsequent use in catalytic reactions.

3.2.2 Catalytic reactions of CH_4 dehydroaromatization

CH_4 dehydroaromatization reactions were conducted with 0.1-1.0 g of catalyst in a fixed bed, tubular quartz reactor (10 mm inner diameter) at atmospheric pressure and 950 K. The catalyst bed was made stationary by a porous quartz frit. Prior to conducting DHA reactions, catalyst samples were pretreated, to remove water, in Ar (0.21 $cm^3\ s^{-1}$, UHP, Minneapolis Oxygen) by increasing the temperature from ambient to 950 K at 0.167 K s^{-1}. Reactor temperature was set by a split tube furnace (Applied Test System, Series 3210) controlled by an Omega temperature controller (CN7823) with K-type thermocouple feedback (Omega Engineering). A feed gas mixture of CH_4/Ar (90% CH_4 and 10% Ar, 0.21 $cm^3\ s^{-1}$ corresponding to CH_4 space velocity of 684 $cm^3\ g_{cat}^{-1}\ h^{-1}$, UHP, Matheson Tri-Gas) was introduced to the reactor with Ar serving as the internal standard. Liquid acetic acid (AA) ($1.52 \times 10^{-7} - 4.57 \times 10^{-7}$ mol s^{-1}, Fluka, >99.8%) was introduced to flowing gas streams using a liquid infusion pump (Model 100, KD Scientific) and vaporized at 473 K in heated transfer lines. Transfer lines were kept at 473 K to ensure that no condensation of liquid reactants or products occurred. AA or H_2 ($5.83 \times 10^{-3} - 2.20 \times 10^{-2}$ $cm^3\ s^{-1}$, UHP, Minneapolis Oxygen) were co-fed with CH_4 once the catalyst was fully carburized and the benzene formation rate reached steady-state, typically after 0.3 to 3.0 hours depending on the catalyst loading. He ($1.00 \times 10^{-2} - 2.20 \times 10^{-2}$ $cm^3\ s^{-1}$, UHP, Minneapolis Oxygen) was introduced to the inlet gas feed as an inert for constant CH_4 partial pressure experiments. The reactor effluent was sent via heated transfer lines to a gas chromatograph (GC) (Agilent 7890) equipped with two capillary columns: a bonded polystyrene-divinylbenzene column (HP-PLOT/Q, 30.0 m x 0.32 mm x 0.5 μm, Agilent) connected to a thermal conductivity detector to separate and analyze permanent gases and a (5%-phenyl)-methylpolysiloxane column (HP-5, 30.0 m x 0.32 mm x 0.5 μm, Agilent) connected to a flame ionization detector to separate and analyze hydrocarbons. Ar, serving as the internal standard, was used to calculate CH_4 conversion as well as product formation rates and selectivity. Product selectivity was calculated on a carbon atom basis considering all carbon-containing products with Equation 3.1 and i as a carbon-containing species, n the number of carbon atoms in species i, and F the molar flow rate. Transient product evolution throughout the course of the reaction was measured with an on-line mass spectrometer (MS) (MKS Cirrus 200 Quadrupole MS system) connected to the outlet of the GC. The number of

removed O-atoms during carburization of molybdenum oxide was determined by the cumulative amount of H_2O, CO, and CO_2 as calculated from the transient MS signal. Product formation rates (mol [product] (g-atom Mo $s)^{-1}$) are reported as measured net rates or forward rates, as discussed in Section 3.3.

$$\%S_i = \frac{n_i * F_i}{\sum_i n_i * F_i} \tag{3.1}$$

3.2.3 Chemical titration of Brønsted acid sites using dimethyl ether

Chemical titration using dimethyl ether (DME) was performed to determine the number of free Brønsted acid sites on H-ZSM-5 and MoO_x/H-ZSM-5 at various degrees of carburization [77]. The number of accessible acid sites during DHA reactions was investigated by titrating MoC_x/H-ZSM-5 samples at different carburization times (0.1-3.0 hours). The samples (0.1 g) were treated in He (0.33 cm^3 s^{-1}, UHP, Minneapolis Oxygen) by increasing the temperature from ambient to 773 K at 0.167 K s^{-1}, soaking for 1 hour, and subsequently cooling the sample to 423 K in He flow. A mixture of 50% DME / 1% CH_4 / 49% Ar (UHP, Praxair) was introduced (0.25 cm^3 per pulse) to the catalyst sample by He (0.67 cm^3 s^{-1}) in pulses at 90 s intervals until unreacted DME was detected in the effluent by MS. CH_4 was used as an internal standard for measuring DME uptake. Cheung et al. showed that each Brønsted acid site can adsorb 0.5 DME molecules because DME reacts with surface hydroxyl groups to form persistent methyl groups [76].

3.2.4 Mo K-edge X-ray absorption near edge structure spectroscopy

X-ray absorption near edge structure (XANES) spectra of MoO_x, MoC_x, and Mo/ZSM-5 samples were measured with the use of beamline X18B at the Brookhaven National Laboratory. MoO_3 (Sigma-Aldrich, 99.5%), MoO_2 (Sigma-Aldrich, 99.9%), β-Mo_2C (prepared by temperature-programmed reduction of MoO_3 in 20% H_2/CH_4 at 973 K [105]), and $MgMo_2O_7$ (prepared as in [106]) were measured as references of standard oxidation states to determine the oxidation state of unknown samples. β-Mo_2C and MoC_x/H-ZSM-5 samples were sealed with Kapton tape to prevent ambient air exposure in a glove box. Spectra were analyzed with the use of Athena Version 0.8.056 [107]. Pre-edge and post-edge baselines were subtracted with use of first- and third-order polynomials,

respectively, and the normalized near-edge region was analyzed between 19.80 and 21.20 keV after removal of the absorption background.

3.3 Results and discussion

Ethylene, ethane, benzene, toluene, xylenes, and naphthalene, the products of methane dehydroaromatization reactions, were observed on 1 g of Mo/H-ZSM-5 catalysts with $Mo/Al_f = 0.25$ at T = 950 K and 12.0 $cm^3\ s^{-1}$ flow of CH_4 (91.2 kPa) balanced with Ar. Near equilibrium conversion of CH_4 (~10%) was observed after an initial induction period. Below, we present a discussion of the structural characteristics of the Mo/H-ZSM-5 catalyst along with a systematic evaluation of DHA reactions of CH_4, CH_4/H_2, and CH_4/AA mixtures to show that forward rates of benzene formation are unperturbed by addition of H_2 and AA. Measured effects of these co-reactants show that thermodynamic reversibility governs the conversion of CH_4 to benzene at these reaction conditions.

3.3.1 Structural characterization of Mo/H-ZSM-5 catalysts

The products formed during carburization of MoO_x/H-ZSM-5 at 950 K were detected by online mass spectrometric analysis as shown in Figure 3.1. Initial production (0.1 ks) of CO and CO_2 was a result of reduction and carburization of trace amounts of unexchanged MoO_3, also reported by Lacheen et al. [58]. The production of CO_2 reaches a maximum at ~0.4 ks while the formation of CO and H_2 reached a maximum at ~ 0.5 ks, which is concurrent with the formation rates of CO_2 becoming negligible. Production of H_2O also peaked at ~0.4 ks and decreased to a negligible rate at ~0.5 ks. The rate of O* removal gradually decreases as the MoO_x/H-ZSM-5 catalyst is converted to MoC_x/H-ZSM-5 catalyst [51,57]. Exposure of MoO_x/H-ZSM-5 to CH_4 removed 2.3 ± 0.1 O atoms per Mo atom after a carburization period of 10.8 ks as measured from the evolution of oxygen-containing products (CO, CO_2, and H_2O), indicating that most of the non-zeolitic O atoms were removed. An induction period of ~0.7 ks was observed which corresponds to the time needed to remove O atoms prior to formation of aromatics [54]. The ratio of O atoms removed per Mo atom as a function of time is shown in section 3.5 (Figure 3.13). This result is comparable to the theoretical value of 2.5 O atoms per Mo atom corresponding to exchanged $Mo_2O_5^{2+}$ dimers occupying two proximate Al sites and is consistent with results reported by Iglesia and co-workers [59,87]. Bao and co-workers as well as Ledoux and co-workers have observed monomeric MoO_x species in Mo/H-ZSM-5 catalysts

using spectroscopic probes: we cannot exclude the possibility of these structures existing [108–111]. While we cannot distinguish between different Mo species in situ, we have accounted for all the available Mo atoms. All rates, net and forward, presented in this report have been normalized to the total number of Mo atoms, to result in the lowest possible rate. Evolution of C_2H_x (ethane and ethylene) products occurred immediately upon exposure of $Mo_2O_5^{2+}$/H-ZSM-5 to CH_4 and gradually increases to a steady-state formation rate (0.4×10^{-4} mol (g-atom Mo-s)$^{-1}$). Benzene, the primary DHA product, initially evolved at ~ 0.7 ks and monotonically increased to a maximum formation rate (1.7×10^{-4} mol (g-atom Mo-s)$^{-1}$) at ~ 10.8 ks once the conversion of $Mo_2O_5^{2+}$ dimers to MoC_x was complete.

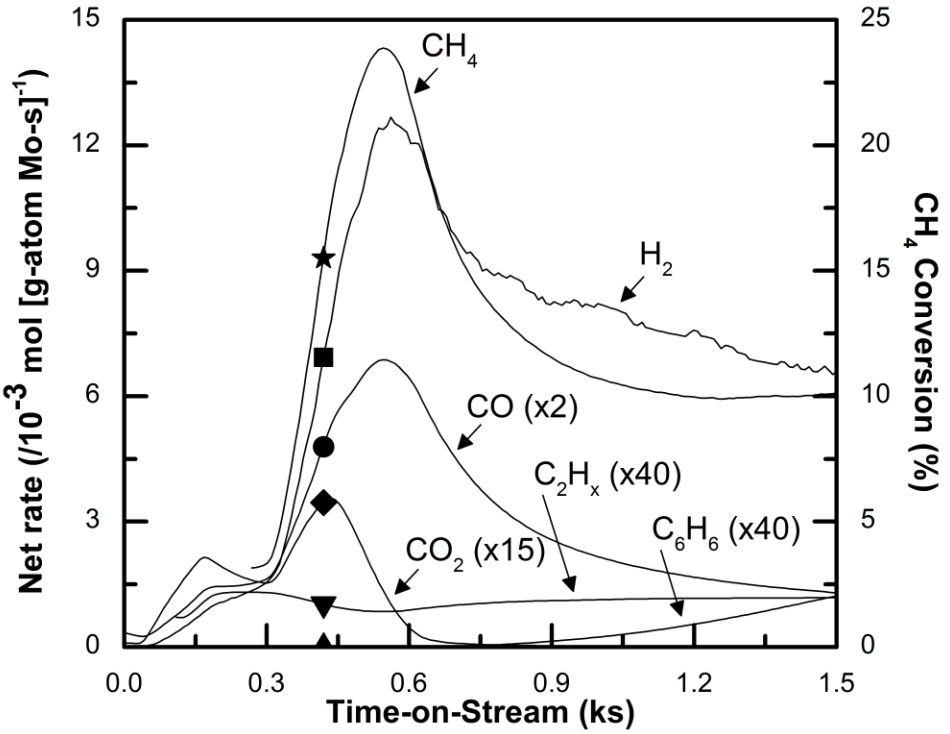

Figure 3.1 Transient H_2 (■), CO (●), CO_2 (◆),C_2H_x (▼), and C_6H_6 (▲) formation rates and CH_4 conversion (★) on 1.0 g of Mo/H-ZSM-5 at T = 950 K, CH_4 flow = 12.0 cm^3 min^{-1}, CH_4/Ar ratio = 9, and Mo/Al$_f$ = 0.25. Symbols are GC data and lines are MS transient data.

Near-edge X-ray absorption spectra for exchanged Mo/H-ZSM-5 catalyst before and after thermal treatment at 950 K in CH_4 are shown in Figure 3.14. Mo compounds with known structure and oxidation states including MoO_3, MoO_2, $MgMo_2O_7$ and β-Mo_2C are also shown for comparison. The spectrum of MoO_x/H -

ZSM-5 (Figure 3.14d) showed a similar pre-edge feature to that observed for $MgMo_2O_7$ (Figure 3.14c), which contains ditetrahedral Mo centers, suggesting the existence of $Mo_2O_5^{2+}$-ZSM-5 structures attached to neighboring exchange sites [92]. The pre-edge absorbance is due to $1s \rightarrow 4d$ electronic transitions which are forbidden in centrosymmetric Mo geometries [112,113]. A comparison of post-edge energy (20 keV) absorbance of MoO_x /H -ZSM-5 to $MgMo_2O_7$ and MoO_3 (Figure 3.14b) indicates that the Mo environment of MoO_x /H -ZSM-5 is similar to the tetrahedral nature of $MgMo_2O_7$ versus the distorted octahedral environment of MoO_3 [59]. This result also supports the presence of $Mo_2O_5^{2+}$ dimers bonded to Al sites. The pre-edge feature of MoO_x /ZSM-5 is not observed after treatment in CH_4 flow to form MoC_x/H-ZSM-5 (Figure 3.14e). The spectrum shown in Figure 3.14e is similar to that of β-Mo_2C (Figure 3.14f) showing that Mo-oxo dimers formed initially upon thermal dispersion of MoO_3 were reduced and carburized to form carbidic species.

The edge energies of the Mo/H-ZSM-5 catalysts and reference samples were determined and are shown in Table 3.4. The edge energy of each compound was taken as the first inflection point, not including the pre-edge feature, in the absorption spectrum. The $Mo_2O_5^{2+}$/H-ZSM-5 sample had an edge energy of 6.3 eV (relative to Mo^0), similar to that of MoO_3 (6.0 eV), corresponding to Mo^{6+}. After exposure to CH_4 at 950 K for 3 hours, the edge energy of the catalyst shifted to 4.0 eV, which was similar to that of β-Mo_2C (3.8 eV). The resulting similarities in edge energy seen in $Mo_2O_5^{2+}$/H -ZSM-5 and MoO_3 as well as MoC_x/H-ZSM-5 and β-Mo_2C is consistent with results reported by Lacheen et al. [59].

Chemical titration using DME was performed to determine the number of free Brønsted acid sites regenerated during reduction and carburization of $Mo_2O_5^{2+}$/H-ZSM-5 catalyst as shown in Table 3.1. The concentration of free Brønsted acid sites in H-ZSM-5 (Si/Al = 13.2) was determined to be 12.9 ± 0.1 x 10^{-4} mol g^{-1}, which is similar to the concentration of Al in the zeolite as calculated from the Si to Al ratio (11.7 x 10^{-4} mol g^{-1}). After thermal treatment of MoO_3/H-ZSM-5 physical mixtures in dry air at 973 K, the concentration of free Brønsted acid sites decreased to 1.9 ± 0.1 x 10^{-4} mol g^{-1} due to exchange of molybdenum oxide on Brønsted acid sites as well as extraction of framework aluminum to form aluminum molybdate and extra-framework Al species [88]. The concentration of free Brønsted acid sites gradually increased with carburization time up to 3.7 ± 0.1 x 10^{-4} mol g^{-1} at ~0.6 ks due to migration of Mo-oxo species in forming MoC_x clusters. The number of protons accessible to DME decreased to 1.9 ± 0.1 x 10^{-4}

mol g^{-1} at ~10.8 ks due to adsorption of aromatics and other organic compounds formed on the regenerated Brønsted acid sites during CH_4 DHA reactions. The increase in the number of regenerated Brønsted acid sites from 0.0 to 0.6 ks is consistent with the production of CO (Figure 3.1) while the decrease in the number of Brønsted acid sites after 600 s is consistent with a concomitant increase in the rate of benzene formation (Figure 3.1). The increase followed by a decrease in the number of free Brønsted acid sites is consistent with a bifunctional CH_4 dehydrocondensation pathway that proceeds through CH_4 dehydrogenation on MoC_x/H-ZSM-5 catalysts to form C_2H_x species followed by dehydroaromatization of C_2H_x species on the regenerated Brønsted acid sites to form aromatics such as benzene and naphthalene, as depicted in Figure 3.2 [54]. This proposed bifunctional mechanism on Mo/ZSM-5 formulations is supported by results reported by Wang et al. who showed that bulk Mo carbide can catalyze conversion of CH_4 to C_2 products, however, does not form aromatics [51]. A similar study by Solymosi et al. showed that unsupported Mo_2C can catalyze dehydrogenation of ethane without formation of aromatics, while MoC_x/H-ZSM-5 catalysts could convert ethane to aromatics [114].

Table 3.1 Regeneration of H^+ and O-atom removal from MoO_x/H-ZSM-5 during carburization. Reaction conditions: Temperature, 950 K; CH_4 flow rate, 12.0 $cm^3\,min^{-1}$; CH_4:Ar = 9:1; catalyst loading, 0.1 g; $Mo/Al_f = 0.25$.

	H-ZSM-5	MoO_x/H-ZSM-5					
Carburization time (ks)	-	0.0	0.3	0.6	0.9	1.2	10.8
No. of Free H^+ (10^{-4} mol g^{-1})	12.9	1.9	2.6	3.7	2.9	2.2	1.9
O $atom_{removed}$/Mo	-	0.0	0.6	1.1	1.3	1.5	2.2

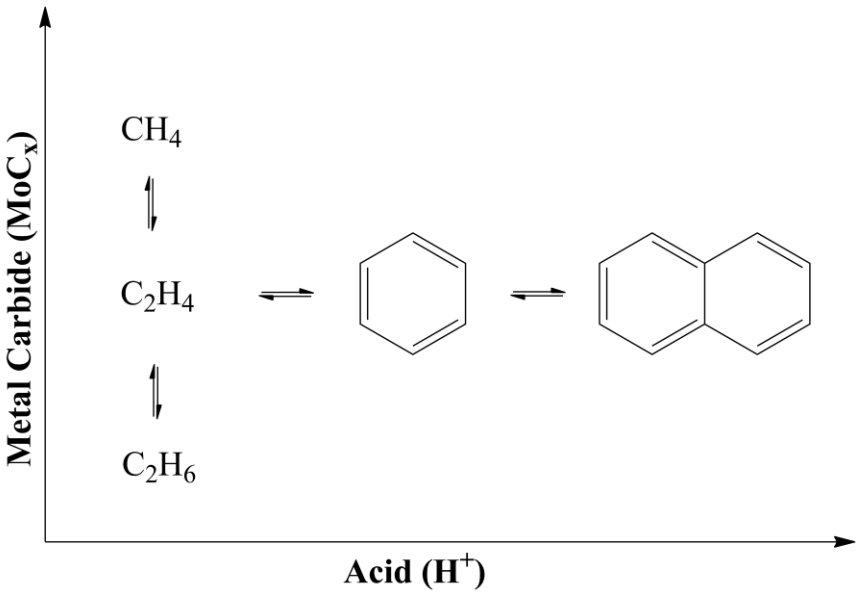

Figure 3.2 Proposed bifunctional pathway of CH_4 dehydroaromatization to aromatics on MoC_x/H-ZSM-5 catalysts.

3.3.2 Steady-state dehydroaromatization of CH_4 over MoC_x/H-ZSM-5 catalysts

Steady-state catalytic rates and selectivities were measured on MoO_x/H-ZSM-5 (Mo/Al_f = 0.25) at 950 K using a CH_4/Ar reactant stream. Net rates of product formation in CH_4 DHA reactions and CH_4 conversion are shown as a function of time in Figure 3.3. Near equilibrium conversion of CH_4 (~8%) was observed after carburization was complete at ~10.8 ks. CH_4 conversion decreased at longer time-on-stream (TOS). Production of C_2H_x was first observed during the induction period then steadily increased with TOS. Formation of benzene and toluene was observed after the induction period with formation rates increasing to 0.17 x 10^{-3} mol (g-atom Mo-s)$^{-1}$ and 0.008 x 10^{-3} mol (g-atom Mo-s)$^{-1}$, respectively, before decreasing monotonically at longer TOS. These formation rates of C_6H_6 are similar to those reported by Hargreaves et al. (0.14 x 10^{-3} mol (g-atom Mo-s)$^{-1}$), Ichikawa et al. (0.29 x 10^{-3} mol (g-atom Mo-s)$^{-1}$), Iglesia et al. (0.45 x 10^{-3} mol (g-atom Mo-s)$^{-1}$), and Solymosi et al. (0.50 x 10^{-3} mol (g-atom Mo-s)$^{-1}$) [59,82,89,115]. Formation of naphthalene followed a similar trend as benzene with formation rates steadily decreasing after reaching a maximum of ~0.05 x 10^{-3} mol (g-atom Mo-s)$^{-1}$. The gradual buildup of coke in the zeolite channels presumably decreased the effective diameter of the zeolite such that formation of bulky naphthalene was inhibited [51,53]. Coke formation is also

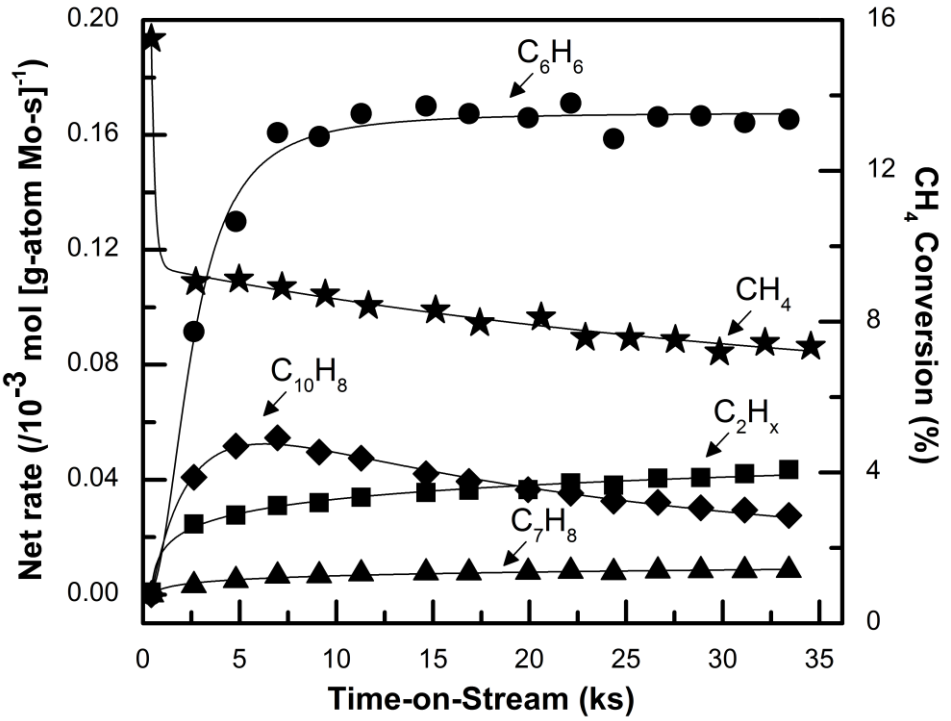

Figure 3.3 Transient C_6H_6 (●), $C_{10}H_8$ (◆), C_2H_x (■), and C_7H_8 (▲) formation rates and CH_4 conversion (★) of Mo/H-ZSM-5 at 950 K, CH_4 flow rate 12.0 cm^3 min^{-1}, CH_4:Ar = 9:1, and catalyst loading 1.0 g with Mo:Al_f = 0.25. Symbols are GC data and lines are fitted curves.

consistent with product selectivity shifting to C_2H_x molecules at longer times on stream as coke deposition deactivated acidic sites in the zeolite. This observation is consistent with the DME titration results shown in Table 3.1 and with reports by Rosynek et al. [51,53].

Table 3.2 shows CH_4 conversion and product selectivities of DHA reactions of CH_4 after TOS of 11, 22, and 32 ks. Selectivity to naphthalene and higher aromatics decreased at longer TOS due to acid site deactivation caused by deposition of coke and heavy aromatics that acts to limit reactant access to such sites [59,116]. Consequently, C_2H_x selectivities increase at longer TOS.

Table 3.2 CH_4 conversion and product selectivity for DHA reactions over Mo/H-ZSM-5 catalyst at 950 K, CH_4 flow rate 12.0 $cm^3\,min^{-1}$, CH_4:Ar = 9:1, and catalyst loading 1 g with Mo:Al_f = 0.25.

Time-on-stream (ks)	11	22	32
CH_4 conversion (%)[a]	8.8	7.9	7.6
Selectivity (%)[b]			
C_2H_4	2.0	2.6	3.3
C_2H_6	2.1	2.4	2.8
C_6H_6	60.3	66.0	68.0
C_7H_8	3.0	3.7	4.0
$C_{10}H_8$	28.0	22.5	19.3
C_{10}^+	2.7	1.7	1.4

[a] $Conv_{CH_4} = \frac{F_{CH_4}^{Inlet} - F_{CH_4}^{Outlet}}{F_{CH_4}^{Inlet}}$ [b]See Equation 3.1

3.3.3 Steady-state dehydroaromatization of CH_4 over MoC_x/H-ZSM-5 catalysts with and without H_2 co-feed

A systematic study of CH_4 DHA reactions at different catalyst loadings was conducted to elucidate the effect of H_2 formed during the reaction. H_2 and C_6H_6 partial pressures monotonically increased with catalyst loading while CH_4 partial pressure monotonically decreased as shown in Figure 3.4. The concentration of H_2 does not increase linearly with catalyst loading; rather it increases sharply in the first 0.1 g of the bed then grows at a more moderate rate to the full 1.0 g. Concurrently, the net rate of C_6H_6 formation (R_{net}) decreased monotonically with catalyst loading as also shown in Figure 3.4. These results indicate that the abundant amounts of H_2 produced in the catalyst bed inhibit CH_4 pyrolysis by equilibrium effects or by reacting with active carbon species which suppresses C-C bond formation [59]. The steady but small increase in H_2 outlet pressure at loadings greater than 0.3 g suggests that there may be an effective CH_4 pyrolysis regime after which DHA reactions are shutdown due to high concentrations of H_2. Figure 3.4 also presents C_6H_6 approach to equilibrium, η, as a function of catalyst loading. η is calculated via Equation 3.2 using outlet pressures and the equilibrium constant determined from thermodynamic values at 950 K (K_{eq} = 0.0302). Equation 3.2 is derived from the stoichiometric reaction of CH_4 to H_2 and C_6H_6, as shown in Equation 3.3. The increase in η can be

$$\eta = \frac{P_{C_6H_6}^{1/6} * P_{H_2}^{3/2}}{P_{CH_4} * K_{eq}} \tag{3.2}$$

$$CH_4 \overset{K_{eq}}{\rightleftharpoons} \frac{3}{2} H_2 + \frac{1}{6} C_6H_6 \tag{3.3}$$

explained by the increase in H_2 pressure and its strong dependence on that pressure. The decrease in R_{net} indicates that the catalyst is more efficient at producing benzene upstream as compared to downstream purely due to equilibrium limitations. R_{net} is related to η with the forward formation rate (R_{for}) as shown in Equation 3.4. R_{for} is determined using calculated values of R_{net} and η which are obtained from analysis of the reactor effluent. In order to account for the changing reactant and product pressures, Equation 3.5, which is analogous to Equation 3.4, was used to calculate R_{for}. The derivation for this R_{for} calculation is presented in section 3.5. The forward rate of benzene formation with CH_4 feed only was calculated to be 0.47 ± 0.08 x 10^{-3} mol/(g- atom Mo-s) and was invariant with catalyst loading, as shown in Figure 3.4. This result shows that an increase in catalyst loading which causes an increase in H_2 pressure has no kinetic consequences on the rate-limiting step of CH_4 DHA and that all effects of H_2 are thermodynamic in nature.

$$R_{net} = R_{for} * (1 - \eta) \tag{3.4}$$

$$R_{for}(x) = \frac{\overline{R}_{net} * \Delta x}{\int_x^{x+\Delta x} [1 - \eta(x)] dx} \tag{3.5}$$

The effects of H_2 can be independently confirmed in co-feed experiments in which H_2 is added to the inlet feed of the reactor. Figure 3.5 shows C_6H_6 production as the H_2/CH_4 ratio is successively increased from 0.0 to 0.3 at time ~12-27 ks. The addition of H_2 results in a shift in equilibrium and a higher value of η (Equation 3.2) which causes a decrease in the net rate of benzene formation. Once H_2 is removed from the inlet at ~27 ks, R_{net} recovers to its original value at ~12 ks. Addition of H_2 causes no permanent changes to catalyst performance and therefore, no irreversible structural or chemical change to the MoC_x moieties that exist during CH_4 pyrolysis. This does not include H_2 regenerating activity as was observed by Zhang and co-workers during CH_4/H_2 switching experiments as these

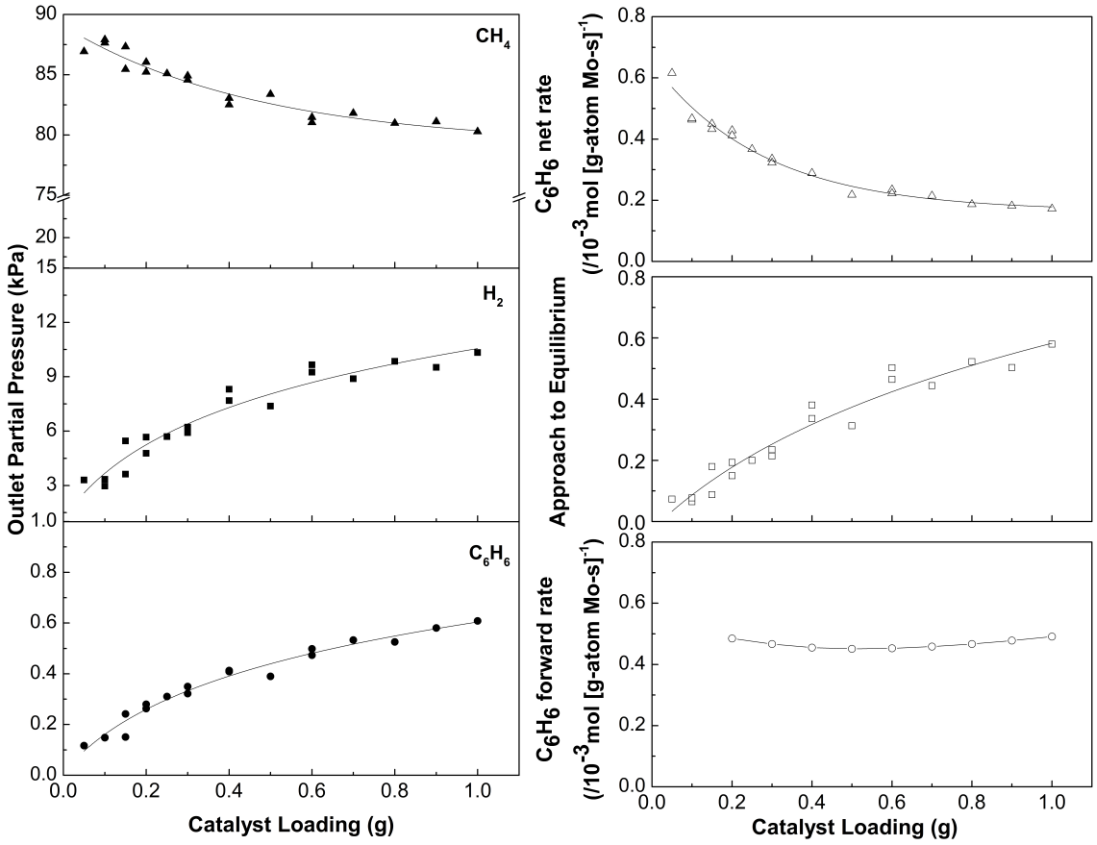

Figure 3.4 CH_4 (▲), H_2 (■), and C_6H_6 (●) outlet partial pressure and R_{net} (△), η (□), and R_{for} (○) as a function of catalyst loading at 950 K, CH_4 flow rate 12.0 $cm^3\,min^{-1}$, CH_4:Ar = 9:1, and catalyst weight 0.05-1.0 g with Mo:Al_f = 0.25.

effects were not investigated in this report [117]. An independent set of experiments with H_2/CH_4 co-feeds (0.03-0.11 molar ratio) at various catalyst loadings (0.2-1.0 g) were done to probe the thermodynamic and kinetic effects of co-processing H_2. Similar to CH_4 only reactions, H_2 and C_6H_6 partial pressures monotonically increased with catalyst loading while CH_4 pressures monotonically decreased as shown in Figure 3.6. At equal catalyst loadings, a higher inlet H_2/CH_4 ratio resulted in a systematic decrease in the C_6H_6 and CH_4 outlet partial pressure while the H_2 pressure increased. Plots of η and R_{net} with H_2 co-feed shown in Figure 3.6 (H_2/CH_4 = 0.03-0.11, 0.1-1.0 g) have similar trends with respect to catalyst loading when compared with CH_4 only reactions (0.05-1.0 g) shown in Figure 3.4. At equal catalyst loadings, higher inlet H_2/CH_4 ratios caused a systematic decrease in C_6H_6 R_{net} while η increased. R_{for} was calculated at each inlet H_2/CH_4 ratio using Equation 3.5. R_{for} values are invariant with respect to catalyst loading and H_2 pressure as presented in Table 3.3 and plotted in

Figure 3.6. Statistical analysis of these data was done as adapted from Taylor [118] and described in section 3.5. The average R_{for} for all H_2 co-feed experiments is 0.38 ± 0.05 x 10^{-3} mol/(g-atom Mo-s). An independent set of experiments at constant CH_4 pressure (83 kPa) and varying H_2/CH_4 ratios (H_2/CH_4 = 0.0 – 0.11) also confirmed that forward rates for CH_4 dehydroaromatization were invariant with hydrogen pressures (section 3.5.3). These results show that artificial and successively higher H_2/CH_4 ratios have no kinetic effects on the rate-limiting step of DHA reactions. This model which accurately describes the hydrogen pressure and its concomitant

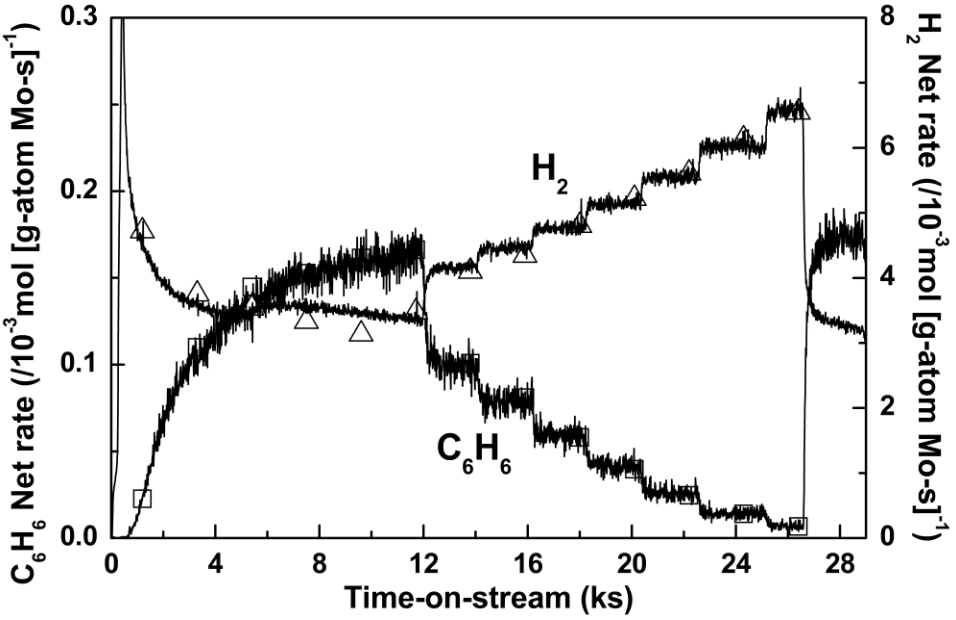

Figure 3.5 C_6H_6 (Δ) and H_2 (□) net formation rates at 950 K, CH_4 flow rate 12.0 cm^3 min^{-1}, CH_4:Ar = 9:1, catalyst loading 1.0 g with Mo:Al_f = 0.25. Inlet H_2/CH_4 = 0.00, 0.09, 0.12, 0.15, 0.17, 0.21, 0.23, 0.27, and 0.00. Symbols are GC data and lines are MS transient data.

Table 3.3 Forward rate of benzene synthesis at different H_2/CH_4 and AA/CH_4 inlet ratios. Reaction conditions: Temperature, 950 K; CH_4 flow rate, 12.0 cm^3 min^{-1}; CH_4:Ar = 9:1; catalyst loading, 0.1-1.0 g; Mo/Al_f = 0.25.

H_2/CH_4	0.0	0.03	0.06	0.08	0.11
R_{for} ($\frac{10^{-3}\text{mol}}{\text{g-atom Mo-s}}$)	0.47 ± 0.08	0.39 ± 0.05	0.41 ± 0.07	0.34 ± 0.05	0.38 ± 0.02
AA/CH_4	0.0	0.02	0.03	0.04	0.05
R_{for} ($\frac{10^{-3}\text{mol}}{\text{g-atom Mo-s}}$)	0.47 ± 0.08	0.50 ± 0.04	0.48 ± 0.08	0.39 ± 0.02	0.43 ± 0.02

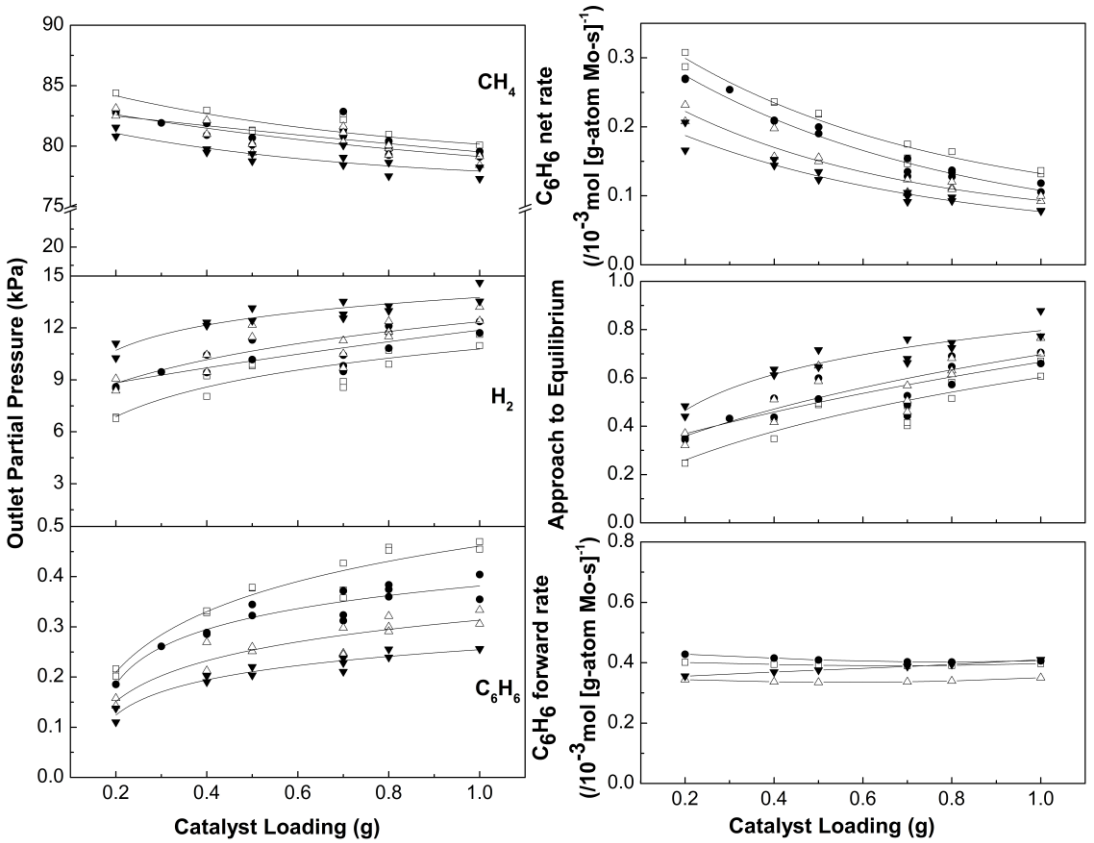

Figure 3.6 CH_4, H_2, and C_6H_6 outlet partial pressure and R_{net}, η, and R_{for} as a function of catalyst loading at 950 K, CH_4 flow rate 12.0 $cm^3\ min^{-1}$, CH_4:Ar = 9:1, and catalyst weight 0.05-1.0 g with Mo:Al_f = 0.25. Inlet H_2/CH_4 = 0.03 (□), 0.06 (●), 0.08 (△), and 0.11 (▼).

effects on benzene synthesis R_{for} shows that all effects of H_2 can be described consistently based on reversibility and equilibrium considerations. These conclusions constitute an alternative model to that described by Iglesia and co-workers which considered the hydrogen pressure in the bed to be an average of the inlet and outlet pressures and concluded that H_2 inhibits DHA rates due to both thermodynamic and kinetic effects [59].

3.3.4 Steady-state dehydroaromatization of CH_4 over MoC_x/H-ZSM-5 catalysts with acetic acid co-feed

Acetic acid (AA) was introduced as a co-reactant with CH_4 to a fully carburized MoC_x/H-ZSM-5 catalyst to assess the kinetic and thermodynamic consequences of co-processing oxygenates on the rate of CH_4 DHA. Figure 3.7

shows product formation rates as a function of time-on-stream (TOS). AA was not detected in the effluent while oxygen containing species in the effluent were predominantly CO (>95%) with negligible amounts of H_2O and CO_2. The addition of AA to CH_4 reactant streams (AA/CH_4 = 0.1) induced significant changes in the formation rates of benzene, naphthalene, hydrogen, and CO: the formation rate of aromatics decreased by ~85% while the formation rate of C_2 hydrocarbons decreased by ~25%. After the initial rate change, product formation rates were steady for 3 hours (Figure 3.7b). After reacting a co-feed of AA and CH_4 for 3 hours, the flow was switched to Ar (0.21 $cm^3\ s^{-1}$) for 1.2 ks to remove residual AA and H_2 from the reactor. After this period the feed was switched to CH_4 and the resulting product formation rates recovered to their previous values before the introduction of the AA co-feed (Figure 3.7c) suggesting that the oxygenate co-feed does not redisperse the Mo-species or irreversibly deactivate the catalyst.

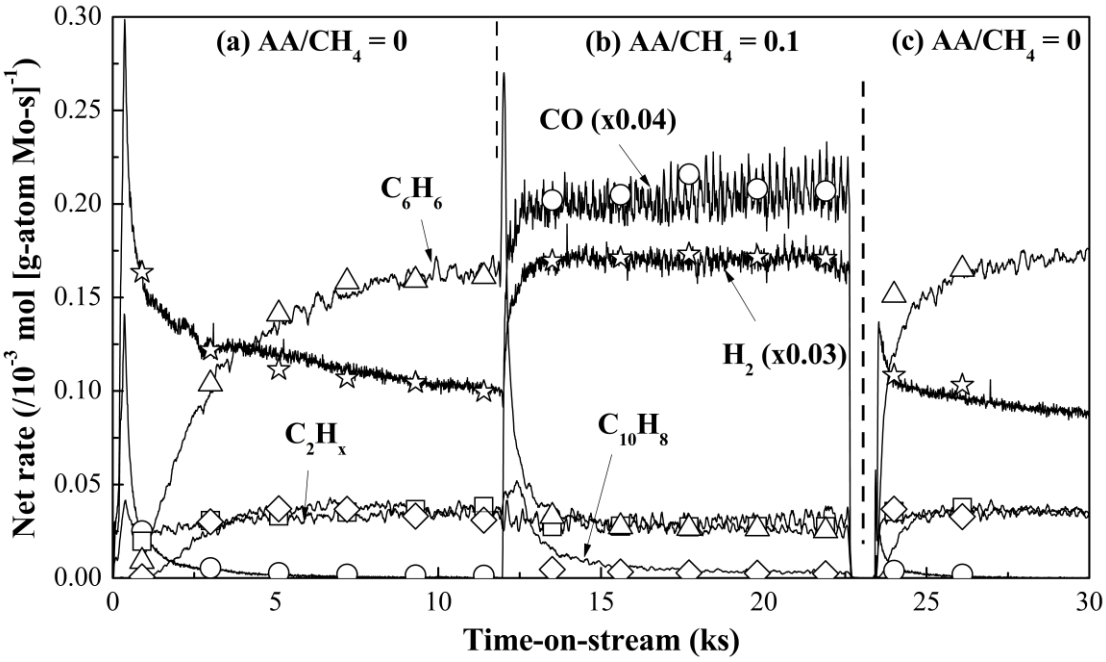

Figure 3.7 Transient product formation rates with acetic acid co-feed on Mo/H-ZSM-5 5 at 950 K, CH_4 flow rate 12.0 $cm^3\ min^{-1}$, CH_4:Ar = 9:1, catalyst loading 0.1-1.0 g with $Mo:Al_f$ = 0.25, and AA/CH_4 = 0.1. Product: C_6H_6 (△), H_2 (☆), C_2H_x (□), $C_{10}H_8$ (◇), and CO (○). Symbols are GC data and lines are MS transient data.

In X-ray photoelectron spectroscopic experiments, Rosynek and co-workers observed the appearance of peaks at a binding energy of 228 eV corresponding to Mo_2C and the disappearance of peaks at a binding energy of 233 eV corresponding to Mo^{6+} upon introduction of CH_4 to oxidized Mo/ZSM-5 at 973 K [51]. After subsequent introduction of CO_2 to the sample, binding energies corresponding to Mo_2C (228 eV) disappeared while binding energies corresponding to oxidized Mo appeared (233 and 229.5 eV for Mo^{6+} and Mo^{4+} respectively). Based on these observations, the authors concluded that introduction of CO_2 caused re-oxidation of Mo. In Raman spectroscopic experiments, Li and co-workers observed, (i) bands at 960 cm^{-1} corresponding to Mo=O stretching disappeared and bands at 1600 cm^{-1} corresponding to coke species appeared with introduction of CH_4 to a fresh MoO_x/HZSM-5 catalyst, (ii) bands at 1600 cm^{-1} decreased while bands at 960 cm^{-1} reappeared with introduction of O_2 up to a O_2/CH_4 ratio of 0.0065, and (iii) bands at 1600 cm^{-1} disappeared while bands at 960 cm^{-1} increased further with introduction of O_2 above an O_2/CH_4 ratio of 0.0065 [119]. Based on these observations, the authors concluded that as the O_2/CH_4 ratio increased, MoC_x gradually reoxidized and coke deposits decreased suggesting a reduction in aromatic synthesis. The oxidation of MoC_x to MoO_x and a concomitant decrease in the number of active sites is consistent with the dramatic decrease in aromatic synthesis rates with the introduction of AA as MoO_x/H-ZSM-5 is unavailable for CH_4 activation in the presence of AA. While these reports suggested complete re-oxidation of MoC_x to MoO_x, the possibility for the existence of a Mo-oxycarbide phase (MoC_xO_y) cannot be excluded because, as noted by Chen and co-workers, an oxygen modified Mo (110) carbide catalyst results in Mo-carbide like activity towards oxygenate decomposition [120].

The decrease in aromatic formation rate is also caused by an increase of H_2 pressure formed in reforming reactions of CH_4, comparable to the thermodynamic effect of H_2 noted in Figure 3.5. The effect of co-feeding AA is therefore, two-fold: production of H_2 from CH_4 reforming by AA resulting in shifted equilibrium of CH_4 DHA and the presence of O^* resulting in MoC_x oxidation and essentially making a fraction of the sites unavailable for C_6H_6 production. Lacheen and co-workers reported lower pyrolysis yields in CO_2/CH_4 (0-0.1 molar ratio) co-feed experiments resulting from a shorter active catalyst bed available for reactions due to CO_2 scavenging of active C^* required for chain growth at the beginning of the bed [59]. Further investigations led the researchers to describe the catalyst bed during CO_2/CH_4 reactions as two distinct zones: one an upstream oxygenate

reforming zone dominated by reverse Boudouard reactions that completely suppress CH_4 pyrolysis; and two a downstream CH_4 pyrolysis zone present after all oxygenate was consumed. The extent of the reforming zone is related to the CO_2/CH_4 ratio and the activity of the pyrolysis zone is directly affected by the amount of H_2 produced in the reforming zone due to reversibility. The pyrolysis zone, active for CH_4 DHA, has an inlet feed of CH_4 as well as CO and H_2, the products of oxygenate reforming. The kinetic and thermodynamic effects of co-processing AA require us to calculate forward rates of benzene synthesis after rigorously assessing the fraction of the bed that is inhibited by O^* and the H_2 pressure at the end of the reforming zone.

Inlet AA/CH_4 ratio was systematically increased by increasing AA feed rate (0.9-3.2 x 10^{-3} $cm^3\,s^{-1}$) until CO_2 was observed in the reactor effluent stream. Figure 3.16 shows C_6H_6 production decrease as the AA/CH_4 ratio increases. Competitive CH_4 DHA and AA pyrolysis reactions make the AA to CH_4 ratio the independent variable when determining how much of the catalyst bed is unavailable for C_6H_6 production and instead only results in upstream reforming of CH_4 to produce H_2/CO mixtures. At $AA/CH_4 = 0.048$, CO_2 production increases by an order of magnitude and C_6H_6 production decreases to less than 10% of that observed at $AA/CH_4 = 0.0$. The AA/CH_4 ratio at which CO_2 is observed to break through the reaction bed is designated as the AA/CH_4 ratio where no Mo sites are available to produce C_6H_6. Independent experiments were conducted at different catalyst loadings to obtain a relationship between the AA/CH_4 ratio and the weight of catalyst oxidized and therefore unavailable to produce C_6H_6. These AA/CH_4 ratios and corresponding catalysts weights are presented in Figure 3.8.

The amount of catalyst unavailable for CH_4 DHA in CH_4/AA co-feed experiments can be independently determined by using the stoichiometric reforming reaction of acetic acid to hydrogen and carbon monoxide. First, a relationship between catalyst loading and outlet partial pressure of H_2 must be known at different AA/CH_4 ratios. These data are shown in Figure 3.17. A function can be fitted through the data at each AA/CH_4 ratio to determine the pressure of hydrogen at any catalyst loading. Assuming at these reaction conditions all AA is converted to H_2 and CO since oxygen is discarded in the reaction primarily as CO (>95% selectivity), for every molecule of AA fed to the reactor, two molecules of hydrogen are produced, as shown in Equation 3.6. The amount of H_2 produced from AA is then known at each AA/CH_4 ratio. Using this value as the partial pressure of H_2 and the fitted functions from Figure 3.17, a projected value of catalyst weight can be determined that is essentially the

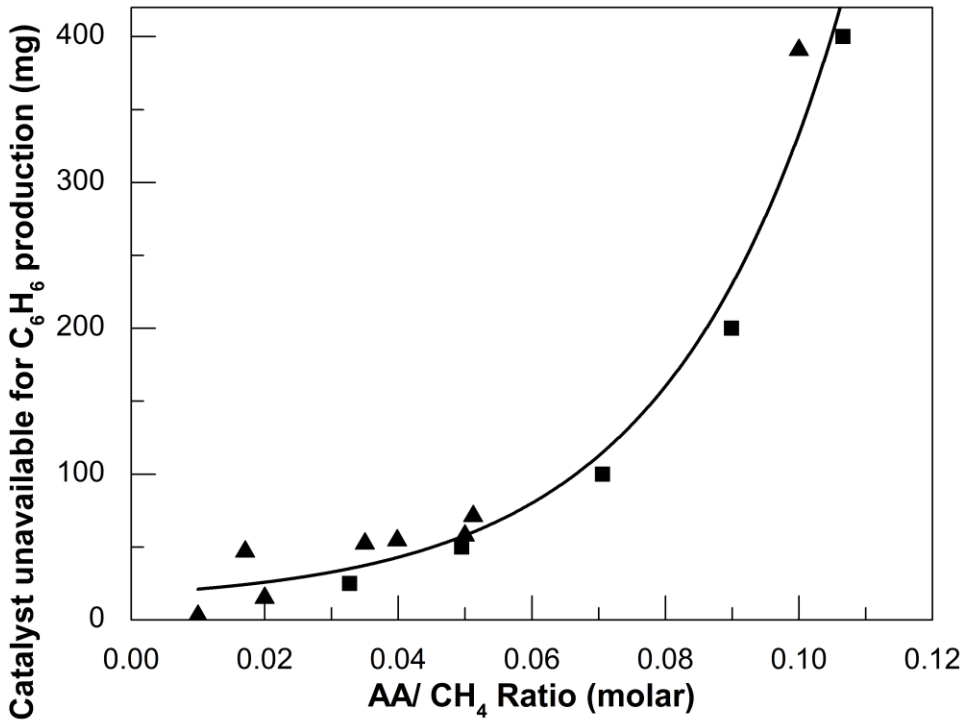

Figure 3.8 Amount of catalyst unavailable to produce C_6H_6 due to the presence of AA as a function of AA/CH_4 ratio. Data from CO_2 breakthrough experiments (■) and AA stoichiometric experiments (▲).

$$CH_3CO_2H \rightarrow 2CO + 2H_2 \tag{3.6}$$

amount of catalyst needed to decompose the set amount of AA to H_2 and CO. Once this is known for each AA/CH_4 ratio, another relationship between the AA/CH_4 ratio and amount of catalyst unavailable to produce C_6H_6 can be obtained which is an independent method for assessing the amount of catalyst oxidized from the CO_2 breakthrough method discussed above. Figure 3.8 presents these data overlaid on the same plot. The data from the two separate methods for assessing the fraction of the bed oxidized based on the AA/CH_4 ratio agree and a function can be fitted through the concatenated data set so that the amount of catalyst unavailable for C_6H_6 synthesis can be determined at any AA/CH_4 ratio in range.

R_{for} is first calculated with Equation 3.4 using outlet values of product partial pressures to determine η with Equation 3.2. Due to the non-uniformity of the H_2 pressure, R_{for} would decrease with catalyst loading if calculated using outlet partial pressures and Equation 4. By using Equation 3.5, the H_2 pressure

can be correctly described at each point of the catalyst bed and an invariant R_{for} with catalyst loading results, as shown in Figure 3.4 and 3.6. A correction for the amount of catalyst unavailable for CH_4 DHA is needed for AA co-feed reactions. This adjustment is made with the model presented in Figure 3.8. Once the number of Mo sites available when using AA/CH_4 co-feeds is known, the correct value for R_{for} can be calculated. This procedure was used to calculate R_{for} for AA/CH_4 co-feed experiments.

An independent set of experiments was conducted to confirm the relationship between the AA/CH_4 ratio and amount of catalyst unavailable for CH_4 DHA. One experiment involved 1000 mg of catalyst and an AA/CH_4 ratio of 0.10. From the trendline shown in Figure 3.8, it was determined that AA/CH_4 = 0.1 renders 390 mg of a 1000 mg bed unavailable for CH_4 DHA, as depicted in Figure 3.9. In the presence of AA, some of the MoC_x is oxidized to MoO_x which is unavailable for CH_4 DHA. Pyrolysis of AA produces some H_2, hence at the start of the CH_4 pyrolysis zone, the C_6H_6 partial pressure is zero but the H_2 partial pressure is non-zero. The second experiment involved using 610 mg of Mo/ZSM-5 catalyst with a feed of H_2 and He at a ratio of 0.20 to that of the CH_4

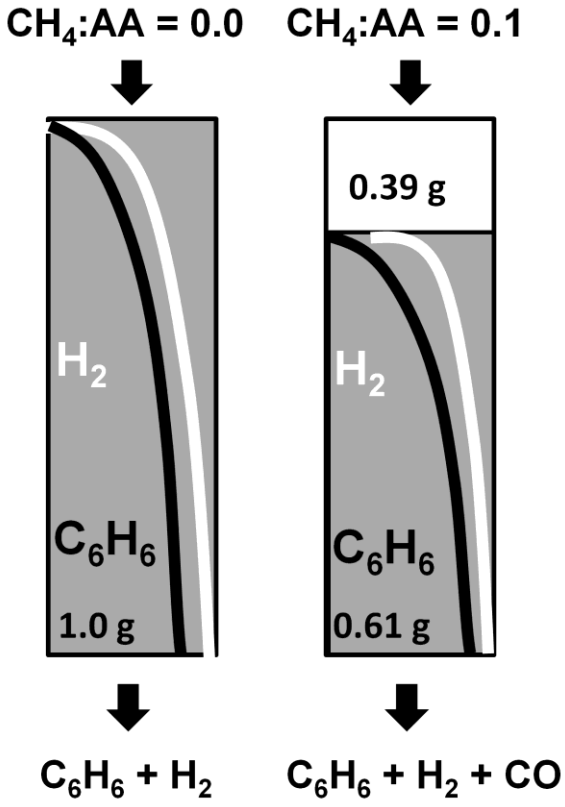

Figure 3.9 Depiction of a CH_4 DHA reactor bed with and without AA co-feed.

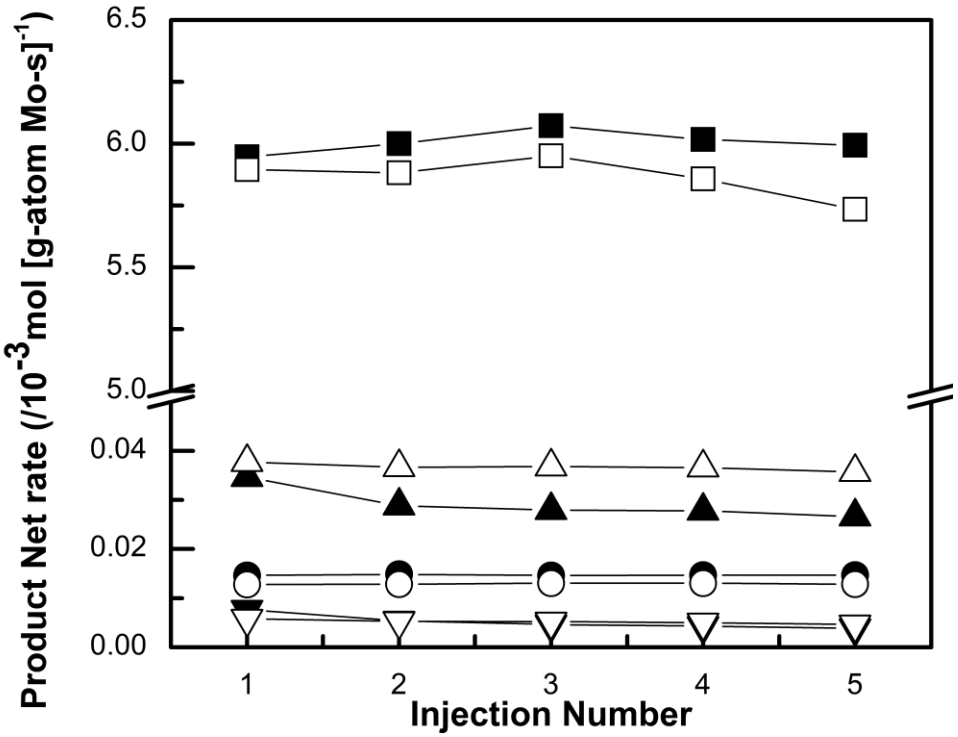

Figure 3.10 H_2 (■), C_6H_6 (▲), C_2H_4 (●), and $C_{10}H_8$ (▼) formation rates. Filled symbols: T = 950 K, CH_4 flow rate 12.0 $cm^3\,min^{-1}$, CH_4:Ar = 9:1, AA/CH_4 = 0.10, and 1.0 g catalyst with Mo:Al_f = 0.25. Empty symbols: T = 950 K, CH_4 flow rate 12.0 $cm^3\,min^{-1}$, CH_4:Ar = 9:1, H_2:CH_4 = He:CH_4 = 0.20, and 0.61 g catalyst with Mo:Al_f = 0.25.

feed. It is known that CO co-feed has no effect on hydrocarbon formation rates at these conditions, therefore inert He was used in place of CO as a safety precaution [60]. Nearly identical product formation rates were observed in the two independent experiments as shown in Figure 3.10, suggesting that the two models above can be used to correctly adjust for the fraction of the catalyst bed upstream that is oxidized in presence of AA and therefore, rendered unavailable for CH_4 pyrolysis and C_6H_6 production.

A systematic study of CH_4 DHA reactions at various catalyst loadings and different AA/CH_4 inlet ratios was shown to have similar trends as compared to CH_4 and CH_4/H_2 reactions with respect to product and reactant partial pressures as presented in Figure 3.11. Plots of η and R_{net} shown in Figure 3.11 also show similar trends with respect to catalyst loading when compared to CH_4 and CH_4/H_2 reactions. The outlet R_{net} was adjusted to account for the amount of Mo unavailable to produce C_6H_6 by using the model in Figure 3.8. R_{for} was calculated at each inlet AA/CH_4 ratio with Equation 3.5. R_{for} is invariant with respect to

catalyst loading as well as H_2 and AA pressure as evident from the results presented in Figures 3.6 and 3.11 and in Table 3.3; the average R_{for} for all AA/CH_4 co-feed experiments is 0.45 ± 0.05 x 10^{-3} mol/(g-atom Mo-s). These results show that successively higher AA/CH_4 ratios have no kinetic effects on the rate-limiting step of DHA reactions. Increased AA feed produces more H_2 from AA reforming reactions which only causes thermodynamic changes in the overall equilibrium of CH_4 to C_6H_6. Figure 3.12 presents the average forward rate as a function of catalyst loading for CH_4, CH_4/H_2, CH_4/AA DHA reactions. The average considering all reactions is 0.42 ± 0.05 x 10^{-3} mol/(g-atom Mo-s). The forward rate of C_6H_6 production is invariant with respect to H_2 or AA co-feed within our ability to measure the rates at these reaction conditions.

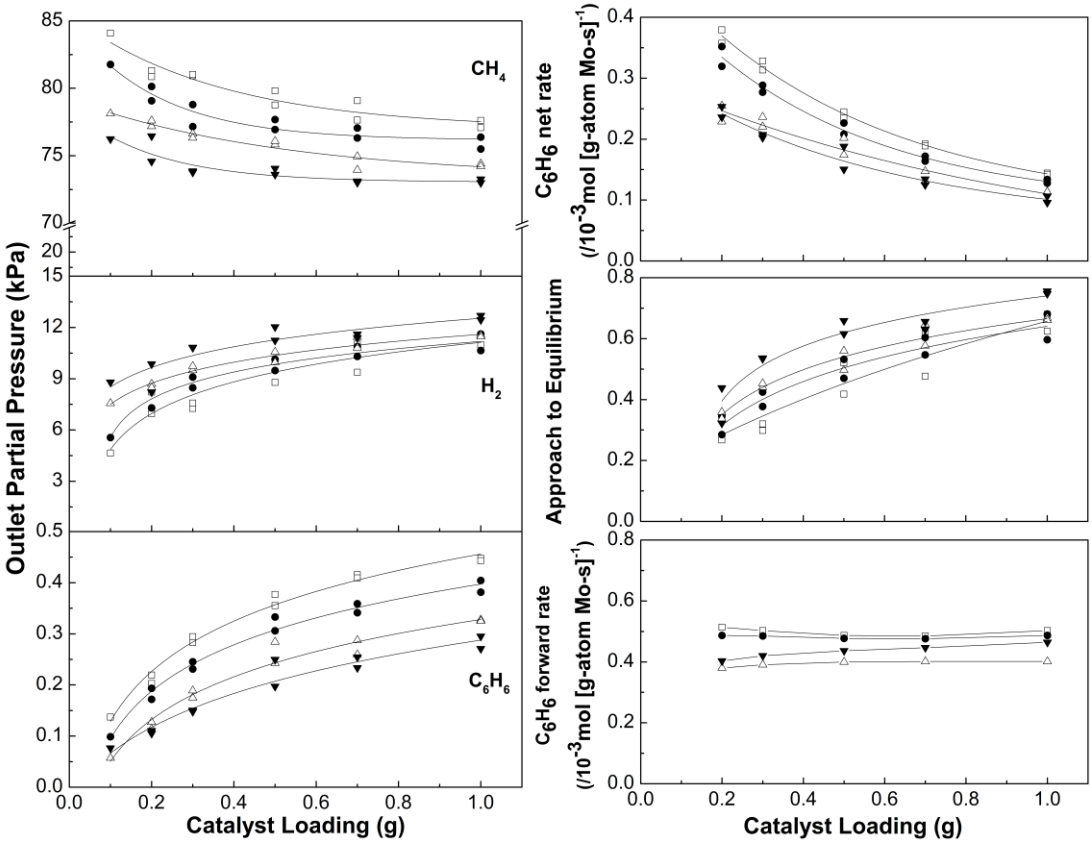

Figure 3.11 CH_4, H_2, and C_6H_6 outlet partial pressure and R_{net}, η, and R_{for} as a function of catalyst loading at 950 K, CH_4 flow rate 12.0 $cm^3\ min^{-1}$, CH_4:Ar = 9:1, and catalyst weight 0.05-1.0 g with Mo:Al_f = 0.25. Inlet AA/CH_4 = 0.02 (□), 0.03 (●), 0.04 (Δ), and 0.05 (▼).

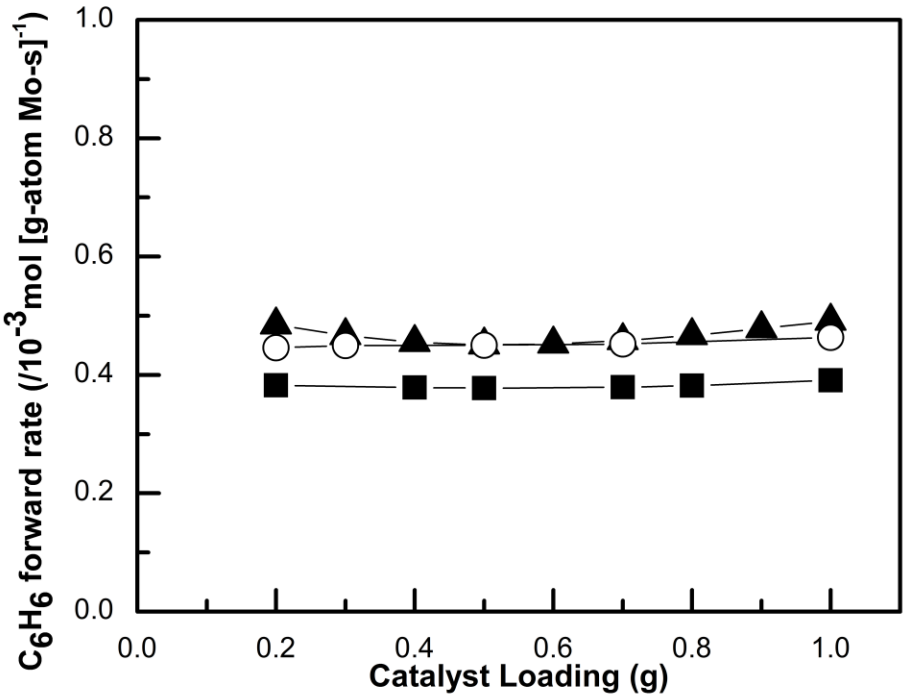

Figure 3.12 Average forward rate of C_6H_6 production as a function of catalyst loading. CH_4 (▲),CH_4/H_2 (■), and CH_4/AA (○).

Our studies in this report show that addition of H_2 and AA do not perturb forward rates of C_6H_6 synthesis, rather this addition causes a shift in the thermodynamic equilibrium of CH_4 to C_6H_6. Our ability to discriminate between the kinetic and thermodynamic effects of H_2 or AA addition is crucial to the understanding of how multi-functional catalysts concurrently accomplish dehydrogenation and deoxygenation.

3.4 Conclusions

Steady-state catalytic reactions of CH_4 with H_2 or AA co-feed over Mo/ZSM-5 at 950 K show that forward rates of C_6H_6 synthesis are unperturbed by addition of H_2 or AA. Measured effects of H_2 addition show that dehydroaromatization of CH_4 is governed by thermodynamic reversibility such that an increase in H_2 pressure causes a decrease in the net rate of C_6H_6 formation, but does not affect the forward synthesis rate. Measured effects of AA addition show that AA is first consumed in reforming reactions with CH_4 to produce CO and H_2 while oxidizing some active MoC_x sites with the extent of MoC_x oxidation dependent on the AA/CH_4 molar ratio. CH_4 DHA occurs on the

remaining MoC_x sites in an environment that includes H_2 produced from reforming reactions. Co-processing CH_4 with AA results in a higher H_2/CH_4 ratio which acts to shift the CH_4 to C_6H_6 equilibrium but does not affect the forward rate of C_6H_6 formation.

3.5 Supplemental information

3.5.1 Oxygen removal from MoO_x/ZSM-5

Figure 3.13 shows $O_{removed}$/Mo during carburization of 1.0 g of MoO_x/ZSM-5 with CH_4 (684 cm^3 g_{cat}^{-1} h^{-1}, 950 K). The final $O_{removed}$/Mo of 2.3 ± 0.1 after a carburization period of 10.8 ks is similar to the theoretical value of 2.5 O atoms per Mo, corresponding to exchanged $Mo_2O_5^{2+}$ dimers occupying two proximate Al sites.

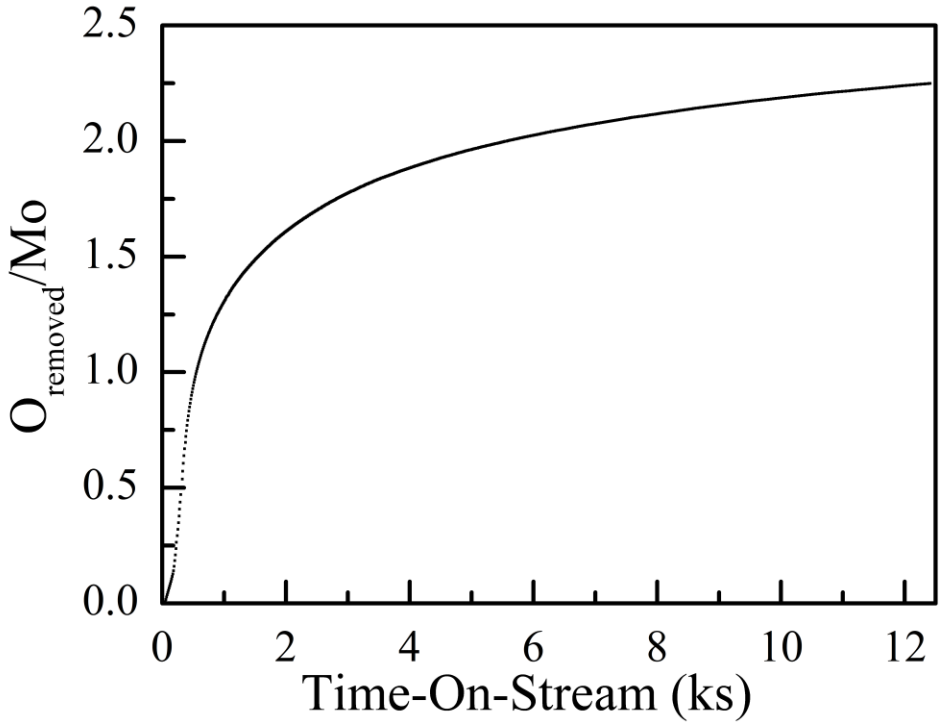

Figure 3.13 O atom removal from MoO_x/H-ZSM-5 catalyst (1.0 g) during carburization as measured by mass spectrometric analysis.

3.5.2 Mo K-edge X-ray absorption near edge structure spectroscopy

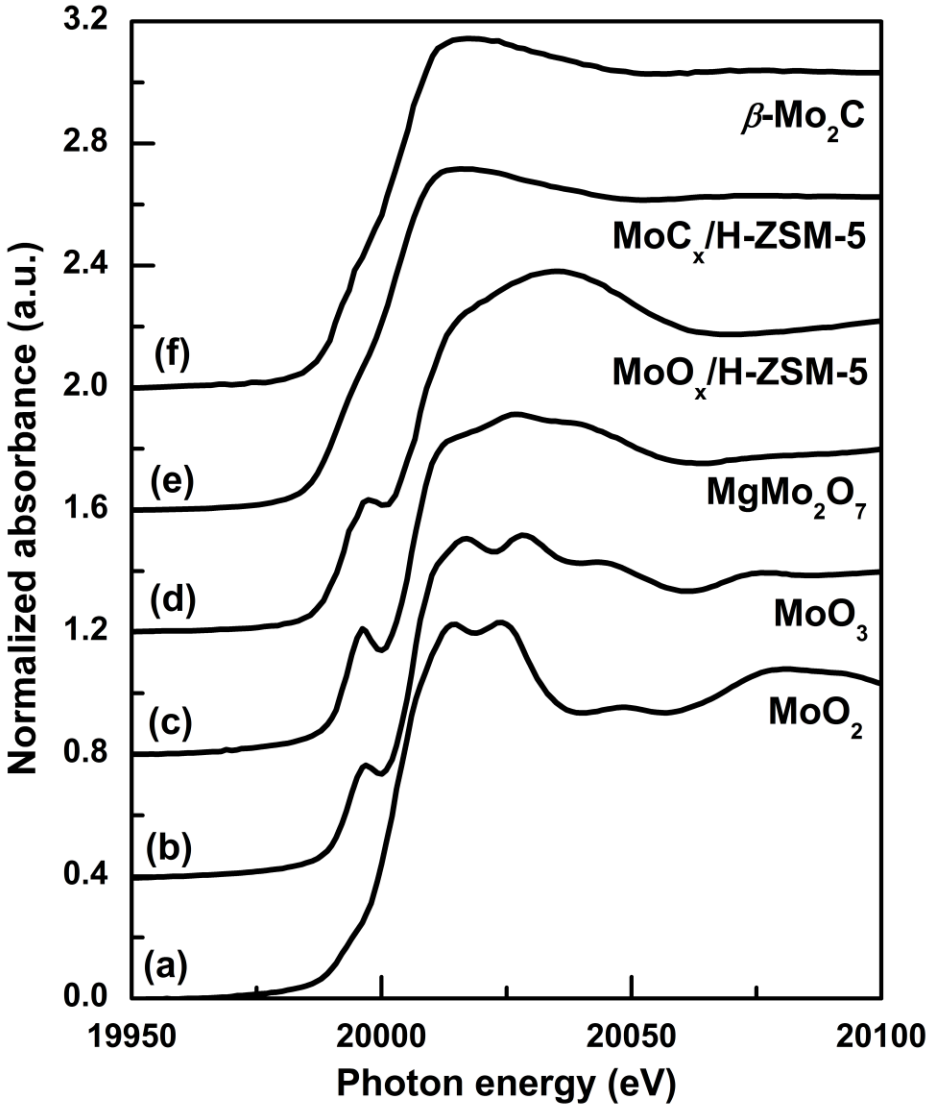

Figure 3.14 Mo K-edge XANES spectra of MoO_2, MoO_3, $MgMo_2O_7$, physical mixture of MoO_3/H-ZSM-5 post treatment in dry air at 973 K and post treatment in CH_4/Ar at 950 K, and β-Mo_2C.

Table 3.4 Edge energy of standard Mo oxides and Mo/H-ZSM-5 compounds relative to Mo foil edge energy (20 keV).

Compound	**ΔE_0 (eV)**
MoO_3	6.0
$MgMo_2O_7$	5.1
β-Mo_2C	3.8
MoO_x/HZSM-5 after treatment in air at 973 K	6.3
MoC_x/HZSM-5 after treatment in CH_4 at 950 K for 3 h	4.0

3.5.3 CH_4 dehydroaromatization with H_2 co-feed and constant CH_4 pressure

Independent data sets at constant CH_4 pressure (83 kPa) and varying H_2/CH_4 ratios (0.011-0.11; H_2 pressures 0-9 kPa) using 0.2-1.0 g of Mo/ZSM-5 catalyst were used to rigorously assess the effect of H_2 pressure on CH_4 DHA rates at constant CH_4 pressure. These data are reported in Figure 3.15. From these results and those presented in Table 3.5, we note that the forward rate for benzene synthesis is invariant with catalyst loading at varying H_2 pressures and constant CH_4 pressures. These results substantiate our inference reported in the manuscript for CH_4/H_2 co-processing experiments with H_2 pressures varying from 0-9 kPa and CH_4 pressures varying from 83-91 kPa, that the forward rate for benzene synthesis is independent of hydrogen pressures.

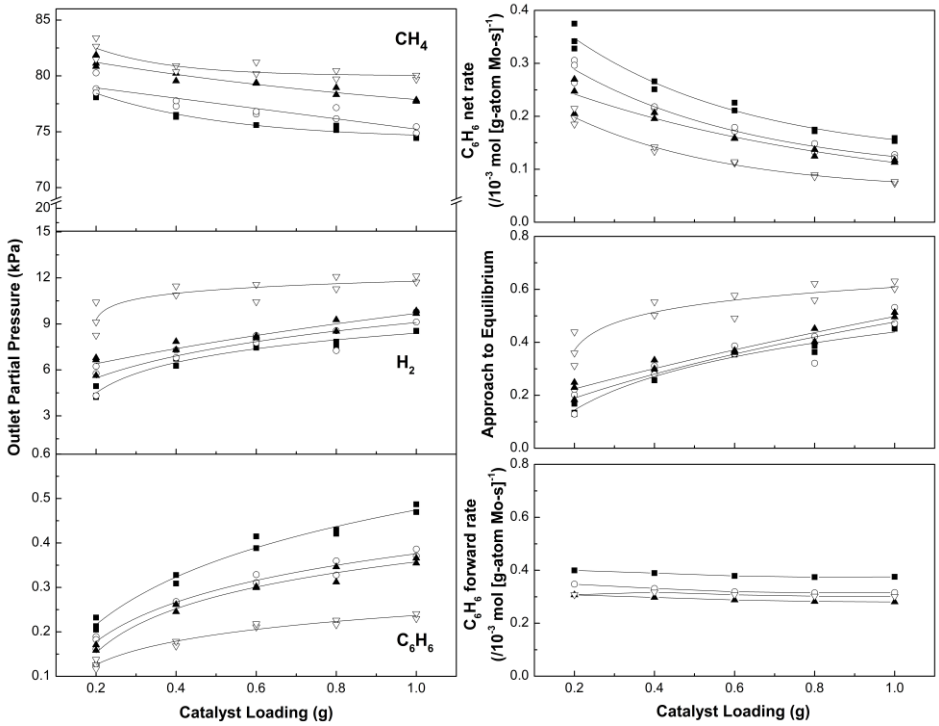

Figure 3.15 CH_4, H_2, and C_6H_6 outlet partial pressure and R_{net}, η, and R_{for} as a function of catalyst loading at 950 K, CH_4 flow rate 12.0 $cm^3\,min^{-1}$, constant P_{CH4} = 83 kPa, CH_4:Ar = 9:1, total flow 14.7 $cm^3\,min^{-1}$ balanced with He, catalyst loading 0.1-1.0 g, and Mo/Al_f = 0.25. Inlet H_2/CH_4 = 0.00 (■), 0.02 (○), 0.06 (▲), and 0.11 (▽).

Table 3.5 Forward rate of benzene synthesis at different H_2/CH_4 inlet ratios at constant P_{CH4} = 83 kPa. Reaction conditions: Temperature, 950 K; CH_4 flow rate, 12.0 $cm^3\,min^{-1}$; CH_4:Ar = 9:1; total flow 14.7 $cm^3\,min^{-1}$ balanced with He; catalyst loading, 0.1-1.0 g; Mo/Al_f = 0.25.

H_2/CH_4	0.0	0.02	0.06	0.11
R_{for} ($\frac{10^{-3}\text{mol}}{\text{g-atom Mo-s}}$)	0.38 ± 0.02	0.33 ± 0.02	0.29 ± 0.02	0.31 ± 0.02

We note that the variation in forward rates that we report in Table 3.5 is within the reproducibility of our measured rates. Independent data sets for CH_4/H_2 mixtures (83 kPa, H_2/CH_4 = 0.11) measured at 0.2, 0.4, 0.8, and 1.0 g using fresh Mo/ZSM-5 formulations for each experiment were used to assess forward rates of benzene synthesis and the results from these independent sets of experiments are reported in Table 3.6 below.

Table 3.6 Independently measured forward rates of benzene synthesis at different catalyst loadings (0.2-1.0g). (1) Reaction conditions: H_2/CH_4 = 0.11, temperature, 950 K; CH_4 flow rate, 12.0 $cm^3\ min^{-1}$; CH_4:Ar = 9:1; Mo/Al_f = 0.25. (2) Reaction conditions: H_2/CH_4 = 0.11, constant P_{CH4} = 83 kPa; temperature, 950 K; CH_4 flow rate, 12.0 $cm^3\ min^{-1}$; CH_4:Ar = 9:1; total flow 14.7 $cm^3\ min^{-1}$ balanced with He; Mo/Al_f = 0.25.

Catalyst Loading (g)	0.2	0.4	0.8	1.0
(1) R_{for} ($\frac{10^{-3}mol}{g\text{-atom Mo-s}}$)	0.36 ± 0.04	0.37 ± 0.01	0.39 ± 0.01	0.41 ± 0.01
(2) R_{for} ($\frac{10^{-3}mol}{g\text{-atom Mo-s}}$)	0.31 ± 0.03	0.32 ± 0.01	0.30 ± 0.01	0.30 ± 0.01

3.5.4 Calculation of R_{for} with error analysis

R_{for} is conventionally calculated with Equation 3.4 when the R_{net} and η are known. For the stoichiometric reaction of CH_4 to H_2 and C_6H_6, as shown in Equation 3.3, η is calculated from Equation 3.2 by knowing the partial pressures of each reactant and product as well as the equilibrium constant, K_{eq}. R_{net} is calculated by dividing the molar flow rate of C_6H_6 at the outlet of the reactor by the number of moles of Mo present in the catalyst bed. Equation 3.4 was adapted in order to account for the non-linear behavior of product and reactant partial pressures as a function of catalyst weight, as shown in Figure 3.5 of the manuscript. First, R_{net} and η were plotted as a function of catalyst weight and an equation was fitted through both sets of data. R_{net} was fitted with an exponential function and η was fitted with a logarithmic function and are given in Equations 3.10 and 3.11 respectively.

$$R_{for} = \frac{R_{net}}{(1-\eta)} \tag{3.7}$$

$$CH_4 \underset{}{\overset{K_{eq}}{\rightleftharpoons}} \frac{3}{2}H_2 + \frac{1}{6}C_6H_6 \tag{3.8}$$

$$\eta = \frac{P_{C_6H_6}^{1/6} * P_{H_2}^{3/2}}{P_{CH_4} * K_{eq}} \tag{3.9}$$

$$R_{net}(x) = A * \exp(\frac{-x}{t}) + y \tag{3.10}$$

$$\eta(x) = a - b * \ln(x + c) \tag{3.11}$$

CH_4 dehydroaromatization rates in the reactor were analyzed between discrete sections, for example between x and $x + \Delta x$. R_{net} of Equation 3.4 was

replaced with the average R_{net} between sections calculated from Equation 3.10, given in Equation 3.12. The term (1-η) of Equation 3.4 was replaced with an integral function to account for the upstream production of H_2 up to point $x + \Delta x$, given in Equation 3.13. R_{for} was transformed into $R_{for}(x)$, which accounts for the non-linearity of product and reactant partial pressures, after multiplying by Δx, to account for dx found in the integral (Equation 3.13), and is given in Equation 3.14. Using Equation 3.14 and fit parameters from Equations 3.10 and 3.11, R_{for} was determined at discrete points along the catalyst bed. An initial x of 0.2 g was used for all calculations.

$$R_{net} \rightarrow \overline{R}_{net}(x) = \frac{R_{net}(x) + R_{net}(x + \Delta x)}{2} \tag{3.12}$$

$$(1-\eta) \rightarrow \int_{x}^{x+\Delta x} [1-\eta(x)]dx \tag{3.13}$$

$$R_{for} \rightarrow R_{for}(x) = \frac{\overline{R}_{net}(x) * \Delta x}{\int_{x}^{x+\Delta x} [1-\eta(x)]dx} \tag{3.14}$$

Uncertainties in forward rates of benzene synthesis were determined using principal error analysis formulas found in Taylor [118]. Standard deviations between replicate data points (data at the same reaction conditions) were used as the standard error for that reaction condition and are denoted δx. Data points for R_{net} and η were plotted as a function of catalyst weight and Equations 3.10 and 3.11 respectively were fitted through the data. $R_{net}(x)$ and $\eta(x)$ were then calculated with this fit at each catalyst weight. As stated in Taylor, the error in a function q of one variable, $q(x)$, is the derivative of q with respect to x multiplied by the error in x, as given in Equation 3.15. The error in Equations 3.10 and 3.11 are then given in Equations 3.16 and 3.17. Equation 3.12 was used to calculate the average R_{net} and the error in this value is just the quadratic sum of the original errors, as given in Equation 3.18. The integral in Equation 3.13 was determined numerically with the formula given in Equation 3.19. The error in Equation 3.19 is calculated with Equation 3.20 which was derived from Equation 3.15. The Δx quantity in Equation 3.14 has no error as it is just the difference between

$$\delta q = \left|\frac{dq}{dx}\right| \delta x \,. \tag{3.15}$$

$$\delta R_{net}(x) = \left| \frac{-A}{t} * \exp(\frac{-x}{t}) \right| * \delta x_{R_{net}} \tag{3.16}$$

$$\delta \eta(x) = \left| \frac{-b}{c+x} \right| * \delta x_{\eta} \tag{3.17}$$

catalyst weights, which are known exactly. Finally, the error in the R_{for} is the sum in quadrature of the original fractional errors multiplied by R_{for}, and is given in Equation 3.21. This procedure was used to find the error in R_{for} at discrete catalyst weights for each reaction system studied: CH_4, CH_4/H_2, and CH_4/AA at different ratios. Average R_{for} values were calculated and the error in these averages was determined by calculating the quadratic sum of original errors and dividing by the square root of the number of data points, as given in Equation 3.22.

$$\delta \overline{R}_{net}(x) = \frac{\sqrt{\delta R_{net}(x)^2 + \delta R_{net}(x+\Delta x)^2}}{2} \tag{3.18}$$

$$\int_{x}^{x+\Delta x} [1-\eta(x)]dx = \begin{pmatrix} (x+\Delta x) - a*(x+\Delta x) - b*(x+\Delta x) + b*c \\ *\ln[c+(x+\Delta x)] + b*(x+\Delta x)*\ln[c+(x+\Delta x)] \end{pmatrix} - \begin{pmatrix} x - a*x - b*x + b*c* \\ \ln[c+x] + b*x*\ln[c+x] \end{pmatrix} \tag{3.19}$$

$$\delta \int_{x}^{x+\Delta x} [1-\eta(x)]dx = 1 - a - b + \frac{b*c}{c+x} + \frac{b*x}{c+x} + b*\ln[c+x] \tag{3.20}$$

$$\delta R_{for}(x) = \sqrt{\left(\frac{\delta \overline{R}_{net}(x)}{\overline{R}_{net}(x)} \right)^2 + \left(\frac{\delta \int_{x}^{x+\Delta x} [1-\eta(x)]dx}{\int_{x}^{x+\Delta x} [1-\eta(x)]dx} \right)^2} * R_{for}(x) \tag{3.21}$$

$$\delta \overline{R}_{for}(x) = \frac{\sqrt{\left(\delta R_{for}(x)\right)^2 + \left(\delta R_{for}(y)\right)^2 + \ldots\ldots + \left(\delta R_{for}(z)\right)^2}}{\sqrt{\#(x, y, \ldots\ldots, z)}} \tag{3.22}$$

3.5.5 Determination of catalyst unavailable for C_6H_6 synthesis

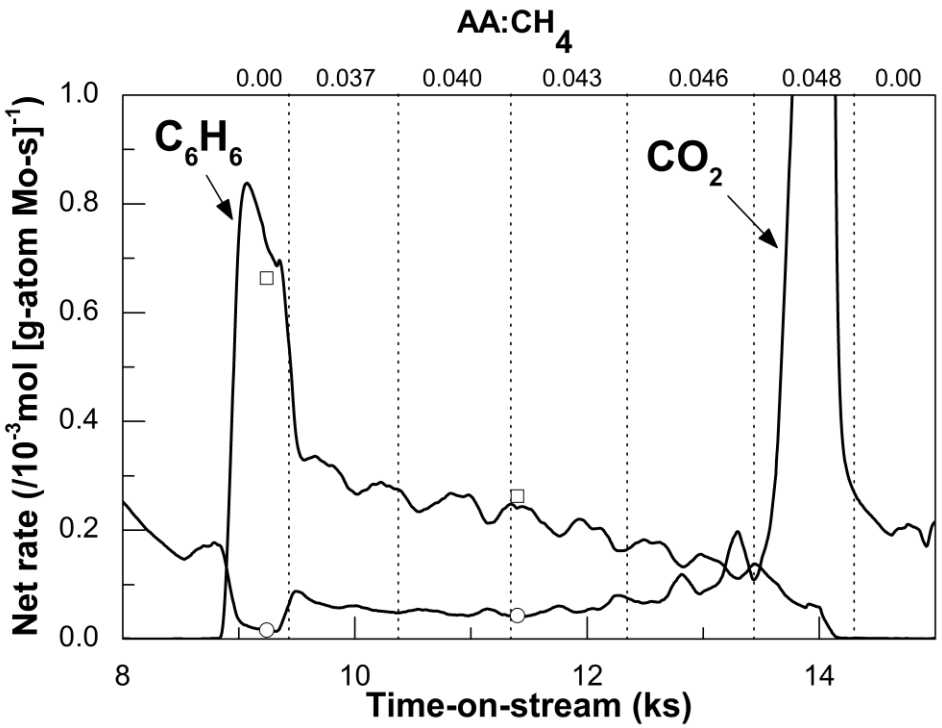

Figure 3.16 C_6H_6 (□) and CO_2 (○) net formation rates at 950 K, CH_4 flow rate 12.0 cm^3 min^{-1}, CH_4:Ar = 9:1, catalyst loading 50 mg with Mo:Al_f = 0.25. Inlet AA/CH_4 ratio = 0.00, 0.037, 0.040, 0.043, 0.046, 0.048, and 0.00. Symbols are GC data and solid lines are MS transient data.

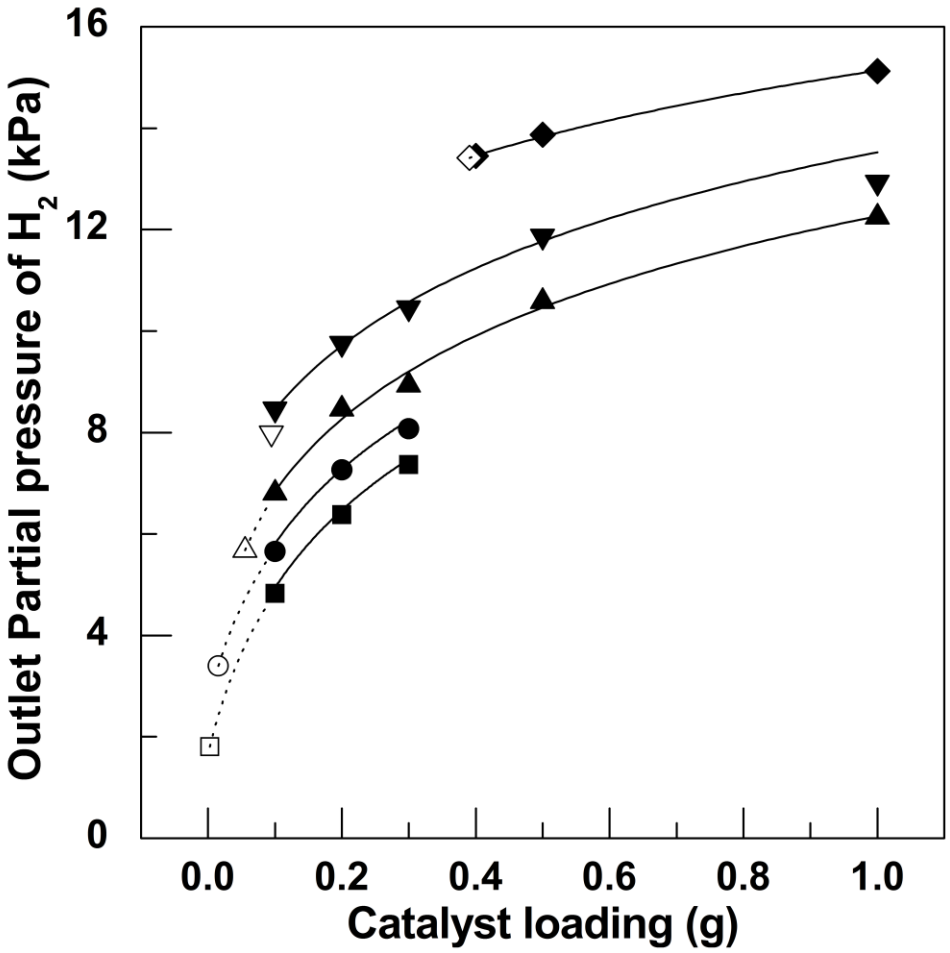

Figure 3.17 Outlet partial pressures of H_2 as a function of catalyst loading at different AA/CH_4 ratios. AA:CH_4 = 0.010 (■), 0.020 (●), 0.035 (▲). 0.050 (▼), and 0.100 (♦). T = 950 K, CH_4 flow rate 12.0 $cm^3\,min^{-1}$, CH_4:Ar = 9:1, and catalyst Mo:Al_f = 0.25. Open symbols depict projected catalyst weights obtained from partial pressures of H_2 as calculated from AA:CH_4 and stoichiometry.

CHAPTER

FOUR

CO-PROCESSING CH_4 AND OXYGENATES ON Mo/H-ZSM-5: CH_4/CO_2 AND CH_4/HCOOH MIXTURES*

4.1 Introduction

Biomass and natural gas are non-conventional sources of carbon for the synthesis of liquid fuels presently produced from petroleum.[7,13,52] The $(CH_2O)_n$ stoichiometry of biomass implies that its conversion to fuels requires the removal of oxygen; conversely, the synthesis of liquid fuels from CH_4 requires the removal of hydrogen. Therefore, a catalytic process that concurrently converts natural gas and biomass offers the potential to couple deoxygenation and dehydrogenation chemistries. In such a process, CH_4 would supply the hydrogen for removing oxygen from biomass-derived compounds.

The dehydroaromatization (DHA) of methane via high-temperature (~973 K) pyrolytic reactions on Mo/ZSM-5 catalysts represents a non-oxidative pathway for the catalytic conversion of methane to olefins and aromatics. The synthesis of aromatics and ethylene at near-equilibrium concentrations using molybdenum oxide modified H-ZSM-5 catalysts via non-oxidative conversion of CH_4 at 973 K was first described by Wang and co-workers.[50] Further studies encompassing the past two decades have reported high selectivity to benzene (> 70%) with 8-10% CH_4 conversion and stable catalytic rates during prolonged reactions (16 hours) using Mo/ZSM-5 catalysts at temperatures ~950 K.[51,54,82–85,87,89] Previously, we and others have described the catalyst as a

*Reported from Bedard, J. W., Hong, D.-Y., and Bhan, A., *Physical Chemistry Chemical Physics*, **15**, 12173-12179, (2013) – Reproduced by permission of the PCCP Owner Societies © 2013

$Mo_2O_5^{2+}$ dimer species occupying two adjacent Al centers before carburization through XANES analysis of the Mo K-edge and counting the number of O atoms removed per Mo atom during carburization.[92,121] Monomeric MoO_x species have been observed by Bao and co-workers as well as Ledoux and co-workers in Mo/ZSM-5 catalysts.[108–111] These structures can therefore not be excluded as potential active sites in CH_4 DHA, however, this issue was circumvented by normalizing all reported rates to the total number of Mo atoms which resulted in the lowest possible rate.[121] The concentration of accessible Brønsted acid sites increased during initial carburization (0.6 ks) due to the migration of Mo-oxo species to form MoC_x clusters and subsequently decreased at longer time-on-stream (10.8 ks) due to the adsorption of heavy aromatics formed during DHA reactions on Brønsted acid sites, as observed via dimethyl ether titration.[121]

Oxygenates have previously been exploited in this catalysis to counteract deactivation of the catalyst due to carbon deposition.[84,97] Ichikawa and co-workers ascribed improved Mo/ZSM-5 catalyst stability at long reaction times when co-feeding CO_2 with CH_4 due to the removal of carbonaceous species through the reverse Boudouard reaction.[98,99] In depth kinetic analysis into how the addition of CO_2 affected the Mo/ZSM-5 was reported by Lacheen and Iglesia wherein they described the reaction bed as having two zones.[59] The first zone contained CO_2 reforming reactions with CH_4 DHA being completely repressed and the second zone, which began once CO_2 was totally consumed, consisted of CH_4 pyrolysis reactions in an environment which contained CO and H_2 produced in the first zone. The researchers took into account the thermodynamic effects of additional H_2, produced from CO_2 reforming, by calculating forward rates of benzene synthesis and concluded that forward synthesis rates of benzene formation decrease with an increase of H_2 pressure. In our previous report, we offered an alternative model and presented data to confirm H_2 does not have any kinetic effects on DHA reactions of CH_4.[121] We measured hydrogen pressure as a function of catalyst loading in a series of independent experiments to postulate an accurate description of the thermodynamic consequences of hydrogen pressure on the forward rate of CH_4 DHA. Measured hydrogen pressures during CH_4 DHA using 0.2 g of Mo/ZSM-5 are greater than 50% of the measured value using 1.0 g of the catalyst suggesting that hydrogen pressures do not increase linearly in the catalyst bed as reported previously.[59] The model we have developed accounts for the disproportionate increase in hydrogen pressure upstream and its thermodynamic consequences on measured benzene synthesis rates to show that

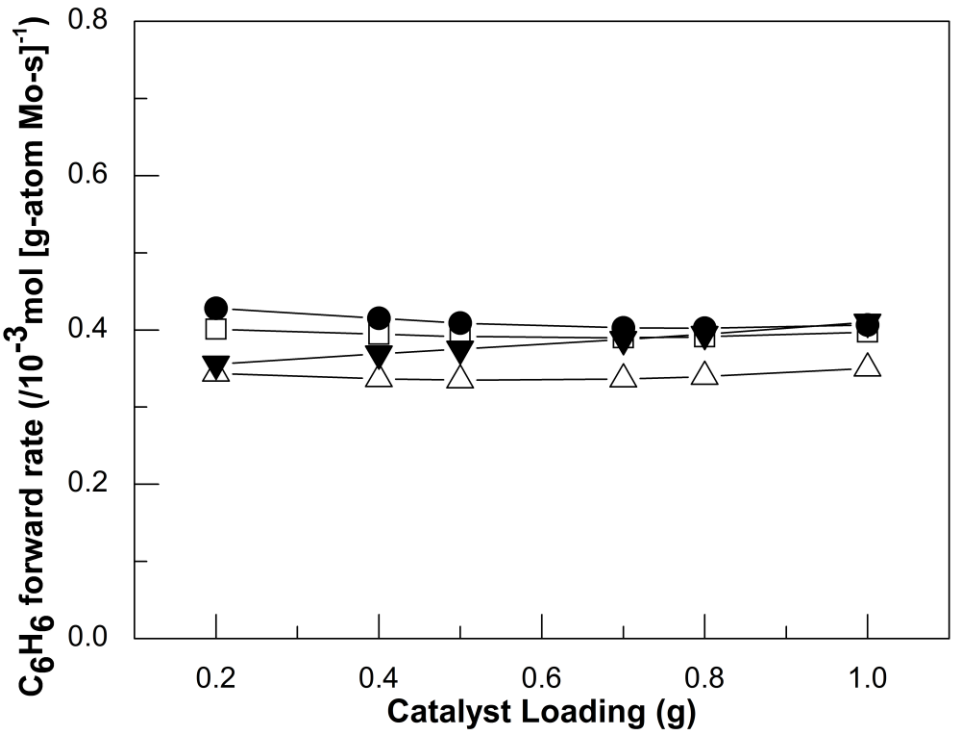

Figure 4.1 Forward rate of C_6H_6 formation as a function of catalyst loading at 950 K, CH_4 flow rate 12.0 $cm^3\,min^{-1}$, 1 atm, CH_4:Ar = 9:1, and catalyst weight 0.2-1.0 g with Mo:Al_f = 0.25. Inlet H_2/CH_4 = 0.03 (□), 0.06 (●), 0.08 (△) and 0.11 (▼).

the forward rate for methane DHA is invariant with the addition of hydrogen; this result contrasts prior reports in the literature.[59]

Figure 4.1 is an adapted plot from our prior report and shows that the forward rate of benzene synthesis is constant at different catalyst weights and varying H_2 to CH_4 ratios. Co-processing acetic acid with CH_4 was also investigated and a kinetic analysis of the data at varying CH_3COOH to CH_4 ratios (0.02-0.05) and catalyst weights (0.2-1.0 g) revealed that addition of CH_3COOH had no kinetic effects on the catalysis and that the forward rate was constant with respect to catalyst weight and CH_3COOH to CH_4 ratio.

In this report, we seek to extend this kinetic analysis to other oxygenates to determine the kinetic and thermodynamic effects of co-processing oxidants which vary in their chemical structure and reduction potential. Co-processing CH_4 with acetic acid, formic acid, and carbon dioxide on Mo/H-ZSM-5 catalysts results in a fraction of the active catalyst being oxidized by the oxygenate upstream to produce CO/H_2 mixtures while the remaining fraction of the active

catalyst performs CH_4 DHA reactions in an environment that includes CO and H_2 produced upstream. We postulate that at the high temperatures required to activate CH_4 in pyrolysis reactions, the oxygenate co-feed fragments to O* species and therefore, no effect of chemical functionality is observed when co-processing CO_2, HCOOH, or CH_3COOH. This research constitutes an example of co-processing a hydrogen rich (CH_4) feedstock with a hydrogen deficient (biomass surrogates) feedstock and highlights a critical limitation in coupling deoxygenation and dehydrogenation chemistries on MoC_x/ZSM-5 catalysts – the preferential selectivity to remove oxygen as CO instead of H_2O.

4.2 Materials and methods

The catalyst synthesis and reaction procedures were adapted from a previously published study and is presented here in brief.[121] A Mo/H-ZSM-5 catalyst was prepared using commercial NH_4-ZSM-5 zeolite (Zeolyst International, CBV 2314, Si/Al = 11.7) and MoO_3 powder (Sigma-Aldrich, 99.9%) by employing a solid state ion exchange procedure.[121] Steady-state catalytic reactions of CH_4/CH_3COOH, CH_4/HCOOH, and CH_4/CO_2 were conducted at 950 K and atmospheric pressure with 0.2-1.0 g of catalyst within a fixed bed, tubular quartz reactor (10 mm inner diameter). Liquid acetic acid (AA) (1.52×10^{-7} – 4.57×10^{-7} mol s^{-1}, Fluka, >99.8%) or liquid formic acid (FA) (1.40×10^{-7} – 4.20×10^{-7} mol s^{-1}, Sigma-Aldrich, >96%) or CO_2 (1.12×10^{-7} – 2.98×10^{-7} mol s^{-1}, research grade, Matheson) was introduced with CH_4 to the carburized catalyst once the benzene formation rate reached steady-state (1.8-10.8 ks depending on catalyst weight). The reactor effluent was analyzed with a gas chromatograph (Agilent 7890) and an on-line mass spectrometer (MKS Cirrus 200). Calculated product formation rates (mol [product] (g-atom Mo $s)^{-1}$) are reported as net rates or forward rates.

4.3 Results and discussion

Methane dehydroaromatization resulted in the synthesis of ethylene, ethane, benzene, toluene, xylenes, and naphthalene on Mo/H-ZSM-5 catalysts at T = 950 K at near equilibrium conversion (~10%) while co-processed oxygenates were converted to CO and H_2 at 100% conversion. Below, we present a rigorous and systematic analysis of DHA reactions of CH_4/AA, CH_4/FA, and CH_4/CO_2 mixtures to show that the forward rates of benzene synthesis are unperturbed by the addition of oxygenates. CH_4 conversion and product selectivities for these

three co-processing experiments are given in the Table 4.2. All effects of co-processing these oxygenates are strictly thermodynamic in nature at these reaction conditions.

4.3.1 Steady state dehydroaromatization of CH_4 on Mo/H-ZSM-5: Previous reports of H_2 and oxygenate co-processing

Previously, we investigated CH_4 DHA with and without H_2 co-feed to note that the production of H_2 was not uniform along the reaction bed while the observed net rate (R_{net}), normalized per Mo atom, decreased with increasing catalyst weight.[121] This decrease in R_{net} was because of an approach to equilibrium, which in turn was due to the greater H_2 partial pressure. The decrease in R_{net} is therefore, due to the thermodynamic reversibility of the reaction. Forward rates (R_{for}) were calculated with Equation 4.1 in order to correctly account for reversibility. The approach to equilibrium, η, was calculated with Equation 4.2 which was derived from the stoichiometric reaction of CH_4 to H_2 and C_6H_6 with the equilibrium constant at 950 K (K_{eq} = 0.0302), as shown in Equation 4.3. Equation 4.1 suggests as the H_2 pressure increases, R_{net} will decrease accordingly, which is observed experimentally.[121] While η and R_{net} account for thermodynamic effects, R_{for} accounts for kinetic changes in C_6H_6 synthesis. The production of H_2 along the reaction bed and the resulting change in thermodynamic driving force for reaction must be accounted for to calculate R_{for}. Equation 4.4 was used to calculate the R_{for} values presented; the derivation of the calculation procedure for determining R_{for} was discussed previously.[121] The integral term in the denominator is used to correctly account for changes in η for discrete sections of the bed, between x and Δx. The terms in the numerator represent the average R_{net} between the same discrete sections of the bed used in the denominator and the Δx term compensates for the dx present in the integral.

$$R_{net} = R_{for} * (1-\eta) \tag{4.1}$$

$$\eta = \frac{P_{C_6H_6}^{1/6} * P_{H_2}^{3/2}}{P_{CH_4} * K_{eq}} \tag{4.2}$$

$$CH_4 \overset{K_{eq}}{\rightleftharpoons} \frac{3}{2} H_2 + \frac{1}{6} C_6H_6 \tag{4.3}$$

$$R_{for}(x) = \frac{\overline{R}_{net} * \Delta x}{\int_x^{x+\Delta x} [1-\eta(x)]dx} \tag{4.4}$$

As discussed in the introduction, prior results by Lacheen and co-workers implied co-processing of H_2 or CO_2 did affect the R_{for} of benzene synthesis.[59] Our results provide an alternative model to the interpretation described by Lacheen and Iglesia, and the work presented here extends our claims and concludes that the co-processing of CH_4/AA, CH_4/FA, and CH_4/CO_2 mixtures has no effect on the R_{for} of benzene formation, rather it only shifts thermodynamic equilibrium.

4.3.2 Steady state dehydroaromatization of CH_4 on Mo/H-ZSM-5 with acetic acid co-feed

The introduction of AA to the CH_4 feed caused a significant decrease (~85%) in the R_{net} of benzene formation (Figure 3.7 of chapter 3). Complete conversion of AA to CO and H_2 was observed at AA/CH_4 = 0.1 and 1.0 g of Mo/H-ZSM-5. Removal of AA from the reactant stream caused complete regeneration of the benzene formation rate suggesting no irreversible catalyst deactivation. In X-ray photoelectron spectroscopic experiments, Rosynek et al. observed the disappearance of bands corresponding to Mo_2C (binding energy = 228 eV) and the appearance of bands corresponding to oxidized Mo (binding energy = 233 and 229.5 eV for Mo^{6+} and Mo^{4+} respectively) after exposure of a carburized Mo/ZSM-5 catalyst to CO_2.[51] Based on these observations, the authors concluded that CO_2 caused re-oxidation of the Mo centers of the Mo/ZSM-5 catalyst. In Raman spectroscopic experiments, Li et al. observed the appearance of bands at 960 cm^{-1} corresponding to Mo=O stretching modes upon introduction of O_2 to a carburized Mo/ZSM-5 catalyst.[119] The intensity of these bands grew with increasing O_2 to CH_4 ratio leading the authors to conclude that with increasing O_2/CH_4, MoC_x gradually reoxidized. The oxidation of MoC_x and associated decrease in the number of active sites is consistent with the significant decrease in aromatic formation rates upon introduction of AA. The amount of catalyst made unavailable for C_6H_6 synthesis was determined through AA breakthrough experiments; this procedure for breakthrough of the oxygenate was adapted from our previous work and is described in Section 3.3.[121] The R_{net} is adjusted for the amount catalyst made unavailable by AA and R_{for} is calculated using Equation 4.4. The results show, once the production of H_2 and oxidation of the catalyst are correctly accounted for, an invariant R_{for} is obtained with respect to catalyst weight and AA to CH_4 feed ratio (see Figure 4.8).

4.3.3 Steady state dehydroaromatization of CH_4 on Mo/H-ZSM-5 with formic acid or carbon dioxide co-feed

Formic acid (FA/CH_4 = 0.01-0.03) and carbon dioxide (CO_2/CH_4 = 0.01-0.03) were individually co-processed with methane on Mo/H-ZSM-5 catalysts at 950 K to determine the kinetic and thermodynamic consequences of co-feeding oxygenates. Similar to reactions with CH_4, CH_4/H_2, and CH_4/AA, C_6H_6 and H_2 partial pressures monotonically increased while CH_4 partial pressures decreased with increasing catalyst loading as shown in Figure 4.2 for CH_4/FA and Figure 4.3 for CH_4/CO_2 experiments. In both co-feed experiments, CH_4 and C_6H_6 pressure systematically decreased while H_2 pressure systematically increased with increasing oxygenate to CH_4 ratio. R_{net} decreased with catalyst loading in all experiments corresponding to the increase in H_2 pressure which caused η to increase. Oxygenate breakthrough experiments at various catalyst loadings and corresponding oxygenate to CH_4 ratios were used to correct for the amount of catalyst unavailable for CH_4 DHA. Inlet oxygenate to CH_4 ratios were increased until CO_2 was observed in the reactor effluent, as shown in Figure 4.4 for a CO_2/CH_4 breakthrough experiment. The final oxygenate to CH_4 ratio was regarded as the ratio needed to deem the corresponding catalyst weight unavailable for CH_4 DHA. Independent experiments were conducted for multiple weights between 25 and 400 mg while co-feeding CO_2 or FA. These results are presented in Figure 4.5 along with the experimental results for CH_4/AA breakthrough for comparison. An oxygenate with a lower carbon to oxygen ratio is predicted to affect a larger amount of catalyst as the mechanism for this inhibition is consumption of CH_4 through reforming reactions, as shown in Equations 4.5-4.7.[59,121] The lack of CH_4 in the vicinity of the Mo/H-ZSM-5 catalyst allows O* to oxidize some MoC_x to MoO_x and MoC_xO_y.[120] Any CH_4 available in this environment would act to carburize the catalyst back to MoC_x before producing ethylene which would subsequently be converted to benzene. This is indeed observed, as shown in Figure 4.5, with CO_2 and FA (C/O = 0.5) deeming more catalyst unavailable for C_6H_6 synthesis than AA (C/O = 1.0).

$$CH_3CO_2H \rightarrow 2CO + 2H_2 \tag{4.5}$$

$$HCO_2H + CH_4 \rightarrow 2CO + 3H_2 \tag{4.6}$$

$$CO_2 + CH_4 \rightarrow 2CO + 2H_2 \tag{4.7}$$

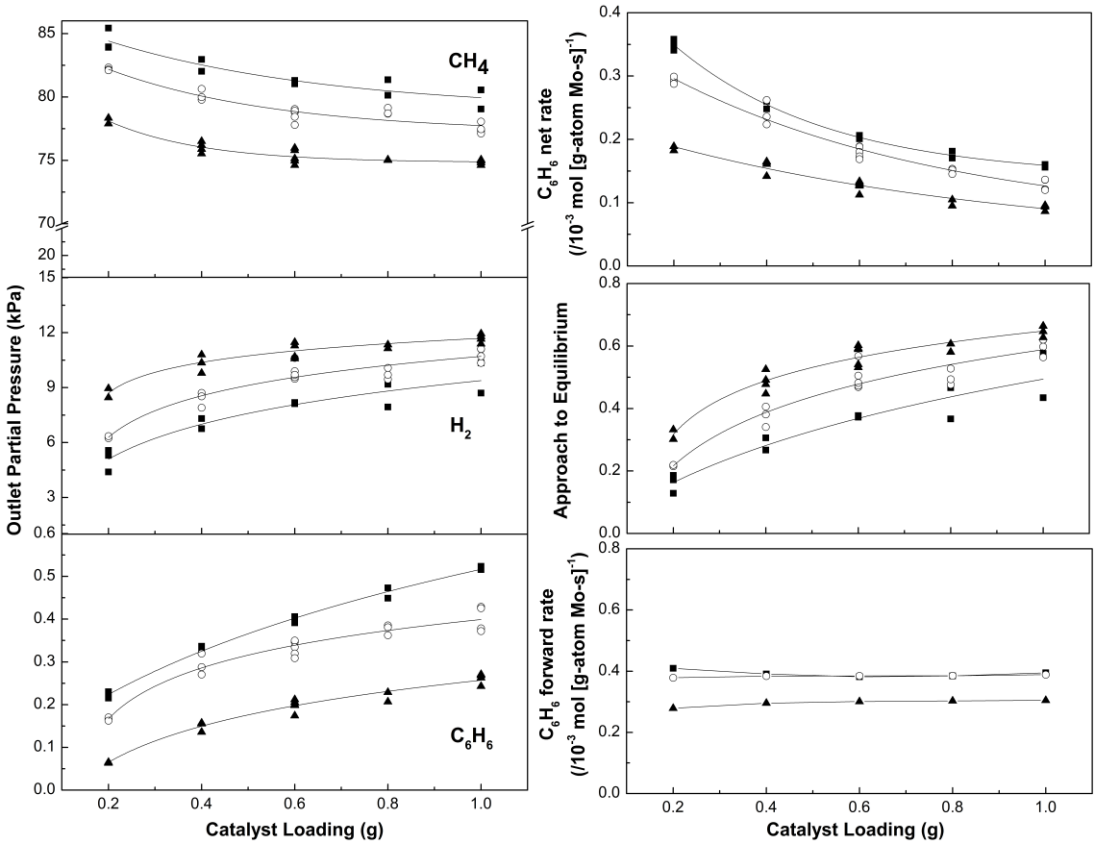

Figure 4.2 CH_4, H_2, and C_6H_6 outlet partial pressure and R_{net}, η, and R_{for} as a function of catalyst loading at 950 K, CH_4 flow rate 12.0 $cm^3\,min^{-1}$, 1 atm, CH_4:Ar = 9:1, and catalyst weight 0.2-1.0 g with Mo:Al_f = 0.25. Inlet FA/CH_4 = 0.01 (■), 0.02 (○), and 0.03 (▲).

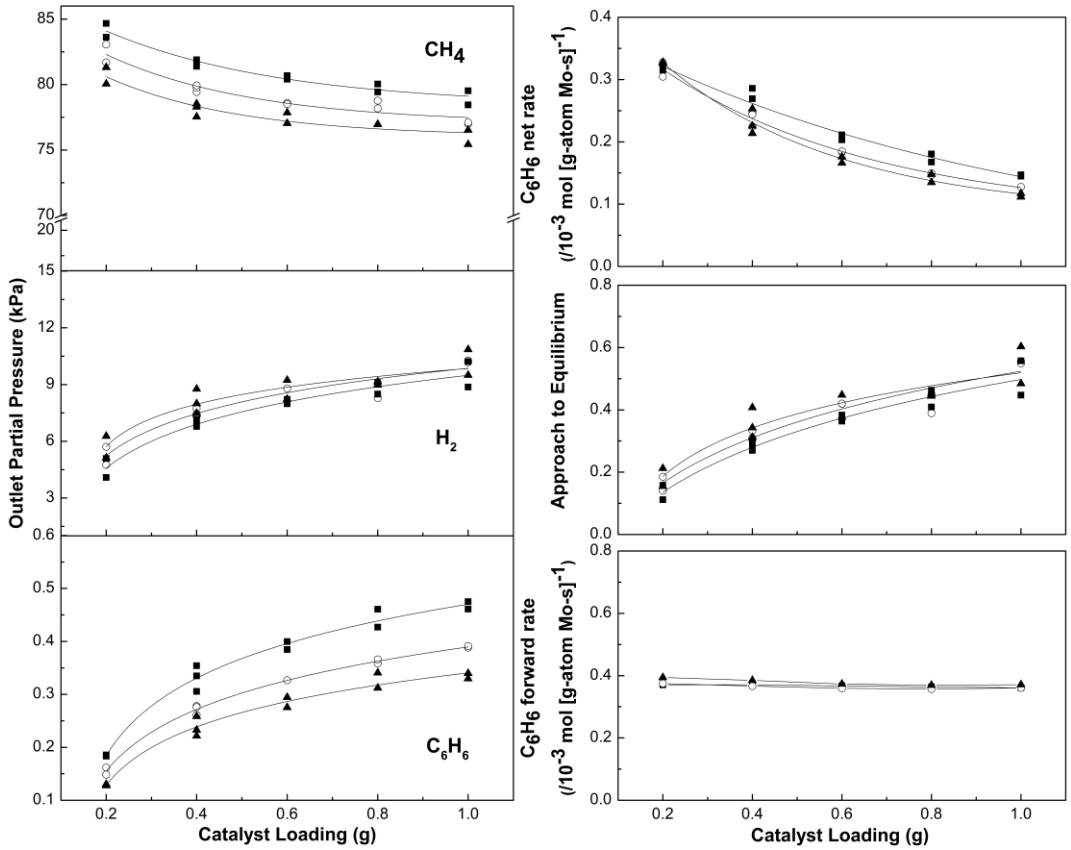

Figure 4.3 CH_4, H_2, and C_6H_6 outlet partial pressure and R_{net}, η, and R_{for} as a function of catalyst loading at 950 K, CH_4 flow rate 12.0 $cm^3\,min^{-1}$, 1 atm, CH_4:Ar = 9:1, and catalyst weight 0.2-1.0 g with Mo:Al_f = 0.25. Inlet CO_2/CH_4 = 0.01 (■), 0.02 (○), and 0.03 (▲).

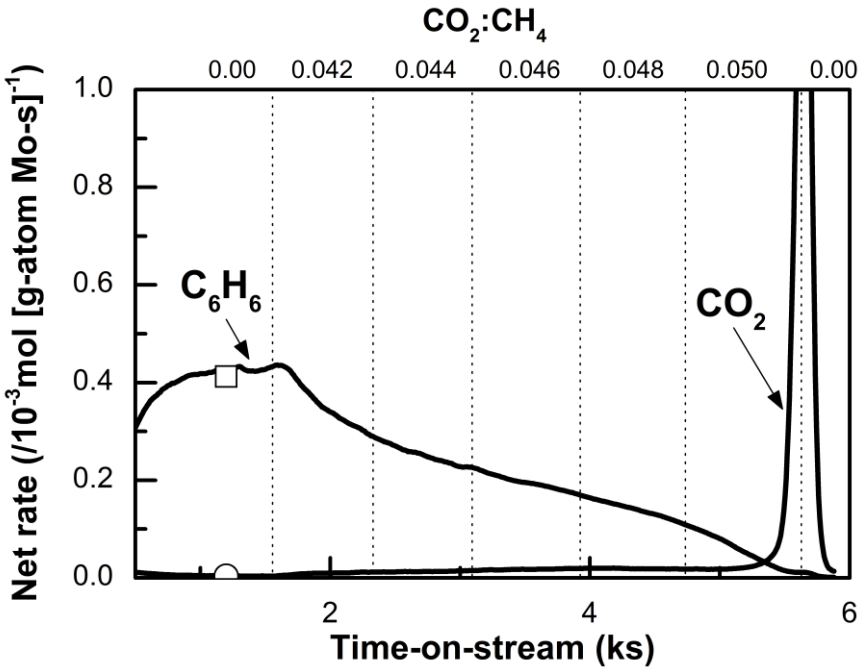

Figure 4.4 C_6H_6 (□) and CO_2 (○) net formation rates at 950 K, CH_4 flow rate 12.0 $cm^3\,min^{-1}$, 1 atm, CH_4:Ar = 9:1, catalyst loading 200 mg with Mo:Al_f = 0.25. Inlet CO_2/CH_4 ratio = 0.00, 0.042, 0.044, 0.046, 0.048, 0.050, and 0.00. Symbols are GC data and solid lines are MS transient data.

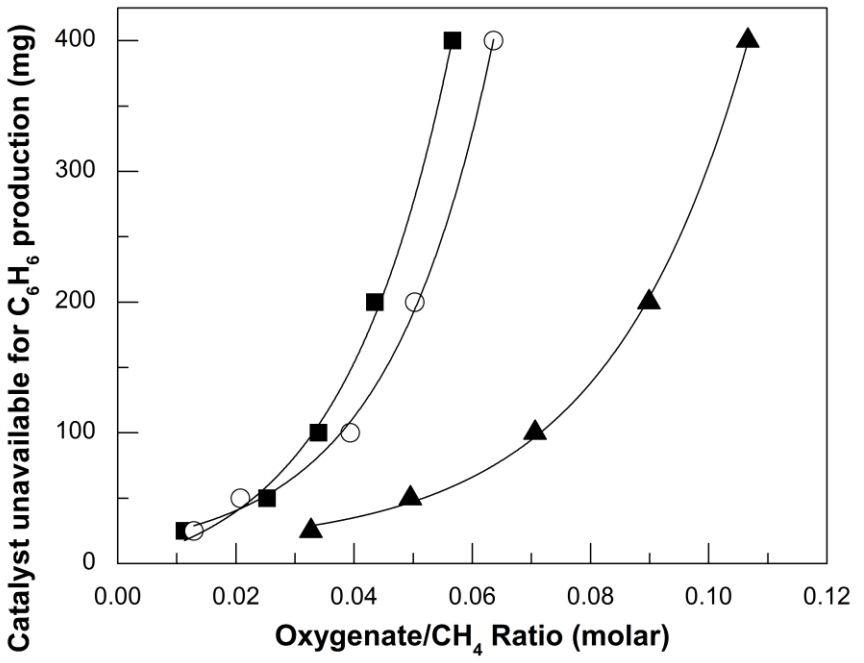

Figure 4.5 Amount of catalyst unable to produce C_6H_6 due to the presence of AA (▲), FA (■), and CO_2 (○) as a function of oxygenate to CH_4 ratio.

The data in Figure 4.5 was fit to an exponential function ($y = y_o + A*\exp[B*x]$) for each oxygenate. The parameters were then used to back calculate the amount of catalyst unavailable for C_6H_6 synthesis for each pertaining oxygenate to CH_4 ratio. R_{net} was subsequently normalized by the amount of Mo active for CH_4 DHA. R_{for} at specific catalyst loadings is then calculated from this adjusted R_{net} and η, which is calculated with product and reactant partial pressures measured at the outlet of the reactor. R_{for} values for CH_4/FA and CH_4/CO_2 co-processing experiments are shown in Figures 4.2 and 4.3 respectively. The average R_{for} for CH_4/FA experiments is $0.36 \pm 0.02 \times 10^{-3}$ mol/(g-atom Mo-s) with inlet $FA/CH_4 = 0.01$-0.03 and catalyst loadings = 0.2-1.0 g while the average R_{for} for CH_4/ CO_2 experiments is $0.37 \pm 0.02 \times 10^{-3}$ mol/(g-atom Mo-s) with inlet $CO_2/CH_4 = 0.01$-0.03 and the same catalyst loadings. These values are consistent with previously determined R_{for} values of CH_4 ($0.47 \pm 0.08 \times 10^{-3}$), CH_4/H_2 ($0.38 \pm 0.05 \times 10^{-3}$), and CH_4/AA ($0.45 \pm 0.05 \times 10^{-3}$) processing experiments.[121] R_{for} is invariant irrespective of catalyst loading, oxygenate identity, and oxygenate to CH_4 ratio within our ability to measure these values at the employed reaction conditions as shown in Figures 4.2 and 4.3 as well as Table 4.1.

Yao et al. report the incorporation of ^{13}C in benzene products in $^{13}CO/CH_4$ co-feed experiments on Mo/MCM-49 catalyst formulations.[122] The authors also claim a promotional effect of CO, however, this report contradicts prior results

Table 4.1 Forward rate of benzene synthesis at different FA/CH_4, CO_2/CH_4, AA/CH_4, and H_2/CH_4 inlet ratios. Reaction conditions: Temperature, 950 K; CH_4 flow rate, 12.0 $cm^3\,min^{-1}$, 1 atm, CH_4:Ar = 9:1; catalyst loading, 0.1-1.0 g; $Mo/Al_f = 0.25$.

FA/CH_4	0.0	0.01	0.02	0.03	
R_{for} ($\frac{10^{-3}\text{mol}}{\text{g-atom Mo-s}}$)	0.47 ± 0.08	0.39 ± 0.03	0.38 ± 0.02	0.30 ± 0.01	
CO_2/CH_4	0.0	0.01	0.02	0.03	
R_{for} ($\frac{10^{-3}\text{mol}}{\text{g-atom Mo-s}}$)	0.47 ± 0.08	0.37 ± 0.02	0.36 ± 0.02	0.38 ± 0.03	
AA/CH_4	0.0	0.02	0.03	0.04	0.05
R_{for} ($\frac{10^{-3}\text{mol}}{\text{g-atom Mo-s}}$)	0.47 ± 0.08	0.50 ± 0.04	0.48 ± 0.08	0.39 ± 0.02	0.43 ± 0.02
H_2/CH_4	0.0	0.03	0.06	0.08	0.11
R_{for} ($\frac{10^{-3}\text{mol}}{\text{g-atom Mo-s}}$)	0.47 ± 0.08	0.39 ± 0.05	0.41 ± 0.07	0.34 ± 0.05	0.38 ± 0.02

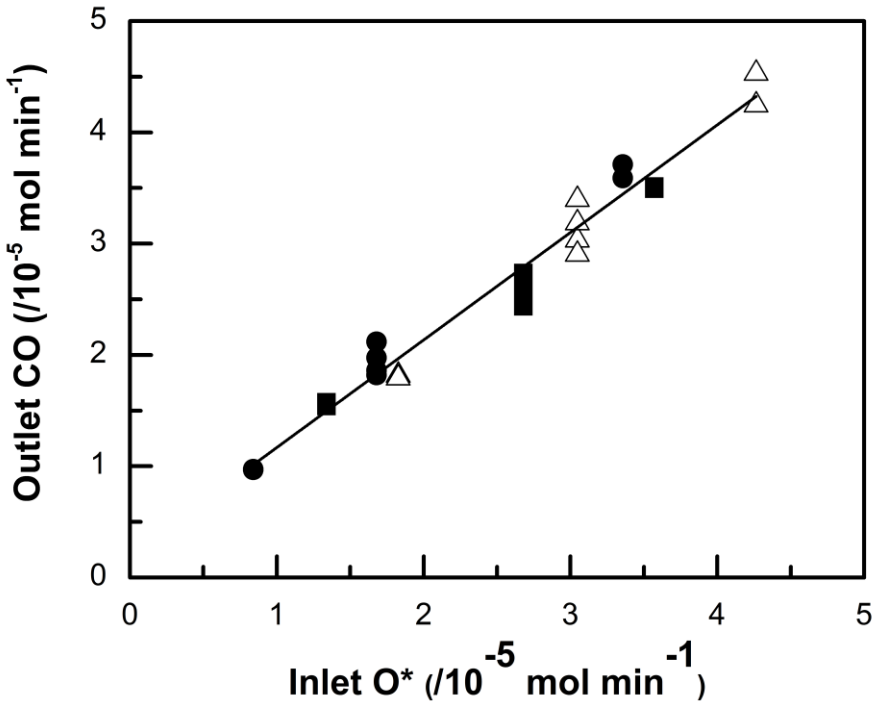

Figure 4.6 Outlet CO flow rates as a function of inlet oxygenate flow rates. CO_2 (■), acetic acid (△), and formic acid (●).

reported by Liu and Iglesia where the authors observe no kinetic consequences of CO addition on CH_4 conversion and hydrocarbon formation rates on Mo/ZSM-5 formulations.[60] In independent experiments with CO_2, HCOOH, and CH_3COOH co-feeds we observe that oxygen is stoichiometrically removed as CO irrespective of the concentration or identity of the oxygenate, as shown in Figure 4.6, and that no change in forward rates is observed at these varying CO concentrations in the effluent. We postulate the incorporation of ^{13}C in benzene observed in $^{13}CO/CH_4$ co-feed experiments reported by Yao et al. represents an exchange reaction and is kinetically inconsequential.[122]

These results show that adding oxygenates at successively higher oxygenate to CH_4 ratios do not kinetically affect the rate determining step of CH_4 pyrolysis on Mo/H-ZSM-5 catalysts; rather the oxygenates fragment on such ssurfaces and are reformed with CH_4 to CO and H_2 as shown in Figure 4.7. The production of H_2 upstream in oxygenate reforming reactions only serves to shift the equilibrium of CH_4 to C_6H_6. The average R_{for} for CH_4/FA, CH_4/CO_2, CH_4/AA, CH_4/H_2, and CH_4 DHA reactions as a function of catalyst weight is shown in Figure 4.8. The average R_{for} considering all reactions and co-feeds is $0.40 \pm 0.05 \times 10^{-3}$ mol/(g-atom Mo-s).

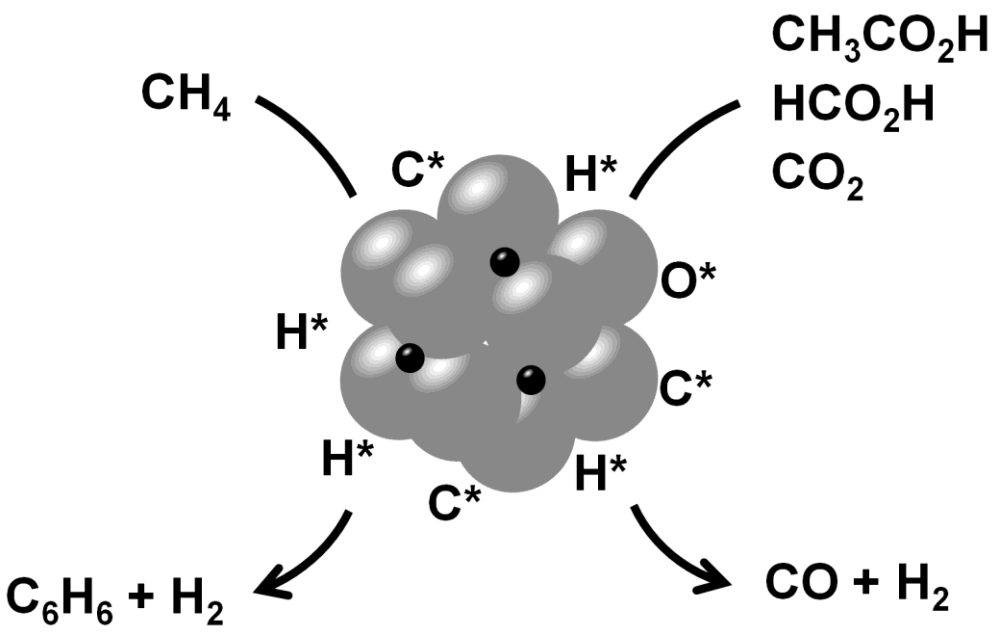

Figure 4.7 Representation of CH_4 pyrolysis and oxygenate reforming on Mo/H-ZSM-5 surfaces

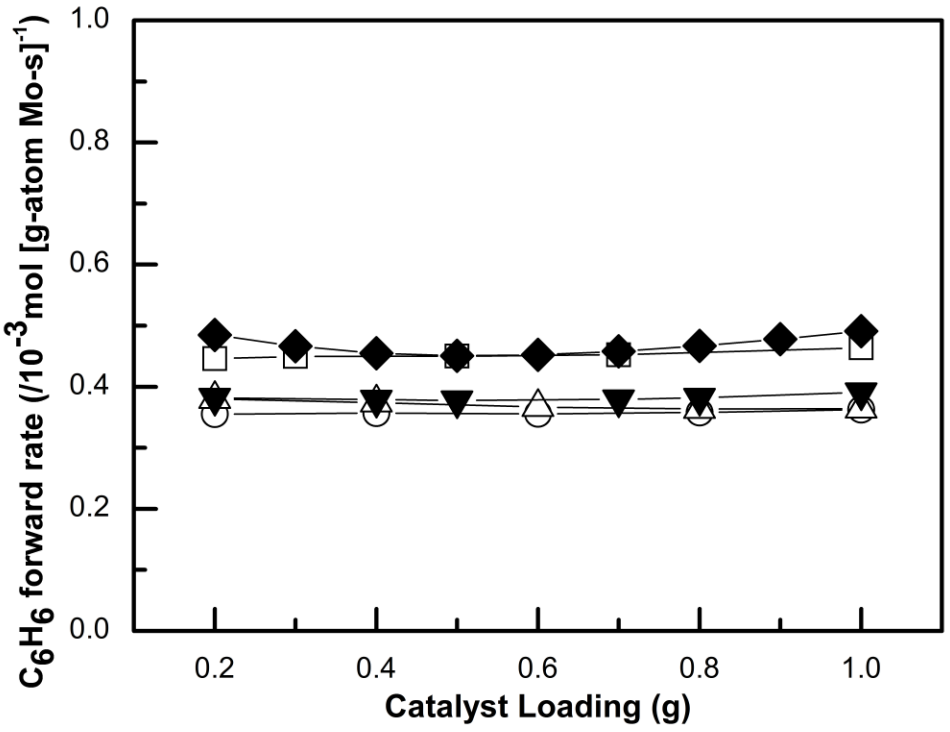

Figure 4.8 Average forward rate of C_6H_6 production as a function of catalyst loading at 950 K, CH_4 flow rate 12.0 $cm^3\,min^{-1}$, 1 atm, CH_4:Ar = 9:1, and catalyst weight 0.2-1.0 g with Mo:Al_f = 0.25. FA/CH_4 (○), CO_2/CH_4 (△), AA/CH_4 (□), H_2/CH_4 (▼), and CH_4 (◆).

Our investigations into the co-processing of oxygenates and CH_4 during DHA reactions show that the addition of oxygenates has no kinetic consequences and can be rigorously described by oxygenate reforming and downstream CH_4 DHA in an environment that includes CO and H_2 produced in the first stage. The understanding of how multi-functional catalysts simultaneously achieve deoxygenation and dehydrogenation is crucially dependent on our ability to distinguish between the kinetic and thermodynamic effects of oxygenate co-processing.

4.4 Conclusions

Co-processing of acetic acid, formic acid, or carbon dioxide with methane on Mo/H-ZSM-5 during steady-state catalytic reactions at 950 K was investigated to determine the kinetic and thermodynamic consequences of co-feeding oxygenates. CH_4 dehydroaromatization is governed by thermodynamic equilibrium such that an increase in the oxygenate to CH_4 ratio causes the net rate of benzene synthesis to decrease. No kinetic coupling of CH_4 dehydrogenation and oxygenate s is observed; rather the oxygenate completely fragments and is reformed with CH_4 to CO and H_2 upstream until completely consumed. CH_4 DHA occurs downstream from the oxygenate reforming zone in an environment that includes CO and H_2 previously produced. Co-processing oxygenates with CH_4 causes an increase in the H_2 to CH_4 ratio which acts to push equilibrium towards the reactants but does not affect the forward rate of C_6H_6 synthesis.

4.5 Supplemental information

The tabulated results presented in Table 4.2 show the observed product distribution and conversion for co-processing CO_2/CH_4, CH_3COOH/CH_4, and $HCOOH/CH_4$ mixtures at 950 K. All data reported were recorded at 11 ks time-on stream.

Table 4.2 CH_4 conversion and product carbon selectivity for DHA reactions over Mo/H-ZSM-5 catalyst at 950 K, CH_4 flow rate 12.0 $cm^3\,min^{-1}$, CH_4:Ar = 9:1, catalyst loading 1 g with Mo:Al_f = 0.25, and time-on-stream 11 ks.

Oxygenate	CO_2	AA	FA
O^*/CH_4 ($/10^{-5}$)	1.8	1.5	1.7
CH_4 conversion (%)[a]	8.6	6.3	8.2
Selectivity (%)[b]			
CO	62.0	54.1	41.2
C_2H_4	1.0	1.3	1.5
C_2H_6	1.1	1.2	1.6
C_6H_6	22.6	29.5	36.7
C_7H_8	1.0	1.4	1.7
$C_{10}H_8$	11.1	11.6	15.6
C_{10}^+	1.2	0.9	1.5

[a] $Conv_{CH_4} = \frac{F_{CH_4}^{Inlet} - F_{CH_4}^{Outlet}}{F_{CH_4}^{Inlet}}$ [b] $\%S_i = \frac{n_i * F_i}{\sum_i n_i * F_i}$

CHAPTER

FIVE

C TO H EFFECTIVE RATIO AS A DESCRIPTOR FOR CO-PROCESSING LIGHT OXYGENATES AND CH_4 ON Mo/H-ZSM-5

5.1 Introduction

Natural gas and biomass represent non-conventional hydrocarbon feedstocks that ultimately require either dehydrogenation or deoxygenation for the synthesis of commodity chemicals and fuels.[7,12] Biomass and methane lie on opposite ends of the chemical spectrum, as characterized by the effective hydrogen index (EHI) introduced by Chen *et al.* (Equation 5.1, Figure 5.1).[21] Methane dehydroaromatization (DHA) on Mo/H-ZSM-5 catalysts represents a direct, non-oxidative route for CH_4 activation to produce aromatics and hydrogen at greater than 70% benzene selectivity with 8-10% CH_4 conversion at ~950 K.[50–52,54,82,85,89,110,121,123–125] Co-processing biomass-derived compounds with CH_4 would enable the synthesis of fuels with a greater degree of saturation compared to those produced from biomass alone. Previously, we reported that forward rates of C_6H_6 synthesis are unperturbed by co-processing CH_4 with H_2, CO_2, or $C_{1\text{-}2}$ carboxylic acids while creating a stratified bed configuration consisting of upstream oxygenate reforming and downstream CH_4 pyrolysis;[121,125] here we present the effective carbon to hydrogen ratio (C/H_{eff}) as a single value descriptor for the effect of co-processing
light oxygenates of varying functionality with CH_4 on the net rate of benzene and total hydrocarbon production.

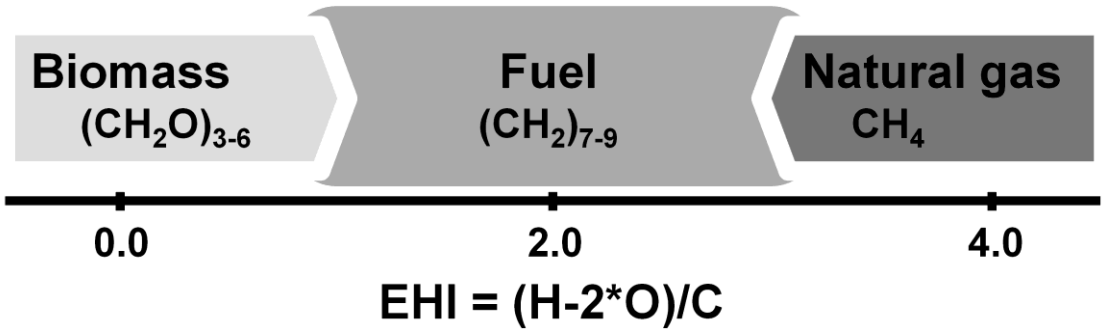

Figure 5.1 Effective hydrogen content of biomass, crude oil, and natural gas.

$$EHI = \frac{H - 2*O - 3*N - 2*S}{C} \tag{5.1}$$

5.2 Materials and methods

Catalyst synthesis and reaction procedures were consistent with a previously published study and are summarized here.[121] Mo/H-ZSM-5 catalyst was prepared via solid state ion exchange starting with MoO_3 powder (Sigma-Aldrich, 99.9%) and commercially available NH_4-ZSM-5 zeolite (Zeolyst International, CBV 2314, Si/Al = 11.7). [121] Steady-state catalytic reactions of CH_4/CO_2, CH_4/H_2O, CH_4/H_2, and CH_4/C_{1-2} oxygenates (Sigma-Aldrich, 99%) were conducted at 950 K and atmospheric pressure with 1.0 g of synthesized Mo/H-ZSM-5 catalyst within a fixed bed, tubular quartz reactor (10 mm inner diameter). Water (H_2O), acetic acid (AcOH), formic acid (FrOH), methanol (MeOH), ethanol (EtOH), or acetaldehyde (AcH) co-feeds were introduced via liquid infusion pump (KD Scientific) while H_2 or CO_2 (UHP, Matheson Tri-Gas) co-feeds were introduced via mass-flow controller (Brooks) with a flowing stream of CH_4/Ar (90% CH_4 and 10% Ar, 0.223 $cm^3\ s^{-1}$ corresponding to CH_4 space velocity of 722 $cm^3\ g_{cat}^{-1}\ h^{-1}$, UHP, Matheson Tri-Gas) to the catalyst after complete carburization and a steady benzene synthesis rate was observed (10.8 ks for 1.0 g catalyst; $R_{net} = 0.2 \times 10^{-3}$ mol C_6H_6 [g-atom Mo s]$^{-1}$). ^{13}C-labelled acetic acid ($^{13}C_2$-AA, Sigma-Aldrich, 99%) was used in carbon tracking experiments. Reactor effluent was analysed with a gas chromatograph (Agilent 7890) and a mass spectrometer (MKS Cirrus 200) connected in series with the GC samples loops (transient analysis) or connected at the outlet of the TCD (tandem analysis). Isotopologue distributions were determined from mass fragmentation patterns using a procedure adapted from Price and Iglesia.[126]

5.3 Results and discussion

Oxygenates have previously been co-processed with CH_4 to reduce deactivation due to carbon deposition.[59,97,119] O_2 and CO_2 co-feeds resulted in the production of CO as the sole oxygen-containing product, through reforming reactions with CH_4 or via reverse Boudouard reactions.[59,97,119] Co-feeds of acetic acid or formic acid also produced CO in a stoichiometric ratio ($O^*_n \rightarrow n$CO).[125] These results clearly demonstrate O removal via CO production pathways rather than CO_2 or H_2O as terminal O^* products as any CO_2 or H_2O that is formed *in situ* is converted to CO, which agrees with thermodynamic equilibrium calculations at these temperatures (HSC 7.1, Figure 5.4). Independent CO_2 or H_2O co-feed experiments also verify this conclusion (see Figure 5.5, 5.6, and Figure 4.6 of chapter 4). The EHI characterizes heteroatom containing hydrocarbons based on the amount of hydrogen necessary to remove those heteroatoms as hydrogen oxide, nitride, or sulfide (Equation 5.1).[21] This relationship however, is invalid for the chemistry at hand because all O is eliminated as CO. The C to H effective ratio (C/H_{eff}) instead expresses O removal as CO as pertinent in DHA reactions with oxygenate co-feeds (Equation 5.2).

$$C / H_{eff} = \frac{C - O}{H} \tag{5.2}$$

The C/H_{eff} is an overall measure of the amount of C, H, and O in a certain feed and represents the ratio of C to H after O elimination. A linear relationship between the net rate of benzene synthesis (R_{net}) and the C/H_{eff} is observed irrespective of the identity or concentration ($O^*/CH_4 \leq 0.1$) of the oxygenate co-feed as shown in Figure 5.2; H_2/CH_4 mixtures also fall on this line. This signifies that the production of benzene is governed by the inlet composition, as represented by C/H_{eff}. R_{net} increases with increasing C/H_{eff} as more C is available, or less H, to produce C_6H_6 which has a C/H_{eff} equal to 1.0. Different oxygenate co-feeds irrespective of their functionality will only affect R_{net} based on their empirical formulas. The molar oxygenate to CH_4 ratio (O^*/CH_4) also affects C/H_{eff}, and in turn R_{net}. A composite C/H_{eff} of the feed is expressed in Equation 5.3 which accounts for the CH_4 present. This relationship also holds for the total hydrocarbon net synthesis rate (Figure 5.7). The observed selectivity to C_6H_6

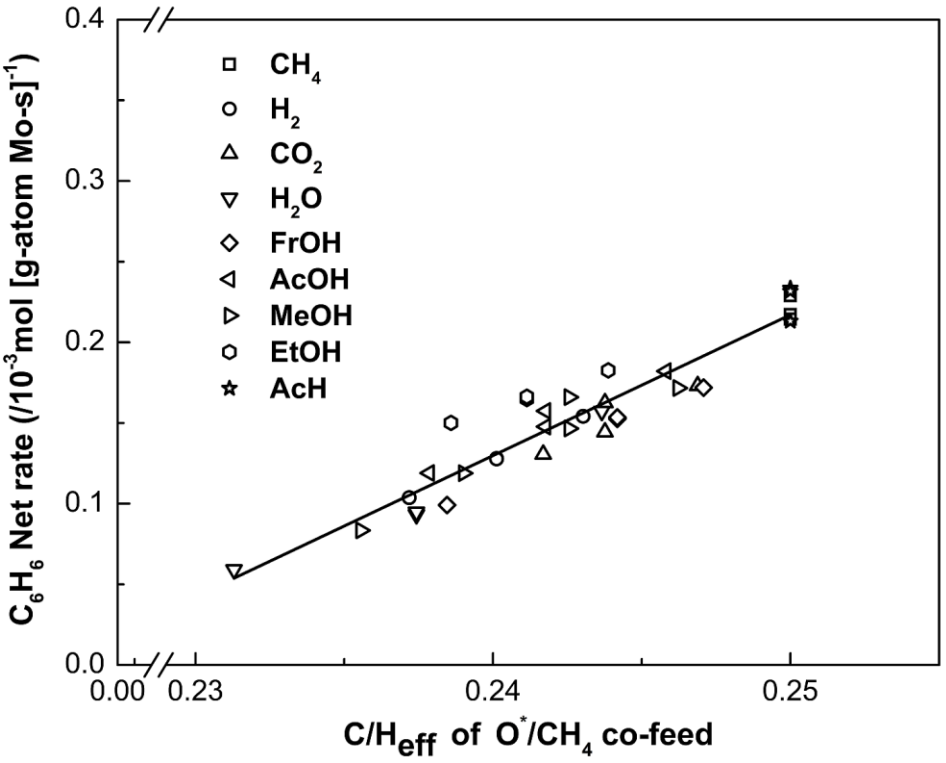

Figure 5.2 R_{net} as a function of C/H_{eff} at 950 K, CH_4 flow rate 12.0 cm^3 min^{-1}, CH_4/Ar = 9:1, catalyst weight 1.0 g with Mo/Al_f =0.25, and H_2/CH_4 = 0.057-0.108, CO_2/CH_4 = 0.012-0.033, H_2O/CH_4 = 0.017-0.051, $FrOH/CH_4$ = 0.008-0.031, $AcOH/CH_4$ = 0.017-0.051, $MeOH/CH_4$ = 0.015-0.061, $EtOH/CH_4$ = 0.053-0.106, or AcH/CH_4 = 0.055-0.110.

$$C/H_{eff,feed} = \frac{C_{CH_4} + (C_{O^*} - O_{O^*}) * \frac{O^*}{CH_4}}{H_{CH_4} + H_{O^*} * \frac{O^*}{CH_4}} \tag{5.3}$$

(71± 2%), C_2H_4 (2.5 ± 0.5%), and $C_{10}H_8$ (19 ±2%) was invariant across all co-feeds and C/H_{eff} (Table 5.1).

The concept of C/H_{eff} governing the net rate of benzene production relies on chemical functionality independence; specific chemical bonds and molecular structure do not matter, instead only the empirical formula of the relevant co-feed. This chemical aspecificity requires total fragmentation of co-feeds into activated C, H, and O species which react with CH_4 to produce CO, H_2 and C_6H_6. Isotopic tracer experiments were conducted in which the experimental distribution of ^{13}C in C_6H_6 was compared to a theoretically calculated binomial distribution based on the inlet ^{13}C concentration to confirm total fragmentation

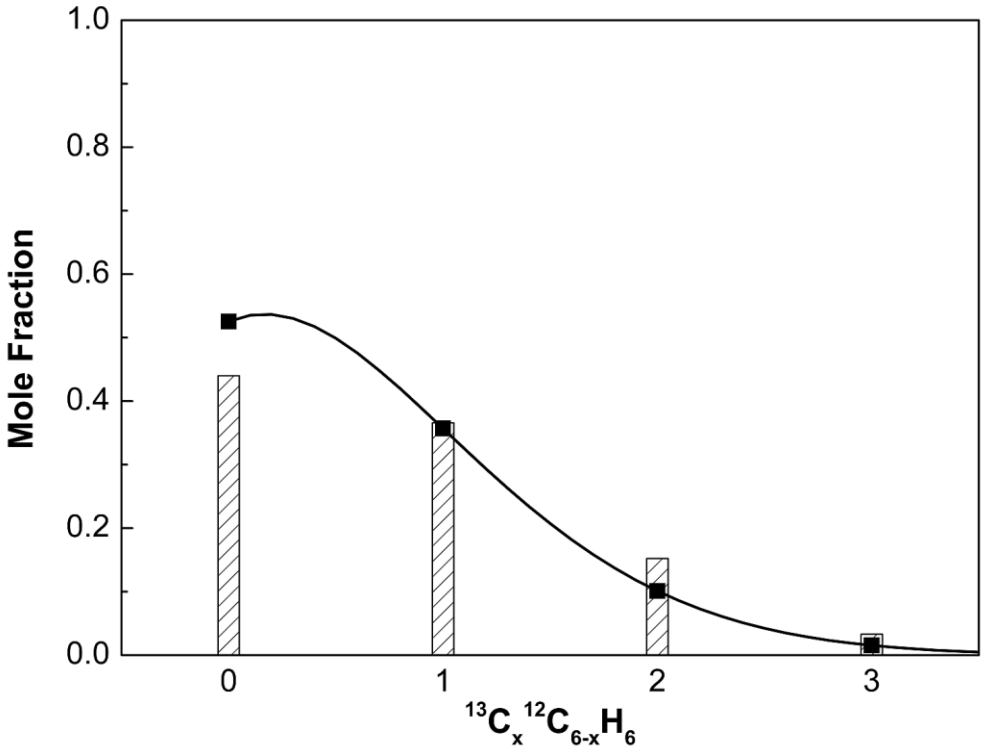

Figure 5.3 Experimental (bars) and theoretical (points) mole fractions for ^{13}C-labeled C_6H_6 produced at 950 K, CH_4 flow rate 12.0 cm^3 min $^{-1}$, CH_4/Ar = 9:1, catalyst weight 1.0 g with Mo/Al$_f$ =0.25, and $^{13}C_2$-AcOH/CH_4 = 0.051 for a feed ^{13}C concentration of 10.2%. Line represents estimation of binomial distribution at non-integer values using the gamma function.

of the oxygenate. The good agreement between experimental and statistically predicted isotopic compositions of C_6H_6 (binomial distribution) in Figure 5.3 when co-processing CH_4 with natural abundance of ^{13}C (1.1%) and ^{13}C-labelled AcOH verifies that total fragmentation of the acetic acid molecule occurs under reaction conditions.

5.4 Conclusions

The C/H$_{eff}$ is a single value descriptor for predicting the net rate of benzene and total hydrocarbon synthesis from CH_4 dehydroaromatization reactions at 950 K while co-feeding C_{1-2} oxygenates with acid, hydroxyl, and carbonyl functionalities which results in CO as the sole oxygen-containing product.

5.5 Supplemental information

Figure 5.4 depicts thermodynamic equilibrium amounts of hydrocarbons and oxygenates with a starting composition of 1 kmol CH_4 and 0.1 kmol CH_3COOH as a function of temperature (273 – 1073 K).

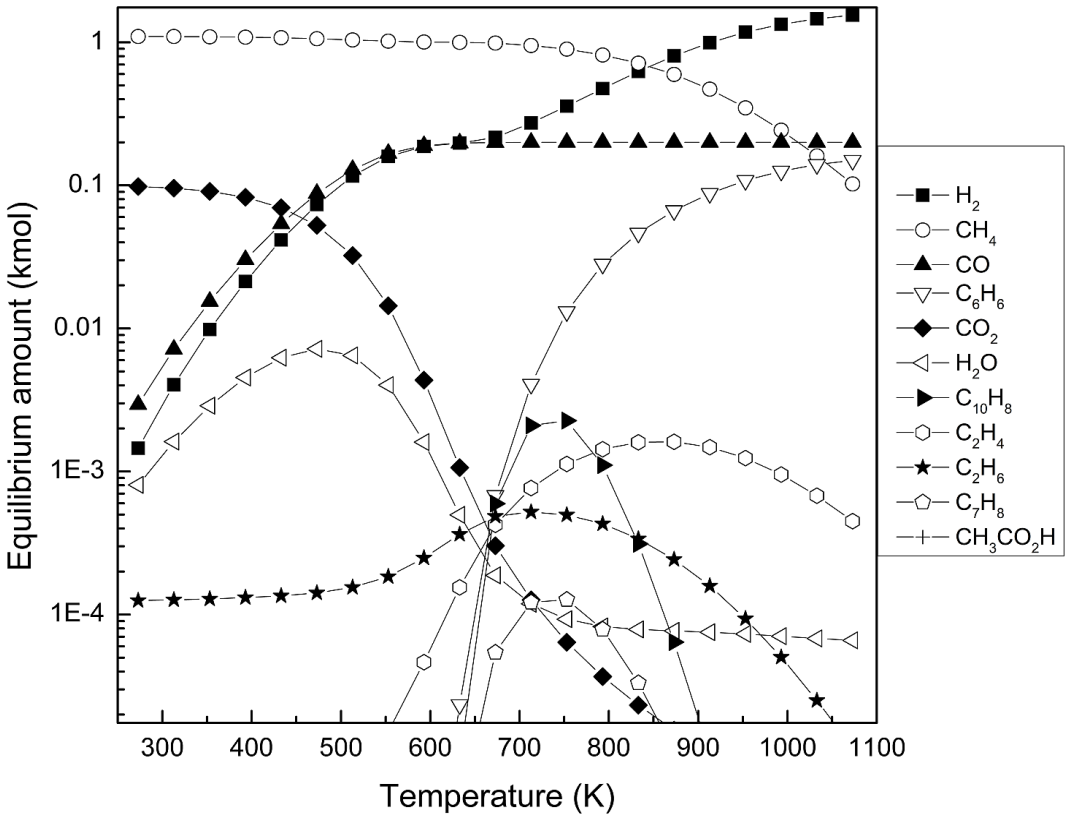

Figure 5.4 Equilibrium amounts of hydrocarbons and oxygenates as a function of temperature starting as CH_4 (1 kmol) and CH_3COOH (0.1 kmol).

Figures 5.5a and 5.5b depict CO production as the sole oxygen-containing product when processing H_2O/CH_4 at various ratios. CO_2 and H_2O mass spectrometric signals are 1-2 orders of magnitude lower than that for CO.

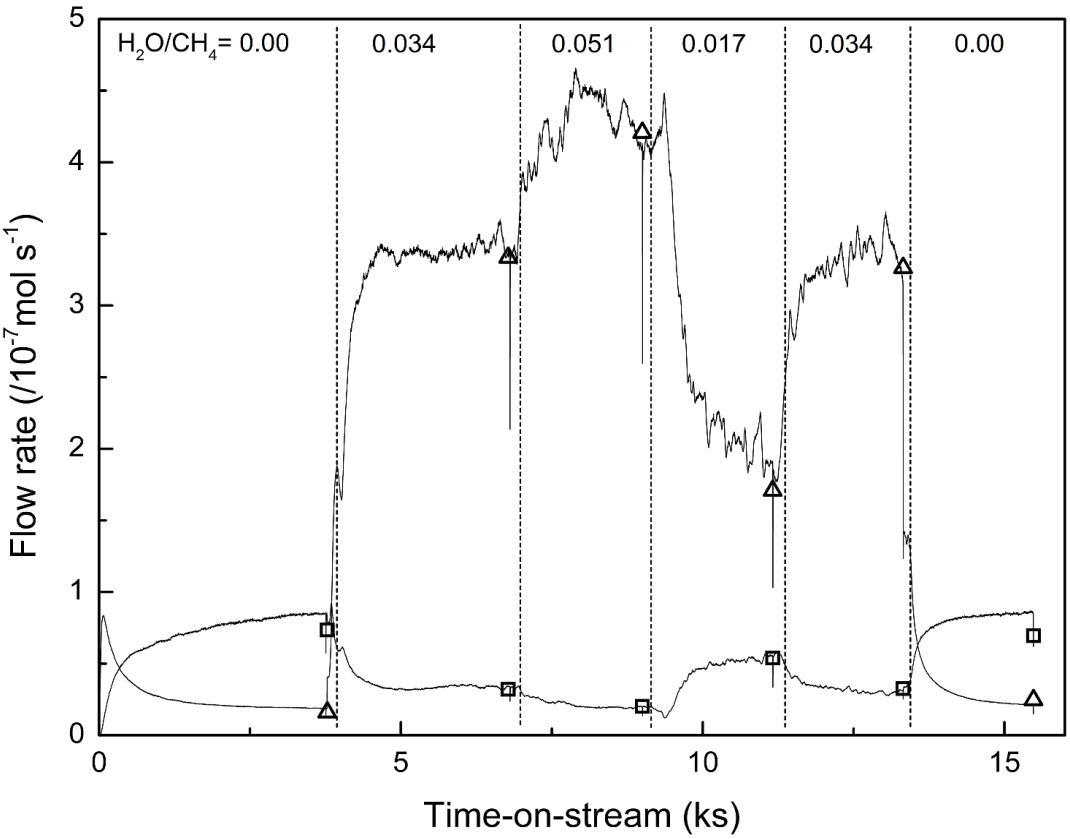

Figure 5.5a C_6H_6 (□) and CO (△) molar flow rates at 950 K, CH_4 flow rate 12.0 cm^3 min^{-1}, CH_4:Ar = 9:1, catalyst loading 1000 mg with Mo:Al_f = 0.25. Inlet H_2O/CH_4 ratio = 0.00, 0.034, 0.051, 0.017, 0.034, and 0.00. Symbols are GC data and solid lines are MS transient data.

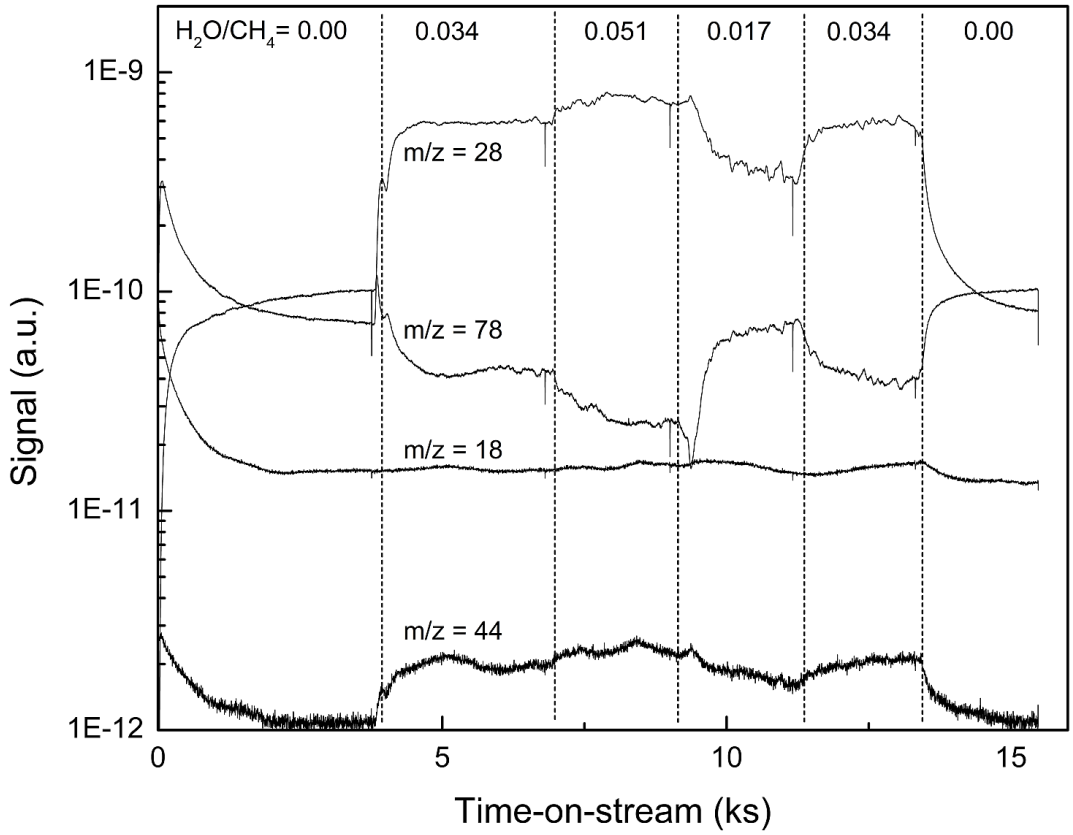

Figure 5.5b CO (28), C_6H_6 (78), H_2O (18), and CO_2 (44) mass spectrometry signals at 950 K, CH_4 flow rate 12.0 $cm^3\ min^{-1}$, CH_4:Ar = 9:1, catalyst loading 1000 mg with Mo:Al_f = 0.25. Inlet H_2O/CH_4 ratio = 0.00, 0.034, 0.051, 0.017, 0.034, and 0.00.

Figure 5.6 depicts the outlet CO flow rate at various H_2O inlet flow rates.

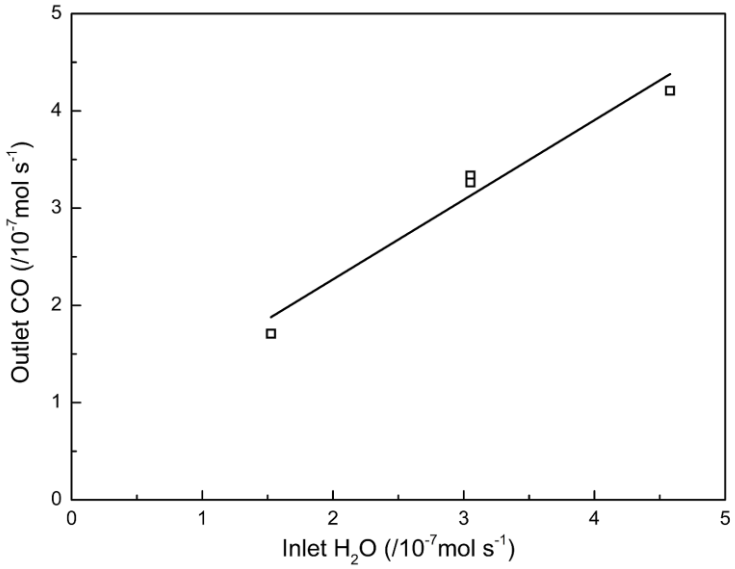

Figure 5.6 Outlet CO flow rate as a function of inlet H_2O flow rate.

Figure 5.7 depicts total hydrocarbon (sum of C_2H_4, C_2H_6, C_6H_6, C_7H_8, and $C_{10}H_8$) net synthesis rate as a function of the feed C/H_{eff}. Net rates are calculated based on total catalyst loaded (1.0 g) and not adjusted for Mo oxidation.

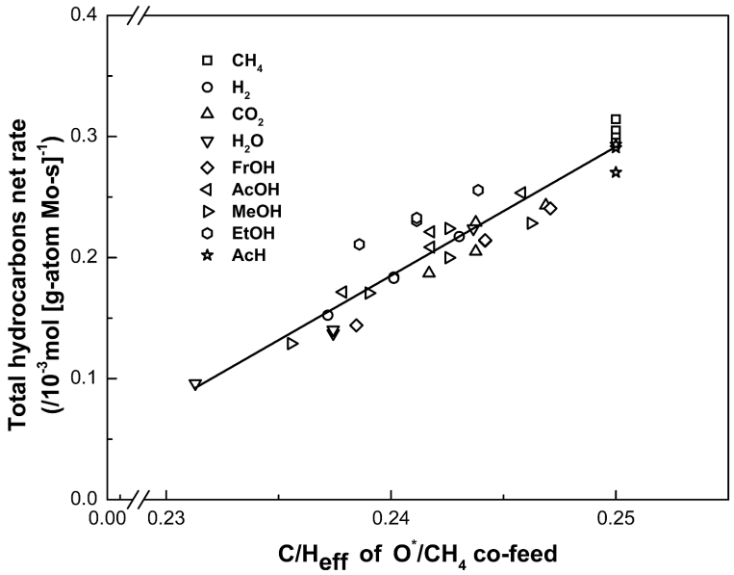

Figure 5.7 Total hydrocarbon net synthesis rate as a function of C/H_{eff} at 950 K, CH_4 flow rate 12.0 cm^3 min $^{-1}$, CH_4/Ar = 9:1, catalyst weight 1.0 g with Mo/Al_f =0.25, and H_2/CH_4 = 0.057-0.108, CO_2/CH_4 = 0.012-0.033, H_2O/CH_4 = 0.017-0.051, $FrOH/CH_4$ = 0.008-0.031, $AcOH/CH_4$ = 0.017-0.051, $MeOH/CH_4$ = 0.015-0.061, $EtOH/CH_4$ = 0.053-0.106, or AcH/CH_4 = 0.055-0.110.

The tabulated results presented in Table 5.1 show the observed product distribution and conversion for co-processing oxygenate/CH_4 mixtures at 950 K.

Table 5.1 CH_4 conversion and hydrocarbon product selectivity for DHA reactions over Mo/H-ZSM-5 catalyst at 950 K, CH_4 flow rate 12.0 cm^3 min^{-1}, CH_4:Ar = 9:1, catalyst loading 1 g with Mo:Al_f = 0.25, and time-on-stream 13 ks.

Co-feed	CH_4	H_2	CO_2	H_2O	FrOH	AcOH
O*/CH_4	-	0.082	0.033	0.034	0.016	0.034
CH_4 conversion (%)[a]	7.3	4.7	6.0	4.4	6.0	4.0
Selectivity (%)[b]						
C_2H_4	2.0	2.7	2.7	2.5	2.2	2.2
C_2H_6	1.8	3.2	2.9	4.1	2.9	2.3
C_6H_6	70.8	71.5	71.2	70.8	71.6	70.7
C_7H_8	3.4	3.2	3.3	3.0	3.4	3.1
$C_{10}H_8$	21.0	18.2	18.5	18.3	17.9	20.5

[a] $Conv_{CH_4} = \frac{F_{CH_4}^{Inlet} - F_{CH_4}^{Outlet}}{F_{CH_4}^{Inlet}}$ [b] $\%S_i = \frac{n_i * F_i}{\sum_i n_i * F_i}$

CHAPTER

SIX

CO-FEEDING $C_{3\text{-}5}$ OXYGENATES AND CH_4 ON Mo/H-ZSM-5

6.1 Introduction

The concept of describing oxygenate co-feeds based on their C to H effective ratio (C/H_{eff}) was introduced in chapter 5. A distinction between small ($C_{1\text{-}2}$) oxygenates with $C/H_{eff} < 0.25$ and larger ($C_{3\text{-}5}$) oxygenates with $C/H_{eff} \geq 0.25$ was observed; incomplete fragmentation of the co-fed oxygenate led to preferential pathways of benzene synthesis. A brief description of the experimental observations and analyses is presented here.

6.2 Materials and methods

The reader is directed to section 2 of chapter 5 for reaction procedures pertinent to the results discussed here. The only changes are the liquid co-feeds (Sigma-Aldrich, 99%) used which include propanoic acid (PrOOH), acrylic acid (ACA), ethyl acetate (EA), propanol (PrOH), acetone (ATN), propionaldehyde (PPL), 2-pentanone (2PTN), and 2-methyl furan (2MF). ^{13}C-labeled acetone ($^{13}C_3$-ATN, Sigma-Aldrich, 99%) was also used in carbon tracking experiments.

6.3 Results and discussion

$C_{3\text{-}5}$ oxygenates were co-fed with CH_4 over Mo/H-ZSM-5 catalysts to verify C/H_{eff} as a single value descriptor for predicting the net benzene synthesis rate

for all oxygenate co-feeds. All oxygen was eliminated as CO (Figure 6.1), consistent with previous studies (chapters 3-5). Figure 6.2 shows the net rate of C_6H_6 synthesis (R_{net}) as a function of the feed C/H_{eff}. C_{1-2} oxygenates as well as H_2 with $C/H_{eff} \leq 0.25$ fall on one line with R_{net} increasing as the feed C/H_{eff} increases. Deviation from this line is observed with C_{3-5} oxygenates. PrOOH, the only C_3 oxygenate with $C/H_{eff} < 0.25$ tested, maintained a constant R_{net} of $0.20 \pm 0.01 \times 10^{-3}$ mol C_6H_6 [g-atom Mo s]$^{-1}$ at varying PrOOH/CH_4 (0.02-0.07). ACA maintained a consistent R_{net} comparable to CH_4 alone (0.20×10^{-3} mol C_6H_6 [g-atom Mo s]$^{-1}$) at varying ACA/CH_4 (0.02-0.07) while EA and PrOH co-feeds, also with $C/H_{eff} = 0.25$, caused an increase in R_{net} at varying O^*/CH_4 (0.03-0.08). ATN, PPL, and 2PTN, each with $C/H_{eff} > 0.25$, caused an increase in R_{net} at varying O^*/CH_4 (0.02-0.23). These co-feeds fall on a congruent line, but with a greater slope (22 vs. 9) than the C_{1-2} oxygenates line. 2MF co-feed caused an increase in R_{net} at varying 2MF/CH_4 (0.03-0.07) and falls on a separate line with a slope of 15. These trends also hold for the total hydrocarbon synthesis rate, as shown in Figure 6.4 of section 6.5. The greater R_{net} and slopes observed with C_{3-5} oxygenates point to preferential pathways of C_6H_6 production unlike those observed for smaller C_{1-2} oxygenates. Such pathways may include alcohol dehydration followed by olefin oligomerization as well as aldol condensation to produce aromatics.[127–129]

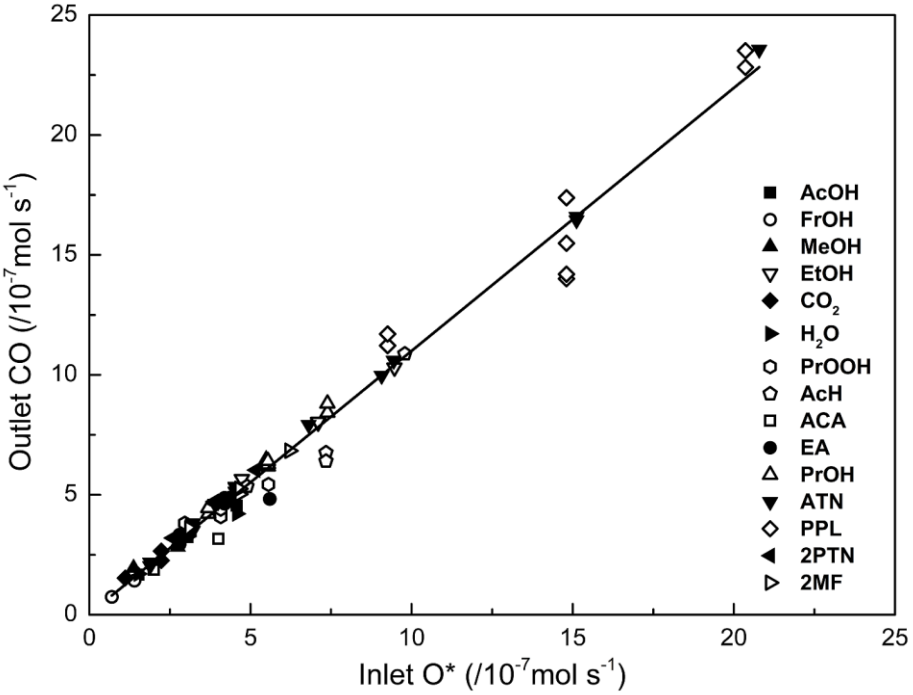

Figure 6.1 Outlet CO flow rate as a function of inlet O^* flow rate.

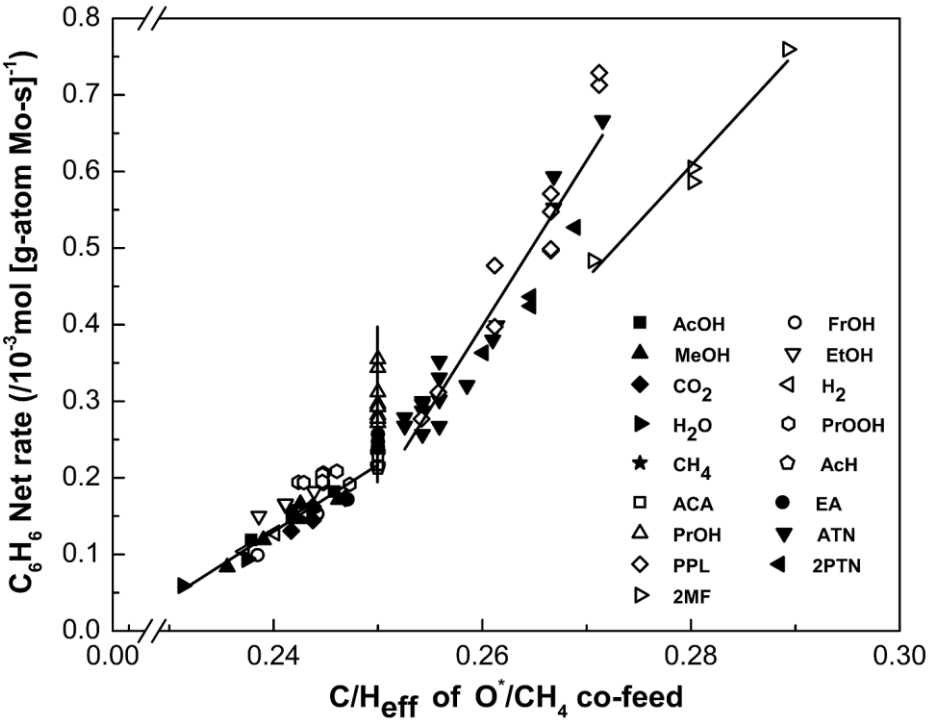

Figure 6.2 R_{net} as a function of C/H_{eff} at 950 K, CH_4 flow rate 12.0 cm^3 min^{-1}, CH_4/Ar = 9:1, catalyst weight 1.0 g with Mo/Al_f =0.25, and H_2/CH_4 = 0.057-0.108, CO_2/CH_4 = 0.012-0.033, H_2O/CH_4 = 0.017-0.051, $FrOH/CH_4$ = 0.008-0.031, $AcOH/CH_4$ = 0.017-0.051, $MeOH/CH_4$ = 0.015-0.061, $EtOH/CH_4$ = 0.053-0.106, AcH/CH_4 = 0.055-0.110, $PrOOH/CH_4$ = 0.022-0.067, ACA/CH_4 = 0.022-0.067, EA/CH_4 = 0.031-0.063, $PrOH/CH_4$ = 0.041-0.083, ATN/CH_4 = 0.021-0.232, PPL/CH_4 = 0.021-0.227, $2PTN/CH_4$ = 0.029-0.058, or $2MF/CH_4$ = 0.035-0.069.

Isotopic tracer experiments were conducted in which the experimental distribution of ^{13}C in produced C_6H_6 was compared to theoretical binomial distributions to determine reaction pathways of acetone to benzene. Figure 6.3 shows a considerable fraction of $^{13}C_{4\text{-}6}$ labeled C_6H_6 in stark contrast to the distribution predicted from the inlet ^{13}C concentration (binomial distribution). These results verify incomplete fragmentation of the ATN parent molecule with direct formation of C_6H_6 from the oxygenate without CH_4 incorporation. Table 6.1 shows theoretical distributions of ^{13}C in C_6H_6 produced from three different sources of hydrocarbon: ^{13}C-ATN only, CH_4 only, and a mix of ^{13}C-ATN and CH_4. The error between the experimental and ^{13}C-ATN/CH_4 mix distributions is lower compared to that predicted when considering ^{13}C-ATN or CH_4 as the only source of hydrocarbon, however, the ^{13}C-ATN/CH_4 mix model greatly underestimates

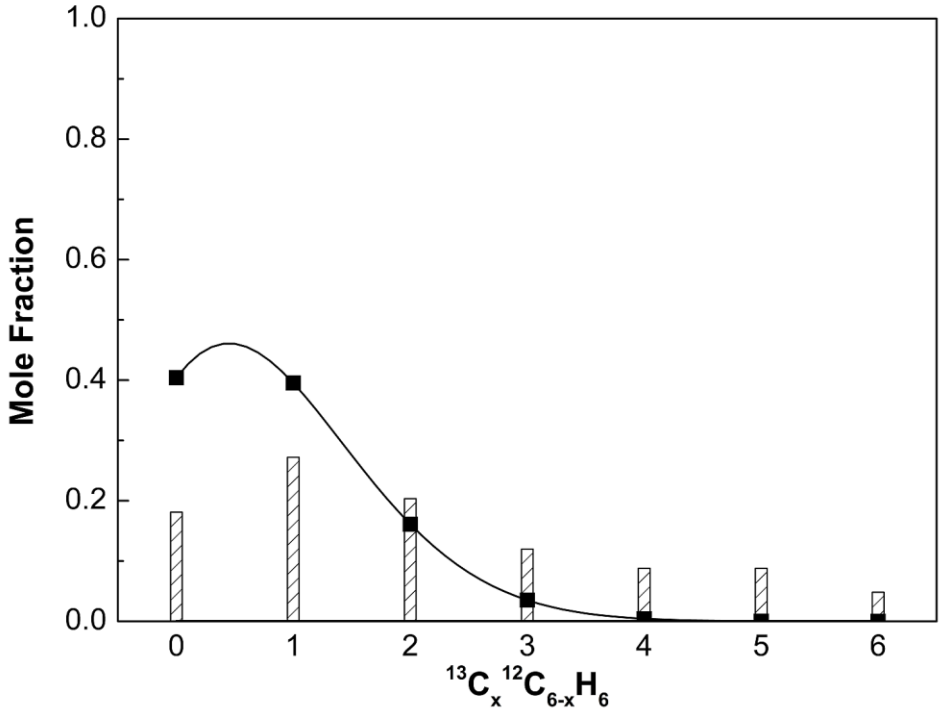

Figure 6.3 Experimental (bars) and theoretical (points) mole fractions for ^{13}C-labeled C_6H_6 produced at 950 K, CH_4 flow rate 12.0 cm^3 min^{-1}, CH_4/Ar = 9:1, catalyst weight 1.0 g with Mo/Al$_f$ =0.25, and $^{13}C_3$-ATN/CH_4 = 0.051 for a feed ^{13}C concentration of 14.0%. The line shown represents estimation of the binomial distribution at non-integer values using the gamma function.

the amount of $C_{4\text{-}6}$ labeled C_6H_6. Linear combinations of these models can not precisely estimate the ^{13}C distribution either, as no combination was found to match the mole fractions experimentally observed for $^{13}C_{2\text{-}5}$ labeled C_6H_6. It is postulated that C_6H_6 is produced from all three sources of hydrocarbon, but the extent of production from each individual source is unknown. It may be a function of the oxygenate co-feed, oxygenate to CH_4 ratio, CH_4 conversion, approach to equilibrium, and other factors.

Table 6.1 Theoretical and experimental mole fractions for ^{13}C-labeled C_6H_6. Theoretical values are based on a binomial distribution of ^{13}C at each corresponding concentration (^{13}C-ATN = 99%, CH_4 = 1.1%, and ^{13}C-ATN/CH_4 = 14%).

$13C_x$	^{13}C-ATN only	CH_4 only	^{13}C-ATN/CH_4 mix	Experimental
0	1.0E-12	0.94	0.40	0.18
1	5.9E-10	0.06	0.40	0.27
2	1.5E-07	1.7E-03	0.16	0.20
3	1.9E-05	2.6E-05	0.04	0.12
4	1.4E-03	2.1E-07	4.3E-03	0.09
5	0.06	9.6E-10	2.8E-04	0.09
6	0.94	1.8E-12	7.6E-06	0.05

6.4 Conclusions

Co-feeding $C_{3\text{-}5}$ oxygenates with CH_4 results in a greater C_6H_6 R_{net} than would be predicted based on the observations made when co-processing $C_{1\text{-}2}$ oxygenates and CH_4 (described in chapter 5). R_{net} observed with $C_{3\text{-}5}$ oxygenates increases linearly with C/H_{eff}, but at a distinct slope than observed with $C_{1\text{-}2}$ oxygenates. It is postulated from ^{13}C-ATN/CH_4 isotopic tracking experiments that incomplete fragmentation of the co-feed oxygenate occurs, leading to preferential pathways of C_6H_6 production including dehydration, olefin oligomerization, and aldol condensation that exclude CH_4 incorporation.

6.5 Supplemental information

Figure 6.4 depicts total hydrocarbon (sum of C_2H_4, C_2H_6, C_6H_6, C_7H_8, and $C_{10}H_8$) net synthesis rate as a function of the feed C/H_{eff}. Net rates are calculated based on total catalyst loaded (1.0 g) and not adjusted for Mo oxidation.

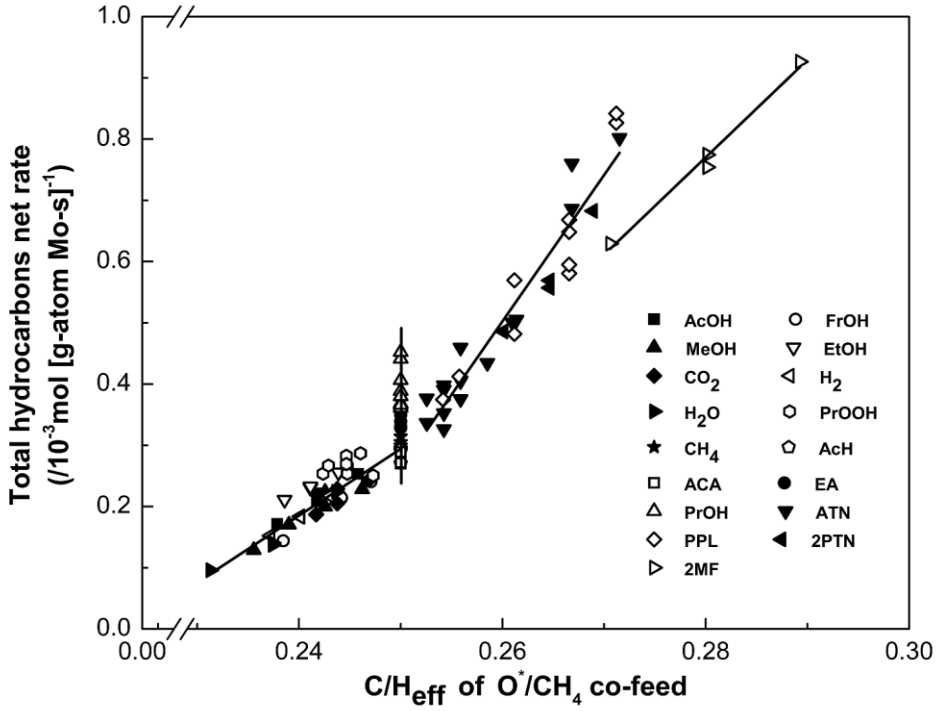

Figure 6.4 Total hydrocarbon net synthesis rate as a function of C/H_{eff} at 950 K, CH_4 flow rate 12.0 cm^3 min^{-1}, CH_4/Ar = 9:1, catalyst weight 1.0 g with Mo/Al_f =0.25, and H_2/CH_4 = 0.057-0.108, CO_2/CH_4 = 0.012-0.033, H_2O/CH_4 = 0.017-0.051, $FrOH/CH_4$ = 0.008-0.031, $AcOH/CH_4$ = 0.017-0.051, $MeOH/CH_4$ = 0.015-0.061, $EtOH/CH_4$ = 0.053-0.106, AcH/CH_4 = 0.055-0.110, $PrOOH/CH_4$ = 0.022-0.067, ACA/CH_4 = 0.022-0.067, EA/CH_4 = 0.031-0.063, $PrOH/CH_4$ = 0.041-0.083, ATN/CH_4 = 0.021-0.232, PPL/CH_4 = 0.021-0.227, $2PTN/CH_4$ = 0.029-0.058, or $2MF/CH_4$ = 0.035-0.069.

BIBLIOGRAPHY

[1] G.M. Whitesides, G.W. Crabtree, Don't forget long-term fundamental research in energy., Science. 315 (2007) 796–8. doi:10.1126/science.1140362.

[2] R.E. Smalley, Future Global Energy Prosperity: The Terawatt Challenge, MRS Bull. 30 (2011) 412–417. doi:10.1557/mrs2005.124.

[3] C. Schubert, Can biofuels finally take center stage?, Nat. Biotechnol. 24 (2006) 777–84. doi:10.1038/nbt0706-777.

[4] M.I. Hoffert, K. Caldeira, G. Benford, D.R. Criswell, C. Green, H. Herzog, et al., Advanced technology paths to global climate stability: energy for a greenhouse planet., Science. 298 (2002) 981–7. doi:10.1126/science.1072357.

[5] N.S. Lewis, Toward cost-effective solar energy use., Science. 315 (2007) 798–801. doi:10.1126/science.1137014.

[6] R. Agrawal, N.R. Singh, F.H. Ribeiro, W.N. Delgass, Sustainable fuel for the transportation sector., Proc. Natl. Acad. Sci. U. S. A. 104 (2007) 4828–33. doi:10.1073/pnas.0609921104.

[7] G.W. Huber, S. Iborra, A. Corma, Synthesis of transportation fuels from biomass: chemistry, catalysts, and engineering., Chem. Rev. 106 (2006) 4044–4098. doi:10.1021/cr068360d.

[8] A. Corma, S. Iborra, A. Velty, Chemical routes for the transformation of biomass into chemicals., Chem. Rev. 107 (2007) 2411–502. doi:10.1021/cr050989d.

[9] S. Czernik, A. V. Bridgwater, Overview of Applications of Biomass Fast Pyrolysis Oil, Energy & Fuels. 18 (2004) 590–598. doi:10.1021/ef034067u.

[10] A. Oasmaa, S. Czernik, Fuel Oil Quality of Biomass Pyrolysis Oils-State of the Art for the End Users, Energy & Fuels. 13 (1999) 914–921. doi:10.1021/ef980272b.

[11] L. Petrus, M.A. Noordermeer, Biomass to biofuels, a chemical perspective, Green Chem. 8 (2006) 861. doi:10.1039/b605036k.

[12] A. Caballero, P.J. Pérez, Methane as raw material in synthetic chemistry: the final frontier., Chem. Soc. Rev. 42 (2013) 8809–20. doi:10.1039/c3cs60120j.

[13] T. Choudhary, E. Aksoylu, D. Wayne Goodman, Nonoxidative Activation of Methane, Cataly. Rev. 45 (2003) 151–203. doi:10.1081/CR-120017010.

[14] E. Sousa-Aguiar, L. Appel, C. Mota, Natural gas chemical transformations: The path to refining in the future, Catal. Today. 101 (2005) 3–7. doi:10.1016/j.cattod.2004.12.003.

[15] G. Busca, Acid catalysts in industrial hydrocarbon chemistry., Chem. Rev. 107 (2007) 5366–410. doi:10.1021/cr068042e.

[16] A. Bhan, W.N. Delgass, Propane Aromatization over HZSM-5 and Ga/HZSM-5 Catalysts, Catal. Rev. 50 (2008) 19–151. doi:10.1080/01614940701804745.

[17] V. a. Blatov, G.D. Ilyushin, D.M. Proserpio, The Zeolite Conundrum: Why Are There so Many Hypothetical Zeolites and so Few Observed? A Possible Answer from the Zeolite-Type Frameworks Perceived As Packings of Tiles, Chem Mater. 25 (2013) 412–424. doi:10.1021/cm303528u.

[18] W.M. Meier, D.H. Olson, C. Baerlocher, Atlas of zeolite structure types, Zeolites. 17 (1996) 1–230. doi:10.1016/S0144-2449(96)80004-2.

[19] C. Baerlocher, L.B. McCusker, Database of Zeolite Structures, http://www.iza-structure.org/databases/ (accessed February 05, 2011).

[20] Zeolyst International, http://zeolyst.com/ (accessed February 05, 2011).

[21] N.Y. Chen, T.F. Degnan, L.R. Koenig, Liquid fuel from carbohydrates, Chemtech. 16 (1986) 11.

[22] T.R. Carlson, G.A. Tompsett, W.C. Conner, G.W. Huber, Aromatic Production from Catalytic Fast Pyrolysis of Biomass-Derived Feedstocks, Top. Catal. 52 (2009) 241–252. doi:10.1007/s11244-008-9160-6.

[23] T.R. Carlson, T.P. Vispute, G.W. Huber, Green gasoline by catalytic fast pyrolysis of solid biomass derived compounds., ChemSusChem. 1 (2008) 397–400. doi:10.1002/cssc.200800018.

[24] E. Fischer, A. Speier, Darstellung der Ester, Berichte Der Dtsch. Chem. Gesellschaft. 28 (1895) 3252–3258. doi:10.1002/cber.189502803176.

[25] I. Roberts, H.C. Urey, A study of the esterification of benzoic acid with methyl alcohol using isotopic oxygen, J. Am. Chem. Soc. 60 (1938) 2391–2393. doi:10.1021/ja01277a028.

[26] P. Dutia, Ethyl Acetate: A Techno-Commercial Profile, Chem. Weekly-Bombay. 49 (2004) 179–186.

[27] A.A. Kulkarni, K.-P. Zeyer, T. Jacobs, A. Kienle, Miniaturized Systems for Homogeneously and Heterogeneously Catalyzed Liquid-Phase Esterification Reaction, Ind. Eng. Chem. Res. 46 (2007) 5271–5277. doi:10.1021/ie060411+.

[28] K. Wilson, J.H. Clark, Solid acids and their use as environmentally friendly catalysts in organic synthesis, Pure Appl. Chem. 72 (2000) 1313–1319. doi:10.1351/pac200072071313.

[29] Y. Liu, E. Lotero, J.G. Goodwin, A comparison of the esterification of acetic acid with methanol using heterogeneous versus homogeneous acid catalysis, J. Catal. 242 (2006) 278–286. doi:10.1016/j.jcat.2006.05.026.

[30] X. Yao, J. Yao, L. Zhang, N. Xu, Fast Esterification of Acetic Acid with Short Chain Alcohols in Microchannel Reactor, Catal. Lett. 132 (2009) 147–152. doi:10.1007/s10562-009-0072-2.

[31] K. Suwannakarn, E. Lotero, J.G. Goodwin, A comparative study of gas phase esterification on solid acid catalysts, Catal. Lett. 114 (2007) 122–128. doi:10.1007/s10562-007-9054-4.

[32] K. Suwannakarn, E. Lotero, J.G. Goodwin, Solid Brønsted Acid Catalysis in the Gas-Phase Esterification of Acetic Acid, Ind. Eng. Chem. Res. 46 (2007) 7050–7056. doi:10.1021/ie070536u.

[33] S. Miao, B.H. Shanks, Esterification of biomass pyrolysis model acids over sulfonic acid-functionalized mesoporous silicas, Appl. Catal. A. 359 (2009) 113–120. doi:10.1016/j.apcata.2009.02.029.

[34] R. Koster, B. van Der Linden, E. Poels, A. Bliek, The Mechanism of the Gas-Phase Esterification of Acetic Acid and Ethanol over MCM-41, J. Catal. 204 (2001) 333–338. doi:10.1006/jcat.2001.3356.

[35] T. Peters, N. Benes, A. Holmen, J. Keurentjes, Comparison of commercial solid acid catalysts for the esterification of acetic acid with butanol, Appl. Catal. A. 297 (2006) 182–188. doi:10.1016/j.apcata.2005.09.006.

[36] D.E. López, K. Suwannakarn, J.G. Goodwin, D.A. Bruce, Reaction Kinetics and Mechanism for the Gas- and Liquid-Phase Esterification of Acetic Acid with Methanol on Tungstated Zirconia, Ind. Eng. Chem. Res. 47 (2008) 2221–2230. doi:10.1021/ie070665a.

[37] W. Chu, X. Yang, X. Ye, Y. Wu, Vapor phase esterification catalyzed by immobilized dodecatungstosilicic acid (SiW12) on activated carbon, Appl. Catal. A. 145 (1996) 125–140. doi:10.1016/0926-860X(96)00109-3.

[38] G.D. Yadav, P.H. Mehta, Heterogeneous Catalysis in Esterification Reactions: Preparation of Phenethyl Acetate and Cyclohexyl Acetate by Using a Variety of Solid Acidic Catalysts, Ind. Eng. Chem. Res. 33 (1994) 2198–2208. doi:10.1021/ie00033a025.

[39] O.D. La Iglesia, R. Mallada, M. Menendez, J. Coronas, Continuous zeolite membrane reactor for esterification of ethanol and acetic acid, Chem. Eng. J. 131 (2007) 35–39. doi:10.1016/j.cej.2006.12.015.

[40] K. Tanaka, R. Yoshikawa, C. Ying, H. Kita, K.-I. Okamoto, Application of Zeolite Membranes to Esterification Reactions, Chem. Ing. Tech. 73 (2001) 768–768. doi:10.1002/1522-2640(200106)73:6<768::AID-CITE7683333>3.0.CO;2-L.

[41] S. Kirumakki, N. Nagaraju, S. Narayanan, A comparative esterification of benzyl alcohol with acetic acid over zeolites Hβ, HY and HZSM5, Appl. Catal. A. 273 (2004) 1–9. doi:10.1016/j.apcata.2004.03.016.

[42] S. Kirumakki, N. Nagaraju, K. Chary, Esterification of alcohols with acetic acid over zeolites Hβ, HY and HZSM5, Appl. Catal. A. 299 (2006) 185–192. doi:10.1016/j.apcata.2005.10.033.

[43] M.P. Bernal, J. Coronas, M. Menendez, J. Santamaria, Coupling of reaction and separation at the microscopic level: esterification processes in a H-ZSM-5 membrane reactor, Chem. Eng. Sci. 57 (2002) 1557–1562. doi:10.1016/S0009-2509(02)00030-1.

[44] B. Jermy, A. Pandurangan, Catalytic application of Al-MCM-41 in the esterification of acetic acid with various alcohols, Appl. Catal. A Gen. 288 (2005) 25–33. doi:10.1016/j.apcata.2005.03.047.

[45] H.T.R. Teo, B. Saha, Heterogeneous catalysed esterification of acetic acid with isoamyl alcohol: kinetic studies, J. Catal. 228 (2004) 174–182. doi:10.1016/j.jcat.2004.08.018.

[46] M.-J. Lee, H.-T. Wu, H.-M. Lin, Kinetics of Catalytic Esterification of Acetic Acid and Amyl Alcohol over Dowex, Ind. Eng. Chem. Res. 39 (2000) 4094–4099. doi:10.1021/ie0000764.

[47] T. Nijhuis, A.E.W. Beers, F. Kapteijn, J.A. Moulijn, Water removal by reactive stripping for a solid-acid catalyzed esterification in a monolithic reactor, Chem. Eng. Sci. 57 (2002) 1627–1632. doi:10.1016/S0009-2509(02)00039-8.

[48] M.R. Altiokka, A. Citak, Kinetics study of esterification of acetic acid with isobutanol in the presence of amberlite catalyst, Appl. Catal. A. 239 (2003) 141–148. doi:10.1016/S0926-860X(02)00381-2.

[49] M.E. Davis, R.J. Davis, Fundamentals of Chemical Reaction Engineering, McGraw-Hill, 2003.

[50] L. Wang, L. Tao, M. Xie, G. Xu, J. Huang, Y. Xu, Dehydrogenation and aromatization of methane under non-oxidizing conditions, Catal. Lett. 21 (1993) 35–41. doi:10.1007/BF00767368.

[51] D. Wang, J.H. Lunsford, M.P. Rosynek, Catalytic conversion of methane to benzene over Mo/ZSM-5, Top. Catal. 3 (1996) 289–297. doi:10.1007/BF02113855.

[52] Z.R. Ismagilov, E. V. Matus, L.T. Tsikoza, Direct conversion of methane on Mo/ZSM-5 catalysts to produce benzene and hydrogen: achievements and perspectives, Energ. Environ. Sci. 1 (2008) 526–541. doi:10.1039/b810981h.

[53] D. Wang, J.H. Lunsford, M.P. Rosynek, Characterization of a Mo/ZSM-5 Catalyst for the Conversion of Methane to Benzene, J. Catal. 169 (1997) 347–358. doi:10.1006/jcat.1997.1712.

[54] B.M. Weckhuysen, D. Wang, M.P. Rosynek, J.H. Lunsford, Conversion of Methane to Benzene over Transition Metal Ion ZSM-5 Zeolites I. Catalytic Characterization, J. Catal. 175 (1998) 338–346. doi:10.1006/jcat.1998.2010.

[55] A.Y. Stakheev, A.Y. Khodakov, L.M. Kustov, V.B. Kazansky, K.M. Minachev, Localization of polyvalent cations in pentasil catalysts modified by metal oxides, Zeolites. 12 (1992) 866–869. doi:10.1016/0144-2449(92)90064-V.

[56] J.A. Biscardi, G.D. Meitzner, E. Iglesia, Structure and Density of Active Zn Species in Zn/H-ZSM5 Propane Aromatization Catalysts, J. Catal. 179 (1998) 192–202. doi:10.1006/jcat.1998.2177.

[57] W. Ding, S. Li, G. D Meitzner, E. Iglesia, Methane Conversion to Aromatics on Mo/H-ZSM5: Structure of Molybdenum Species in Working Catalysts, J. Phys. Chem. B. 105 (2001) 506–513. doi:10.1021/jp0030692.

[58] H.S. Lacheen, E. Iglesia, Isothermal activation of Mo2O52+-ZSM-5 precursors during methane reactions: effects of reaction products on

structural evolution and catalytic properties, Phys. Chem. Chem. Phys. 7 (2005) 538–547. doi:10.1039/b415166f.

[59] H.S. Lacheen, E. Iglesia, Stability, structure, and oxidation state of Mo/H-ZSM-5 catalysts during reactions of CH4 and CH4–CO2 mixtures, J. Catal. 230 (2005) 173–185. doi:10.1016/j.jcat.2004.11.037.

[60] Z. Liu, M.A. Nutt, E. Iglesia, The Effects of CO2, CO and H2 Co-Reactants on Methane Reactions Catalyzed by Mo/H-ZSM-5, Catal. Lett. 81 (2002) 271–279. doi:10.1023/A:1016553828814.

[61] A. Chakrabarti, M. Sharma, Cationic ion exchange resins as catalyst, React. Polym. 20 (1993) 1–45. doi:10.1016/0923-1137(93)90064-M.

[62] F.F. Bamoharram, M.M. Heravi, P. Ardalan, T. Ardalan, A kinetic study of the esterification of lactic acid by ethanol in the presence of Preyssler acid an eco-friendly solid acid catalyst, React. Kinet., Mech. Catal. 100 (2010) 71–78. doi:10.1007/s11144-010-0159-1.

[63] A. Corma, H. García, S. Iborra, J. Primo, Modified faujasite zeolites as catalysts in organic reactions: Esterification of carboxylic acids in the presence of HY zeolites, J. Catal. 120 (1989) 78–87. doi:10.1016/0021-9517(89)90252-2.

[64] X. Chen, Z.P. Xu, T. Okuhara, Liquid phase esterification of acrylic acid with 1-butanol catalyzed by solid acid catalysts, Appl. Catal. A. 180 (1999) 261–269. doi:10.1016/S0926-860X(98)00337-8.

[65] S. Miao, B.H. Shanks, Mechanism of acetic acid esterification over sulfonic acid-functionalized mesoporous silica, J. Catal. 279 (2011) 136–143. doi:10.1016/j.jcat.2011.01.008.

[66] A. Zecchina, S. Bordiga, G. Spoto, D. Scarano, G. Spano, F. Geobaldo, IR spectroscopy of neutral and ionic hydrogen-bonded complexes formed upon interaction of CH3OH, C2H5OH, (CH3)2O, (C2H5)2O and C4H8O with H-Y, H-ZSM-5 and H-mordenite: comparison with analogous adducts formed on the H-Nafion superacidic membrane, J. Chem. Soc. Faraday T. 92 (1996) 4863–4875. doi:10.1039/ft9969204863.

[67] C.-C. Lee, R.J. Gorte, W.E. Farneth, Calorimetric Study of Alcohol and Nitrile Adsorption Complexes in H-ZSM-5, J. Phys. Chem. B. 101 (1997) 3811–3817. doi:10.1021/jp970711s.

[68] H. Chiang, A. Bhan, Catalytic consequences of hydroxyl group location on the rate and mechanism of parallel dehydration reactions of ethanol over acidic zeolites, J. Catal. 271 (2010) 251–261. doi:10.1016/j.jcat.2010.01.021.

[69] W. Wang, J. Jiao, Y. Jiang, S.S. Ray, M. Hunger, Formation and decomposition of surface ethoxy species on acidic zeolite Y., ChemPhysChem. 6 (2005) 1467–9. doi:10.1002/cphc.200500262.

[70] S. Namuangruk, P. Pantu, J. Limtrakul, Alkylation of benzene with ethylene over faujasite zeolite investigated by the ONIOM method, J. Catal. 225 (2004) 523–530. doi:10.1016/j.jcat.2004.04.016.

[71] A. Ison, R.J. Gorte, The adsorption of methanol and water on H-ZSM-5*1, J. Catal. 89 (1984) 150–158. doi:10.1016/0021-9517(84)90289-6.

[72] S.R. Blaszkowski, R.A. van Santen, The Mechanism of Dimethyl Ether Formation from Methanol Catalyzed by Zeolitic Protons, J. Am. Chem. Soc. 118 (1996) 5152–5153. doi:10.1021/ja954323k.

[73] S. Svelle, C. Tuma, X. Rozanska, T. Kerber, J. Sauer, Quantum chemical modeling of zeolite-catalyzed methylation reactions: toward chemical accuracy for barriers., J. Am. Chem. Soc. 131 (2009) 816–825. doi:10.1021/ja807695p.

[74] E.M. Calverley, Letters to the Editor, AIChE J. 39 (1993) 725. doi:10.1002/aic.690390426.

[75] D.C. Harris, Nonlinear Least-Squares Curve Fitting with Microsoft Excel Solver, J. Chem. Educ. 75 (1998) 119–121. doi:10.1021/ed075p119.

[76] P. Cheung, A. Bhan, G.J. Sunley, E. Iglesia, Selective carbonylation of dimethyl ether to methyl acetate catalyzed by acidic zeolites., Ange, Chem. Int. Ed. 45 (2006) 1617–20. doi:10.1002/anie.200503898.

[77] H. Chiang, A. Bhan, Catalytic consequences of hydroxyl group location on the kinetics of n-hexane hydroisomerization over acidic zeolites, J. Catal. 283 (2011) 98–107. doi:10.1016/j.jcat.2011.07.006.

[78] V.S. Nayak, J.B. Moffat, Sorption and diffusion of alcohols in heteropoly oxometalates and ZSM-5 zeolite, J. Phys. Chem. 92 (1988) 7097–7102. doi:10.1021/j100336a014.

[79] D. Liu, A. Bhan, M. Tsapatsis, S. Al Hashimi, Catalytic Behavior of Brønsted Acid Sites in MWW and MFI Zeolites with Dual Meso- and Microporosity, ACS Catal. 1 (2011) 7–17. doi:10.1021/cs100042r.

[80] J.H. Lunsford, Catalytic conversion of methane to more useful chemicals and fuels: a challenge for the 21st century, Catal. Today. 63 (2000) 165–174. doi:10.1016/S0920-5861(00)00456-9.

[81] J.A. Labinger, J.E. Bercaw, Understanding and exploiting C-H bond activation., Nature. 417 (2002) 507–14. doi:10.1038/417507a.

[82] F. Solymosi, J. Cserenyi, A. Szöke, T. Bansagi, A. Oszko, Aromatization of methane over supported and unsupported Mo-based catalysts, J. Catal. 165 (1997) 150–161. doi:10.1006/jcat.1997.1478.

[83] F. Solymosi, A. Szöke, J. Cserenyi, Conversion of methane to benzene over Mo2C and Mo2C/ZSM-5 catalysts, Catal. Lett. 39 (1996) 157–161. doi:10.1007/BF00805576.

[84] F. Solymosi, A. Erdohelyi, A. Szöke, Dehydrogenation of methane on supported molybdenum oxides. Formation of benzene from methane, Catal. Lett. 32 (1995) 43–53. doi:10.1007/BF00806100.

[85] L. Li, R.W. Borry, E. Iglesia, Design and optimization of catalysts and membrane reactors for the non-oxidative conversion of methane, Chem. Eng. Sci. 57 (2002) 4595–4604. doi:10.1016/S0009-2509(02)00314-7.

[86] Y.-H. Kim, R.W. Borry, E. Iglesia, Catalytic Properties of Mo/HZSM-5 for CH4 Aromization, J. Ind. Eng. Chem. 6 (2000) 72–78.

[87] Y.-H. Kim, R.W. Borry, E. Iglesia, Genesis of methane activation sites in Mo-exchanged H–ZSM-5 catalysts, Micropor. Mesopor. Mat. 35-36 (2000) 495–509. doi:10.1016/S1387-1811(99)00245-0.

[88] R.W. Borry, Y.H. Kim, A. Huffsmith, J.A. Reimer, E. Iglesia, Structure and Density of Mo and Acid Sites in Mo-Exchanged H-ZSM5 Catalysts for Nonoxidative Methane Conversion, J. Phys. Chem. B. 103 (1999) 5787–5796. doi:10.1021/jp990866v.

[89] S. Liu, L. Wang, R. Ohnishi, M. Ichikawa, Bifunctional Catalysis of Mo/HZSM-5 in the Dehydroaromatization of Methane to Benzene and Naphthalene XAFS/TG/DTA/MASS/FTIR Characterization and Supporting Effects, J. Catal. 181 (1999) 175–188. doi:10.1006/jcat.1998.2310.

[90] J.C. Fierro-Gonzalez, S. Kuba, Y. Hao, B.C. Gates, Oxide- and zeolite-supported molecular metal complexes and clusters: physical characterization and determination of structure, bonding, and metal oxidation state., J. Phys. Chem. B. 110 (2006) 13326–51. doi:10.1021/jp0571123.

[91] B.C. Gates, Supported metal cluster catalysts, J. Mol. Catal. A-Chem.. 163 (2000) 55–65. doi:10.1016/S1381-1169(00)00399-X.

[92] W. Li, G.D. Meitzner, R.W. Borry, E. Iglesia, Raman and X-Ray Absorption Studies of Mo Species in Mo/H-ZSM5 Catalysts for Non-Oxidative CH4 Reactions, J. Catal. 191 (2000) 373–383. doi:10.1006/jcat.1999.2795.

[93] D. Ma, Y. Shu, M. Cheng, Y. Xu, X. Bao, On the Induction Period of Methane Aromatization over Mo-Based Catalysts, J. Catal. 194 (2000) 105–114. doi:10.1006/jcat.2000.2908.

[94] B.M. Weckhuysen, D. Wang, M.P. Rosynek, J.H. Lunsford, Conversion of Methane to Benzene over Transition Metal Ion ZSM-5 Zeolites II. Catalyst Characterization by X-Ray Photoelectron Spectroscopy, J. Catal. 175 (1998) 347–351. doi:10.1006/jcat.1998.2011.

[95] H. Zheng, D. Ma, X. Bao, J.Z. Hu, J.H. Kwak, Y. Wang, et al., Direct observation of the active center for methane dehydroaromatization using an ultrahigh field 95Mo NMR spectroscopy., J. Am. Chem. Soc. 130 (2008) 3722–3. doi:10.1021/ja7110916.

[96] D. Ma, Y. Shu, W. Zhang, X. Han,, Y. Xu, X. Bao, In Situ 1H MAS NMR Spectroscopic Observation of Proton Species on a Mo-Modified HZSM-5 Zeolite Catalyst for the Dehydroaromatization of Methane, Ange. Chem. Int. Ed. 39 (2000) 2928–2931. doi:10.1002/1521-3773(20000818)39:16<2928::AID-ANIE2928>3.3.CO;2-K.

[97] Y. Shu, H. Ma, R. Ohnishi, M. Ichikawa, Highly stable performance of catalytic methane dehydrocondensation towards benzene on Mo/HZSM-5 by a periodic switching treatment with H2 and CO2, Chem. Commun. (2003) 86–87. doi:10.1039/b208607g.

[98] R. Ohnishi, S. Liu, Q. Dong, L. Wang, M. Ichikawa, Catalytic Dehydrocondensation of Methane with CO and CO2toward Benzene and Naphthalene on Mo/HZSM-5 and Fe/Co-Modified Mo/HZSM-5, J. Catal. 182 (1999) 92–103. doi:10.1006/jcat.1998.2319.

[99] Y. Shu, R. Ohnishi, M. Ichikawa, Pressurized Dehydrocondensation of Methane toward Benzene and Naphthalene on Mo/HZSM-5 Catalyst: Optimization of Reaction Parameters and Promotion by CO2 Addition, J. Catal. 206 (2002) 134–142. doi:10.1006/jcat.2001.3481.

[100] S.Y. Yu, J.A. Biscardi, E. Iglesia, Kinetic Relevance of Hydrogen Desorption Steps and Virtual Pressures on Catalytic Surfaces during Reactions of Light Alkanes, J. Phys. Chem. B. 106 (2002) 9642–9648. doi:10.1021/jp020780t.

[101] S.Y. Yu, T. Waku, E. Iglesia, Catalytic desulfurization of thiophene on H-ZSM5 using alkanes as co-reactants, Appl. Catal. A. 242 (2003) 111–121. doi:10.1016/S0926-860X(02)00507-0.

[102] S.Y. Yu, J. Garcia-Martinez, W. Li, G.D. Meitzner, E. Iglesia, Kinetic, infrared, and X-ray absorption studies of adsorption, desorption, and

reactions of thiophene on H-ZSM5 and Co/H-ZSM5, Phys. Chem. Chem. Phys. 4 (2002) 1241–1251. doi:10.1039/b108640p.

[103] W. Li, S.Y. Yu, E. Iglesia, Isotopic Tracer Studies of Thiophene Desulfurization Reactions Using Hydrogen from Alkanes on H-ZSM5 and Co/H-ZSM5, J. Catal. 203 (2001) 175–183. doi:10.1006/jcat.2001.3309.

[104] S.Y. Yu, W. Li, E. Iglesia, Desulfurization of Thiophene via Hydrogen Transfer from Alkanes on Cation-Modified H-ZSM5, J. Catal. 187 (1999) 257–261. doi:10.1006/jcat.1999.2668.

[105] J.S. Lee, S.T. Oyama, M. Boudart, Molybdenum carbide catalysts I. Synthesis of unsupported powders, J. Catal. 106 (1987) 125–133. doi:10.1016/0021-9517(87)90218-1.

[106] K. Stadnicka, J. Haber, R. Kozłowski, The crystal structure of magnesium dimolybdate, Acta Cryst. B. 33 (1977) 3859–3862. doi:10.1107/S0567740877012229.

[107] B. Ravel, M. Newville, ATHENA, ARTEMIS, HEPHAESTUS: data analysis for X-ray absorption spectroscopy using IFEFFIT., J. Synchrotron Radiat. 12 (2005) 537–41. doi:10.1107/S0909049505012719.

[108] D. Ma, Y. Shu, X. Bao, Y. Xu, Methane Dehydro-aromatization under Nonoxidative Conditions over Mo/HZSM-5 Catalysts: EPR Study of the Mo Species on/in the HZSM-5 Zeolite, J. Catal. 189 (2000) 314–325. doi:10.1006/jcat.1999.2704.

[109] D. Zhou, D. Ma, X. Liu, X. Bao, Study with density functional theory method on methane dehydro-aromatization over Mo/HZSM-5 catalysts I: Optimization of active Mo species bonded to ZSM-5 zeolite, J. Chem. Phys. 114 (2001) 9125. doi:10.1063/1.1366316.

[110] J.-P. Tessonnier, B. Louis, S. Walspurger, J. Sommer, M.-J. Ledoux, C. Pham-Huu, Quantitative measurement of the Brönsted acid sites in solid acids: toward a single-site design of Mo-modified ZSM-5 zeolite., J. Phys. Chem. B. 110 (2006) 10390–5. doi:10.1021/jp0602629.

[111] J.-P. Tessonnier, B. Louis, S. Rigolet, M.-J. Ledoux, C. Pham-Huu, Methane dehydro-aromatization on Mo/ZSM-5: About the hidden role of Brønsted acid sites, Appl. Catal. A. 336 (2008) 79–88. doi:10.1016/j.apcata.2007.08.026.

[112] T. Ressler, O. Timpe, T. Nesius, J. Find, G. Mestl, M. Dieterle, et al., Time-Resolved XAS Investigation of the Reduction/Oxidation of MoO3−x, J. Catal. 191 (2000) 75–85. doi:10.1006/jcat.1999.2772.

[113] S.P. Cramer, K.O. Hodgson, W.O. Gillum, L.E. Mortenson, The molybdenum site of nitrogenase. Preliminary structural evidence from x-ray absorption spectroscopy, J. Am. Chem. Soc. 100 (1978) 3398–3407. doi:10.1021/ja00479a023.

[114] F. Solymosi, A. Szöke, Conversion of ethane into benzene on Mo2C/ZSM-5 catalyst, Appl. Catal. A. 166 (1998) 225–235. doi:10.1016/S0926-860X(97)00260-3.

[115] S. Burns, J.S.J. Hargreaves, P. Pal, K.M. Parida, S. Parija, The effect of dopants on the activity of MoO3/ZSM-5 catalysts for the dehydroaromatisation of methane, Catal. Today. 114 (2006) 383–387. doi:10.1016/j.cattod.2006.02.030.

[116] B.M. Weckhuysen, M.P. Rosynek, J.H. Lunsford, Characterization of surface carbon formed during the conversion of methane to benzene over Mo / H-ZSM-5 catalysts, Catal. Lett. 52 (1998) 31–36. doi:10.1023/A:1019094630691.

[117] Y. Xu, J. Lu, J. Wang, Y. Suzuki, Z.-G. Zhang, The catalytic stability of Mo/HZSM-5 in methane dehydroaromatization at severe and periodic CH4–H2 switch operating conditions, Chem. Eng. J. 168 (2011) 390–402. doi:10.1016/j.cej.2011.01.047.

[118] J.R. Taylor, An Introduction to Error Analysis: The Study of Uncertainties in Physical Measurements, 2nd ed., University Science Books, Sausalito, CA, 1997.

[119] S. Yuan, J. Li, Z. Hao, Z. Feng, Q. Xin, P. Ying, et al., The effect of oxygen on the aromatization of methane over the Mo/HZSM-5 catalyst, Catal. Lett. 63 (1999). doi:10.1023/A:1019096300302.

[120] H. Hwu, M. Zellner, J. Chen, The chemical and electronic properties of oxygen-modified C/Mo(110): a model system for molybdenum oxycarbides, J. Catal. 229 (2005) 30–44. doi:10.1016/j.jcat.2004.09.014.

[121] J.W. Bedard, D.-Y. Hong, A. Bhan, CH4 dehydroaromatization on Mo/H–ZSM-5: 1. Effects of co-processing H2 and CH3COOH, J. Catal. 306 (2013) 58–67. doi:10.1016/j.jcat.2013.06.003.

[122] S. Yao, C. Sun, J. Li, X. Huang, W. Shen, A 13CO isotopic study on the CO promotion effect in methane dehydroaromatization reaction over a Mo/HMCM-49 catalyst, J. Nat. Gas Chem. 19 (2010) 1–5. doi:10.1016/S1003-9953(09)60031-1.

[123] J.J. Spivey, G. Hutchings, Catalytic aromatization of methane., Chem. Soc. Rev. 43 (2014) 792–803. doi:10.1039/c3cs60259a.

[124] J. Gao, Y. Zheng, G.B. Fitzgerald, J. de Joannis, Y. Tang, I.E. Wachs, et al., Structure of Mo 2 C x and Mo 4 C x Molybdenum Carbide Nanoparticles and Their Anchoring Sites on ZSM-5 Zeolites, J. Phys. Chem. C. 118 (2014) 4670–4679. doi:10.1021/jp4106053.

[125] J.W. Bedard, D.-Y. Hong, A. Bhan, Co-processing CH4 and oxygenates on Mo/H-ZSM-5: 2. CH4-CO2 and CH4-HCOOH mixtures., Phys. Chem. Chem. Phys. 15 (2013) 12173–9. doi:10.1039/c3cp50855b.

[126] G.L. Price, E. Iglesia, Matrix method for correction of mass spectra in deuterium-exchange applications, Ind. Eng. Chem. Res. 28 (1989) 839–844. doi:10.1021/ie00090a028.

[127] J. Chheda, J.A. Dumesic, An overview of dehydration, aldol-condensation and hydrogenation processes for production of liquid alkanes from biomass-derived carbohydrates, Catal. Today. 123 (2007) 59–70. doi:10.1016/j.cattod.2006.12.006.

[128] T.Q. Hoang, X. Zhu, T. Sooknoi, D.E. Resasco, R.G. Mallinson, A comparison of the reactivities of propanal and propylene on HZSM-5, J. Catal. 271 (2010) 201–208. doi:10.1016/j.jcat.2010.01.017.

[129] P. Dejaifve, J.C. Vedrine, V. Bolis, E.G. Derouane, Reaction pathways for the conversion of methanol and olefins on H-ZSM-5 zeolite, J. Catal. 63 (1980) 331–345. doi:10.1016/0021-9517(80)90086-X.